Astronomy Letters, Vol. 26, No. 5, 2000, pp. 269–276. Translated from Pis'ma v Astronomicheskiĭ Zhurnal, Vol. 26, No. 5, 2000, pp. 323–332.

Early Afterglows of Short Gamma-Ray Bursts

R. A. Burenin*

Space Research Institute, Russian Academy of Sciences, ul. Profsoyuznaya 84/32, Moscow, 117810 Russia

Received October 1, 1999

Abstract—In the relativistic fireball model, the afterglow of a gamma-ray burst (GRB) is produced by synchrotron radiation of the electrons accelerated in the external shock that emerges as the relativistic flow moves. According to this model, the afterglow peaks on a time scale of ~10 s when observed in the soft gamma-ray band. The peak flux can be high enough to be detected by modern all-sky monitors. We investigate the emission from short ($\Delta T < 1$ s) GRBs on a time scale $t \approx 10$ s using BATSE/CGRO data. A significant flux is recorded for ~20% of the events. In most cases, the observed persistent emission can be explained in terms of the model as an early burst afterglow. No early afterglows of most short GRBs are observed. The model parameters for these bursts are constrained. © *2000 MAIK "Nauka/Interperiodica"*.

Key words: *gamma-ray bursts*

1. INTRODUCTION

The enormous energy release in cosmological GRB sources (10^{52}–3×10^{54} erg; see, e.g., [1]), the nonthermal spectra with a large number of hard photons $h\nu > 511$ keV, which could produce electron–positron pairs at a high energy density, and the gamma-ray flux variability on short time scales ($c\delta t \lesssim 300$ km) prompt us to consider models in which the radiation source moves toward the observer at a relativistic velocity [2, 3]. To solve the "problem of compactness" of the GRB source requires a Lorentz factor $\gamma \gtrsim 100$. In order to relax the requirements on the source's energetics, models in which the kinetic energy of its motion is converted into gamma-ray emission are considered. The relativistic fireball model is currently most popular. In this model, the kinetic energy of the relativistic flow transforms to the energy of gamma-ray photons through synchrotron radiation of the electrons accelerated in the shocks produced by the interaction between different parts of the flow and by its interaction with the interstellar medium (in the so-called internal and external shocks; see, e.g., the review by Piran [4]).

The rapid variability of GRBs cannot be explained by external shocks ([5, 6]; see, however, [7]). On the other hand, internal shocks do not ensure the conversion of a significant fraction of the energy of the relativistic flow into radiation, and most of its kinetic energy must dissipate in external shocks. The latter are assumed to be responsible for the burst afterglows. According to these ideas, the observed afterglow parameters must depend mainly on the initial relativistic-flow velocity and on the properties of the medium surrounding the source. The parameters of the main burst depend markedly on the properties of the source itself; therefore, the relative characteristics of GRBs and their afterglows are not necessarily similar, by any means, for different bursts, which is the case (see, e.g., [8]).

The spectra and light curves of GRB afterglows that are possible in this model were described in [9, 10]. The observed light curves of X-ray and optical burst afterglows turned out to follow power laws with indices that were in satisfactory agreement with theoretical predictions for the final evolutionary stages of the light curve. This was perceived as a confirmation of the model (see, e.g., [11]). All-wave observations of the afterglow spectrum for GRB 970508 also showed good agreement with theory [12].

One usually manages to observe the afterglow several hours after a GRB, when one has time to point optical, X-ray, and radio telescopes at its source. At this time, the Lorentz factor of the flow motion drops to $\gamma \lesssim 10$, irrespective of its initial value. It is therefore of interest to observe burst afterglows at the earliest stage of GRB development, when the Lorentz factor of the flow motion, as well as the density and temperature of the matter, are at a maximum. Such observations could allow the initial Lorentz factor γ_0 and other model parameters to be determined. Note the recently published observations of early GRB afterglows in the soft gamma-ray [13–15] and optical [16] bands.

* E-mail address for contacts: br@hea.iki.rssi.ru

1063-7737/00/2605-0269$20.00

2. AFTERGLOW INTENSITY

In the relativistic fireball model, the GRB afterglows are explained by synchrotron radiation of the electrons accelerated in the external shock produced by the interaction of the relativistic flow with the interstellar medium [9, 10]. The afterglow spectra consist of power-law segments with breaks at several characteristic frequencies: ν_m is the frequency corresponding to the maximum of the electron energy distribution, and ν_c is the frequency above which the electrons are cooled significantly by synchrotron radiation. The frequency below which the emission is self-absorbed significantly always lies in the radio band. The soft gamma-ray flux from the afterglow initially increases as $F_\nu \propto t^2$. At time $t = t_\gamma$, the relativistic shell gathers a fairly large amount of interstellar matter on its way and begins to decelerate. Subsequently, the afterglow flux drops; the light curve consists of power-law segments with breaks at times t_m and t_c when the time-varying frequencies ν_m and ν_c pass through the range of observation.

The model has the following parameters: initial Lorentz factor γ_0 of the shell motion, redshift z of the source, initial kinetic energy E of the shell, fractions ϵ_e and ϵ_B of the electrons and the magnetic field in the post-shock energy density, and particle density n of the ambient interstellar medium. The afterglow flux can be calculated for any set of these parameters by using formulas from [10]. Figure 1 shows how the 30–300-keV flux from an early afterglow depends on each of these parameters separately for different t. We designated $E_{52} = 2(1 - \cos\theta)^{-1}E/(10^{52}$ erg), where θ is the apex angle of the cone in which the shell moves. In each panel, only the indicated parameter varies, while the remaining parameters are fixed: $\gamma_0 = 300$, $z = 0.65$, $E_{52} = 1$, $\epsilon_e = 0.1$, $\epsilon_B = 0.1$, and $n = 1$ cm^{-3}. Approximately the same parameters were obtained from observations of the afterglow of GRB 970508 [17]. Since the density n can apparently vary over a wide range, we took an approximate mean interstellar-gas density as a typical parameter. The power-law slope of the energy distribution of the accelerated electrons was assumed to be $p = 2.5$. The correspondence between different lines and different times is indicated in the lower right panel (z). The curves in Fig. 1 change their slope at some parameters, because the afterglow flux depends differently on them for different relationships of the characteristic times t_γ, t_m, and t_c to the time of observation t, while the times t_γ, t_m, and t_c, in turn, also depend on the model parameters. For the same reason, the curves corresponding to fixed times touch the dependence for the flux at $t = t_\gamma$.

As we see from Fig. 1, for a considerable fraction of the range of possible parameters, the 30–300-keV flux from an early afterglow proves to be high enough to be detected by modern all-sky monitors. Apart from the flux, the quantities t_γ and ν_m, which also depend on the model parameters, can be determined from the observed gamma-ray light curve and spectrum. Since the number of parameters is larger than the number of measurable quantities, the parameters cannot be determined completely. They can only be constrained from observations.

3. SHORT BURSTS

The time when the afterglow peaks in the soft gamma-ray band, $t_\gamma \approx 5$ s [10], is equal to the duration of some bursts in order of magnitude. If the emission from external shocks is superimposed on the emission from the main burst, which is produced in internal shocks, then they are difficult to separate when observed in the soft gamma-ray band. However, for sufficiently short GRBs, the afterglow peak and the main burst can be separated in time. As was said above, the afterglow flux can be high enough to be detected by modern instruments.

It should be noted that X-ray, optical, and radio afterglows have been detected only for bursts with durations of a few seconds or more. This is attributable to peculiarities of the BeppoSAX wide-field cameras whose data are used to point telescopes with a narrow field of view [18]. As yet no afterglows of short bursts have been observed on long time scales, and, accordingly, there is no direct confirmation that at least some of the sources of short GRBs lie at cosmological distances. Short ($\lesssim$1 s) bursts are generally believed to constitute a separate class of events, as suggested by the bimodal duration distribution of GRBs. In addition, short GRBs differ from longer ones in that they are, on the average, harder [19] and their flux distribution is in better agreement with the assumption of a uniform distribution of the sources in Euclidean space [20]. The latter implies that their sources must be closer than the sources of long bursts. If the sources of these bursts were in the Galactic disk, then no fireball would be formed in them. A relativistic fireball must emerge in a GRB source if it lies at a distance $\gtrsim$30 kpc [21]. Here, we compare the persistent emission from short bursts with model predictions by assuming that the sources of these bursts lie at cosmological distances. Even if no soft gamma-ray emission is observed on a time scale of ~10 s after short bursts, we can constrain the model parameters. If, however, a long "tail" is detected after a short GRB, then we can try to estimate the extent to which the observed characteristics of this emission match the characteristics of the emission from external shocks.

4. SEARCH FOR AFTERGLOWS

The BATSE instrument onboard the Compton Gamma-Ray Observatory (CGRO) is most sensitive to GRBs in the 30–300-keV band. A detailed description of the instrument can be found, for example, in [22]. Time histories of the bursts detected by this instrument are accessible via Internet.[1] Parameters of a polynomial

[1] http://cossc.gsfc.nasa.gov/cossc/BATSE.html

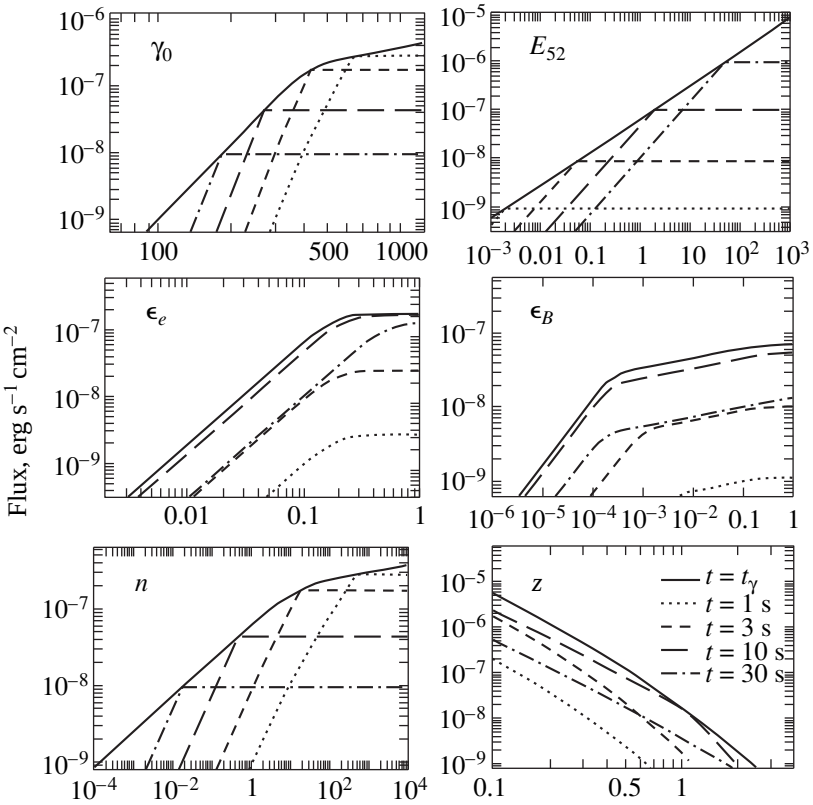

Fig. 1. Afterglow flux versus model parameters: γ_0, E_{52}, ϵ_e, ϵ_B, n, and z. In each panel, only one parameter varies, while the remaining parameters have fixed values (see the text). The correspondence between different lines and different times is indicated in the lower left panel (z).

fit to the background for each burst can also be found there. The Compton Observatory is in a low orbit, and the onboard instruments are affected by high-energy particles in the radiation belts, magnetospheric anomalies, etc. The BATSE background count rate can therefore exhibit a significant instability. However, the background on a time scale of ~10 s can be modeled reliably enough. The BATSE background is much more difficult to model on time scales $\gtrsim$100 s. For example, when the early afterglow of GRB 980923 was observed, the background had to be modeled by assuming that it depended only on the satellite's orbital phase and did not change from turn to turn [15]. The afterglow had been observed for ~400 s. BATSE observations of GRB afterglows on such long time scales are also complicated by the fact that the burst source is eclipsed by the Earth every several thousand seconds.

As was said above, even if the main burst is short, an afterglow in which an energy comparable to the energy of the main event is released can be detected following it. As a characteristic of the duration of the main event, we use its duration at 1/3 of the maximum of the light curve, $T_{1/3}$. Figure 2 shows how $T_{1/3}$ and T_{90}, the time in which 90% of the GRB energy is released (this characteristic of duration is given in the BATSE gamma-ray burst catalog [23]), are related. We used light curves for about 300 most intense bursts detected by BATSE. The inclined lines in Fig. 2 represent linear dependences with slopes of 1, 10^{-1}, and 10^{-2}. If the measure of duration $T_{1/3}$ is used to select short bursts instead of T_{90}, then events for which, following the main peak of the time history, emission is detected on long time scales with a flux much lower than that at maximum of the light curve remain in the sample. In the model under consideration, it is this emission that could be produced in an external shock. In addition, $T_{1/3}$ must be much less distorted during measurements with different sensitivities, because it is not associated with measurements of low fluxes in the tails of the GRB time histories.

Let us consider the 98 most intense BATSE bursts with $T_{1/3} < 1$ s, whose time histories are accessible via Internet. Forty three of them have $T_{1/3} < 0.3$ s. In Fig. 3, fluxes in the intervals 1–3, 3–10, and 10–30 s after the peaks of the burst time histories are plotted against peak fluxes. The dots were plotted in the figure only if a significant (at 95% confidence) flux was detected for a given burst in a given time interval. The horizontal solid lines mark 68% upper limits on the flux in these time intervals for the remaining GRBs. In the first time interval, we considered only 43 bursts with $T_{1/3} < 0.3$ s. The dotted lines indicate linear dependences with slopes of 10^{-2} and 10^{-3}. We calibrated the fluxes by

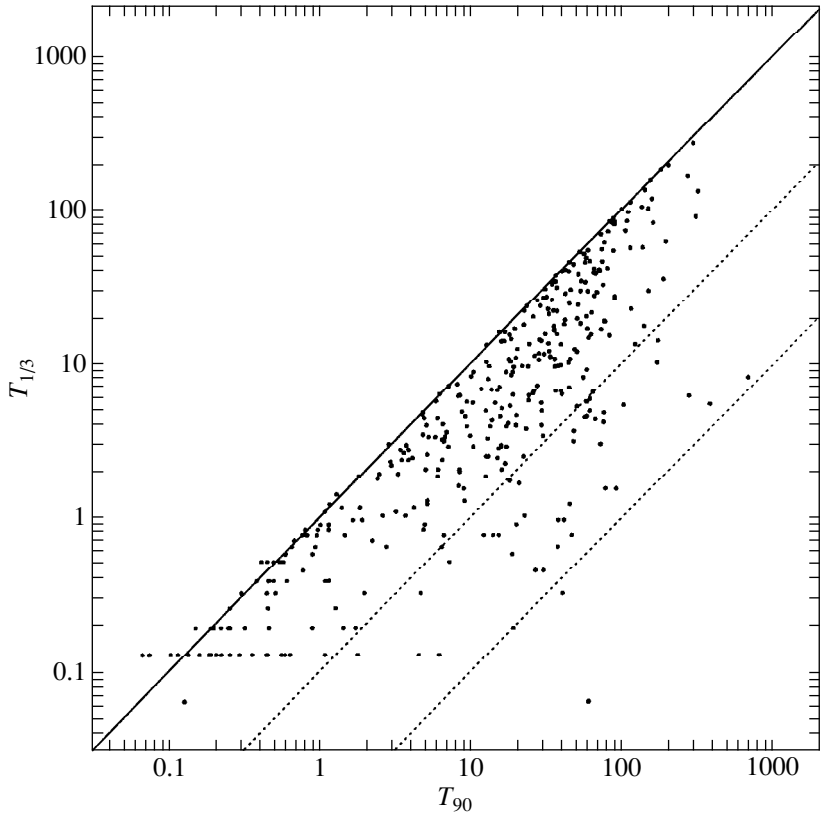

Fig. 2. Comparison of T_{90} and $T_{1/3}$, which characterize burst duration.

using the 4th BATSE gamma-ray burst catalog [23] and the "current" GRB catalog accessible via Internet.[2] The calibration uncertainty does not exceed 50%. Since the error associated with the conversion of detector count rates to energy units does not affect the significance of flux detection, it was not included in the errors shown in Fig. 3. As is evident from Fig. 3, here we consider bursts with peak fluxes $\gtrsim 10^{-6}$ erg s^{-1} cm^{-2}, i.e., approximately 20% of the most intense short GRBs detected by BATSE.

In each of the time intervals, a significant (at 95% confidence) flux is detected approximately for 20% of the bursts: for 11, 28, and 21 events, respectively. The flux on time scales much longer than the burst duration correlates weakly with the flux during the main event. This is consistent with the assumption that the emission is produced in processes that are not directly related to one another (for example, in internal and external shocks). As an example, Fig. 4 shows light curves for the weak tails of the time histories. Only the bases of the main GRB peaks are seen in the figure. Maximum count rates are indicated alongside them.

Although the observed emission in many cases is very weak, it can be noticed that more than a third (~5–10 of ~20) of the tails of the time histories for short bursts represent a gentle rise of the light curve with a characteristic size of ~30 s on which variability with $\delta t \lesssim 1$ s is superimposed. As an example, Fig. 4a shows GRB 921022 (triggering 1997), the most intense burst of this type. The GRB tail-to-peak flux ratio reaches 10^{-1}. The tails of the time histories for the remaining bursts represent a smooth fall, which starts immediately after the completion of the main event. This emission is much weaker with respect to the peak flux than that in the former case and accounts for a fraction of $\sim 10^{-3}$. As an example, Fig. 4b shows GRB 930131 (triggering 2151), the most intense burst of this type (and by far the most intense short GRB detected by BATSE). The bursts of these two types are in a majority. Similar types of weak burst tails have been previously identified by using PHEBUS/Granat data [24]. However, some bursts cannot be classified in this way. As an example, Fig. 4c shows the intense GRB 970201 (triggering 5989); the tail of its time history exhibits individual smooth emission peaks.

Let us define the effective spectral index α as the index of a power-law spectrum $F_\nu \propto \nu^{-\alpha}$ with the ratio of 100–300-keV and 30–100-keV fluxes equal to the observed one. In Fig. 5, effective spectral indices in different time intervals during and after bursts are plotted against spectral indices at the peaks of the time histories. Figure 5a shows the GRB effective spectral indices averaged over the entire time history. They correlate

[2] http://www.batse.msfc.nasa.gov/data/grb/catalog/

well with the spectral indices at maximum of the light curve. Here, we used all 98 bursts with $T_{1/3} < 1$ s. This figure gives an idea of the distribution of spectral indices for short GRBs. In most cases, the emission from a burst is, on the average, softer than the emission at its peak, a clear consequence of the flux–hardness correlation [25]. The other three figures (5b–5d) show effective spectral indices in the time intervals 1–3, 3–10, and 10–30 s after the GRB peaks. The horizontal dashed line marks $\alpha = 1/2$, which one might expect for the afterglow spectrum if the frequency of the synchrotron peak is higher than the frequency at which the observations are carried out, $\nu < \nu_m$. As is evident from these figures, the spectra of most tails of the time histories are fairly hard, and their slopes most likely correspond precisely to this situation (we would have had $\alpha = p/2 \approx 1.3$ at $\nu_m < \nu$). We see from Figs. 5b–5d and from a comparison of these figures with Fig. 5a that the observed persistent GRB emission is considerably softer than the emission during the main event. Figure 6 shows how the effective spectral indices are related in the intervals 3–10 and 10–30 s. This figure leads us to conclude that the spectral slope of the persistent emission for most bursts does not vary with time, within the limits of the measurement errors.

In those cases where no significant flux was detected, its 68% upper limit is $\sim 3 \times 10^{-9}$ erg s^{-1} cm^{-2} (Fig. 3); i.e., BATSE is sensitive enough to detect early afterglows of short GRBs at typical model parameters (see Sect. 2). Recall that the 30–300-keV flux at the afterglow peak can be 10^{-8}–10^{-6} erg s^{-1} cm^{-2} (Fig. 1).

For 80% of the bursts for which no significant flux was detected in the intervals 1–3, 3–10, and 10–30 s, the burst-averaged fluxes in these time intervals are $(2.65 \pm 0.91) \times 10^{-9}$, $(1.09 \pm 0.44) \times 10^{-9}$, and $(0.30 \pm 0.25) \times 10^{-9}$ erg s^{-1} cm^{-2}, respectively.

5. RESULTS

The emission from an external shock must possess certain peculiarities. As was pointed out above, it cannot exhibit rapid variability and have a gentle light curve of certain shape and a certain spectrum. There are few short intense GRBs with a significant flux at $t \gg T_{1/3}$ (about 20%). At certain model parameters, the flux from an early afterglow may well be equal to the observed one. Let us estimate the extent to which other characteristics of this emission are consistent with the assumption that it is produced in an external shock.

In the previous section, we discussed light curves of different types. For light curves of the type that GRB 921022 (triggering 1997, Fig. 4a) has, we can estimate $t_\gamma \approx 30 \text{ s} \approx 5 \text{ s } (1+z) E_{52}^{1/3} (\gamma_0/300)^{-8/3} (n/\text{cm}^{-3})^{-1/3}$ [10]. However, the presence of rapid variability is inconsistent with the assumption that the emission is produced in an external shock. It is possible that this variability can be explained by inhomogeneity of the medium surrounding the source [7] without going far beyond the model. If the light curve of the persistent emission represents a smooth fall which starts immediately after the completion of the main event, as, for example, in GRB 930131 (Fig. 4b), then we can estimate $t_\gamma \lesssim 1$ s. Since the estimates of t_γ for these two types of light curve differ significantly, the sets of parameters for them must also differ markedly. Constraints on the model parameters for each burst can be obtained from observed fluxes. It seems unlikely that the persistent emission from GRB 970201 (Fig. 4c) is its early afterglow, because the peaks in the tail of the time history differ from the main one only in amplitude. No bursts with a single smooth broad peak in the tail of the time history are observed: it is this shape of the light curve that is expected for the early afterglows of GRBs near maximum.

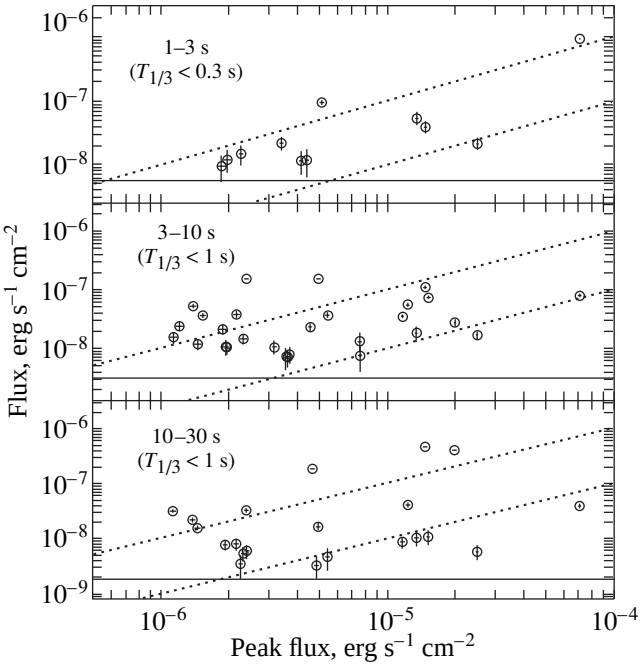

Fig. 3. Fluxes in the intervals 1–3, 3–10, and 10–30 s after the peaks of the burst time histories versus peak fluxes. The dotted lines represent linear dependences with slopes of 10^{-2} and 10^{-3}.

The spectral index of an early afterglow in the soft gamma-ray band can be either 1/2 or $p/2 \approx 1.2$–1.5, which corresponds to the cases where $\nu < \nu_m$ and vice versa [10]. As was said in the previous section, the recorded persistent emission is fairly hard, and the observed spectral indices agree with $\alpha \approx 1/2$ in most cases (Fig. 5). In the model, this corresponds to a situation when $\nu < \nu_m$. A constraint on the model parameters also follows from this inequality. It can be inferred from Fig. 5d that the condition $\nu < \nu_m$ is also satisfied in the time interval 10–30 s. Under the assumption of adiabatic evolution, this would imply that the time when the frequency of the synchrotron peak crosses the band of observation is $t_m \gtrsim 10$ s; hence,

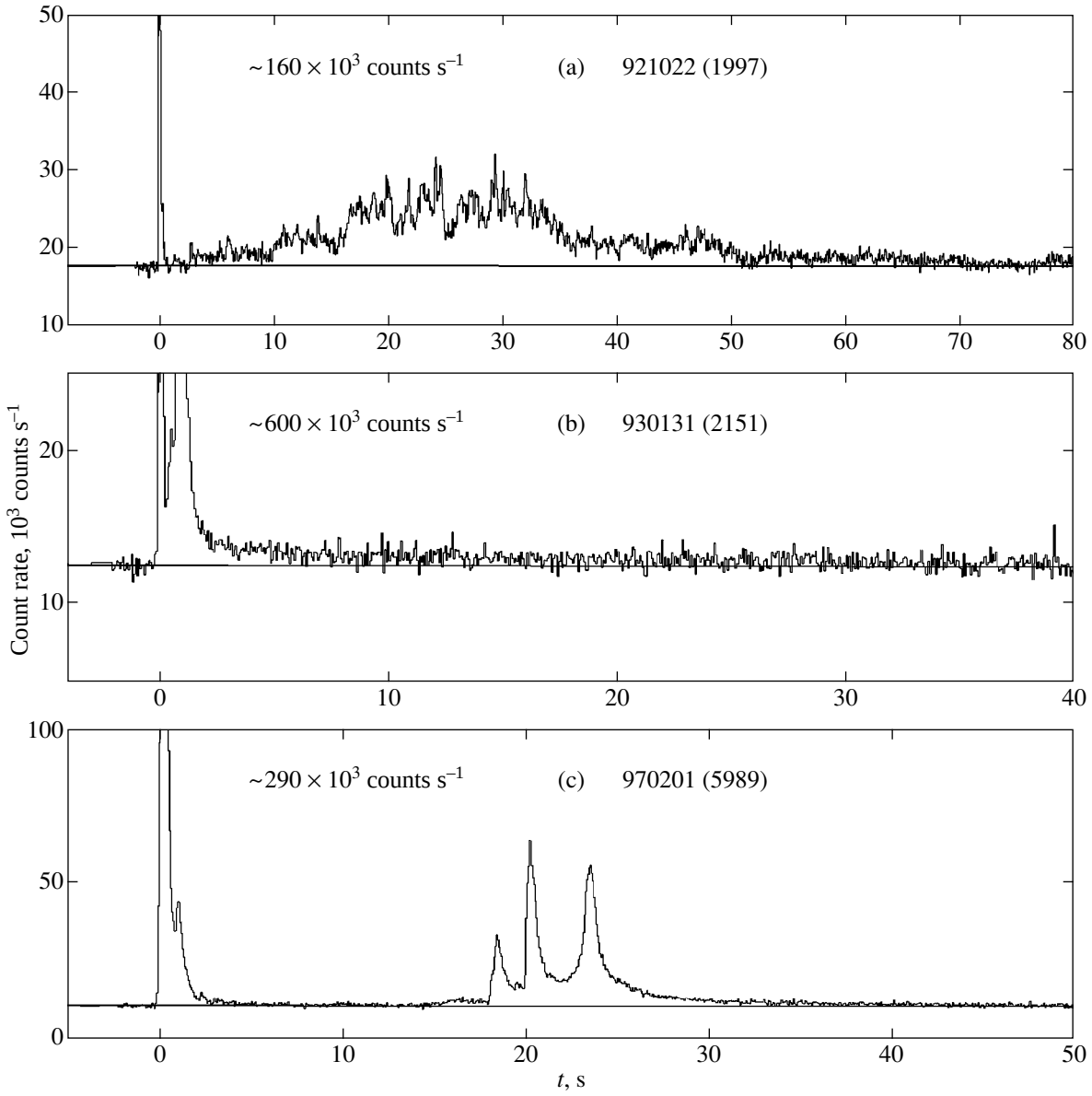

Fig. 4. Light curves for the weak tails of the time histories of short GRBs.

$(\epsilon_e/0.1)^{4/3}(\epsilon_B/0.1)^{1/3}E_{52}^{1/3} \gtrsim 10$. A similar constraint on t_m followed from an attempt to apply the model under consideration to a soft gamma-ray observation of the afterglow of GRB 920723 [13]. These constraints can be matched with the constraints on the model parameters obtained for bursts without observable persistent emission on long time scales (see below) only by increasing the distance to the GRB sources.

No early afterglows of most (~80%) short GRBs are detected, which allows the model parameters for the sources of these bursts to be constrained. The set of parameters must satisfy an upper limit on the early-afterglow flux. The table gives constraints on each of these parameters, provided that all the remaining parameters have typical values (Sect. 2). Moderate values of $\gamma_0 \lesssim 300$ seem preferable, because, at $\gamma_0 \sim 1000$, the other parameters must be changed considerably to satisfy the limit on the flux. This is reflected in the second and fourth rows of the table, where γ_0 was set equal to 1000, while the remaining parameters change as in the other rows. Clearly, if we change several parameters simultaneously, then the constraints on each of them can be less severe. However, observations rule out the possibility that the GRB sources are nearby and, concurrently, all the remaining parameters are large.

At moderate initial Lorentz factors $\gamma_0 \lesssim 300$, the afterglow peaks later (at $\gamma_0 \sim 100$, $t_\gamma \approx 100$–200 s). However, as was noted above, weak GRB emission on such time scales is difficult to study with BATSE because of unstable background. To investigate early afterglows at

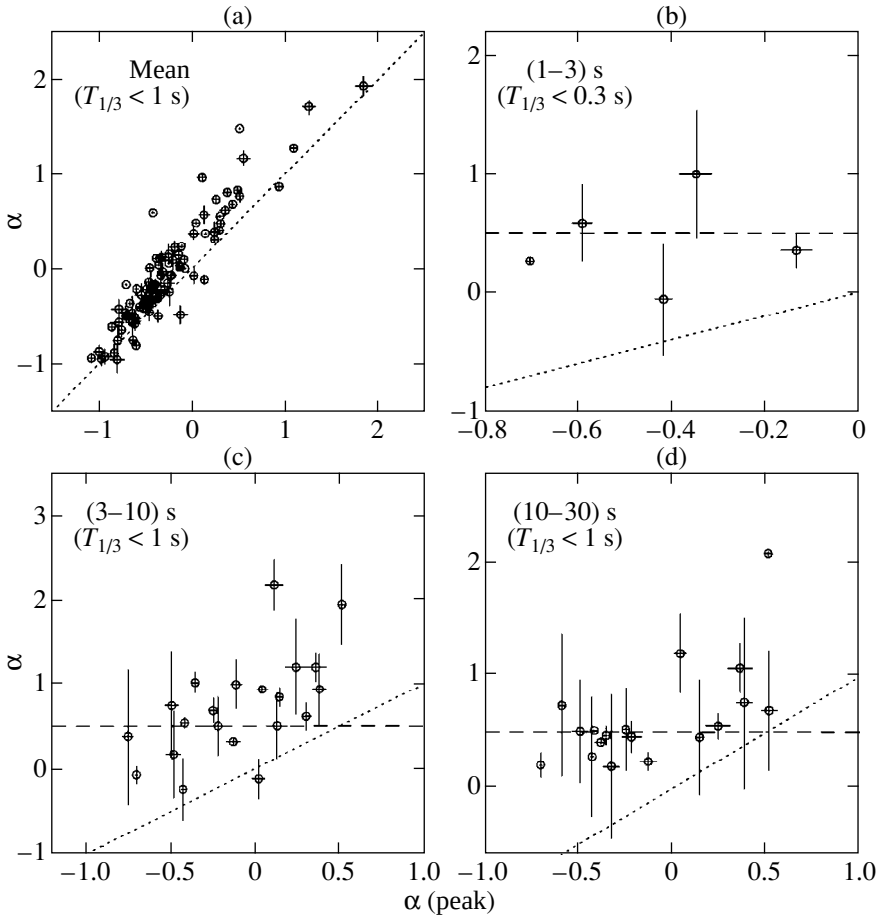

Fig. 5. Effective spectral indices in different time intervals versus spectral indices at burst peaks: (a) averaged over the entire time history; (b) in the interval 1–3 s; (c) 3–10 s; and (d) 10–30 s.

$t \sim 10^2$–10^3 s requires a stable background, which, for example, the Granat instruments have (see, e.g., [13]).

All the model parameters except the initial Lorentz factor γ_0 can be determined from afterglow observations at later stages. This has been done for several bursts. The parameters deduced from observations of the afterglows of GRBs 970508 and 911214 do not differ greatly from the typical values chosen here [17, 26]. The density of the interstellar medium was found to be $n \approx 0.03$ cm^{-3}. Based on observations of the optical flare that accompanied GRB 990123 [16] and assuming that the model parameters were the same as those for the afterglow of GRB 970508, Sari and Piran [10] estimated the initial Lorentz factor to be $\gamma_0 \sim 200$. In this case, $t_\gamma \approx 30$ s, and the peak flux is $\sim 10^{-8}$ erg s^{-1} cm^{-2}, in agreement with our results for short bursts. Wang *et al.* [27] estimated the afterglow parameters for GRB 990123, which differ from those for GRBs 970508 and 911214 by a higher density, $n \approx 800$ cm^{-3}, and a smaller magnetic-field strength, $\epsilon_B \approx 10^{-6}$. Their observations of the optical flare yielded $\gamma_0 \sim 1200$. For such a large γ_0, the afterglow peaks at $t_\gamma \approx 0.1$ s, and its peak flux must be $\sim 3 \times 10^{-6}$ erg s^{-1} cm^{-2}, i.e., of the order of the flux

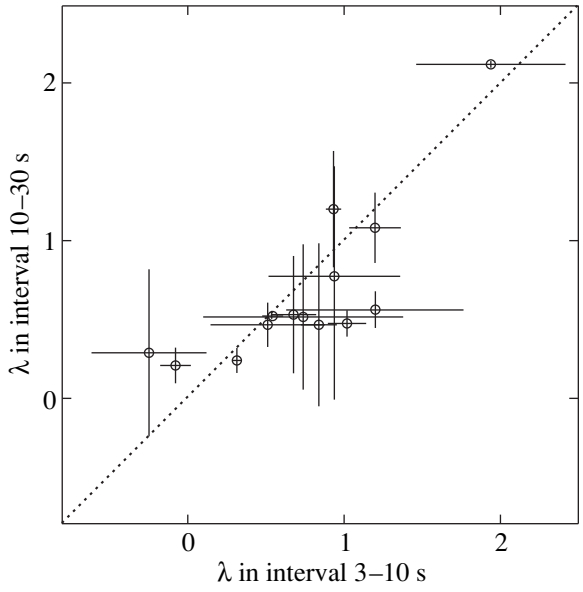

Fig. 6. Effective spectral indices in the interval 10–30 s versus spectral indices in the interval 3–10 s.

Table

Time interval	F_ν, erg s^{-1} cm^{-2}	γ_0	z	E_{52}	ϵ_e	ϵ_B	n, cm^{-3}
(1–3) s	$<10^{-8}$	<360	>0.5	*	*	*	<3
″		$=10^3$	>2.1	<0.03	<0.007	$<3\times10^{-6}$	$<3\times10^{-4}$
(3–10) s	$<5\times10^{-9}$	<270	>1.1	<0.07	<0.03	$<10^{-4}$	<0.2
″		$=10^3$	>2.1	<0.07	<0.01	$<10^{-5}$	$<3\times10^{-5}$
(10–30) s	$<3\times10^{-9}$	<180	>1.5	<0.2	<0.03	$<10^{-4}$	<0.01

* The limit on the flux gives no constraint if the remaining parameters are typical.

during the burst itself. The flux becomes lower than $\sim3\times10^{-9}$ erg s^{-1} cm^{-2} at $t\approx100$ s, which is approximately equal to the duration of GRB 990123. This set of parameters is not suitable for short GRBs under the assumption that their sources lie at cosmological distances. However, the significant differences between short bursts and bursts with a duration $\Delta T\gtrsim1$ s discussed above (see Sect. 3) suggest that the fireball parameters for short GRBs could also differ markedly from those for long GRBs.

ACKNOWLEDGMENTS

I wish to thank the Russian Foundation for Basic Research for financial support (project nos. 96-15-96930 and 97-02-17693).

REFERENCES

1. S. R. Kulkarni, S. G. Djorgovski, S. C. Odewahn, *et al.*, Nature, 1999 (in press); astro-ph/9902272.
2. W. K. H. Schmidt, Nature **271**, 525 (1978).
3. J. H. Krolik and E. A. Pier, Astrophys. J. **373**, 277 (1991).
4. T. Piran, Phys. Rep. **314**, 575 (1999); astro-ph/9810256.
5. E. E. Fenimore, C. Madras, and S. Nayakshin, Astrophys. J. **473**, 998 (1996).
6. R. Sari and T. Piran, Astrophys. J. **485**, 270 (1997); astro-ph/9701002.
7. C. D. Dermer and K. E. Mitman, Astrophys. J. Lett. **513**, L5 (1999).
8. J. I. Katz and T. Piran, Astrophys. J. **490**, 772 (1997).
9. R. Sari, T. Piran, and R. Narayan, Astrophys. J. Lett. **497**, L17 (1998); astro-ph/9712005.
10. R. Sari and T. Piran, Astron. Astrophys., 1999 (in press); astro-ph/9901105; astro-ph/9901338.
11. R. Wijers, M. Rees, and P. Mészáros, Mon. Not. R. Astron. Soc. **228**, L51 (1997).
12. T. J. Galama, R. A. Wijers, M. Bremer, *et al.*, Astrophys. J. Lett. **500**, L97 (1998).
13. R. A. Burenin, A. A. Vikhlinin, O. V. Terekhov, *et al.*, Pis'ma Astron. Zh. **25**, 483 (1999).
14. A. Tkachenko, R. Burenin, O. Terekhov, *et al.*, 3rd INTEGRAL Workshop, 1999 (in press).
15. T. W. Giblin, J. van Paradijs, C. Kouveliotou, *et al.*, Astrophys. J. Lett. **524**, L47 (1999).
16. C. Akerlof, R. Balsano, S. Barthelmy, *et al.*, Nature, 1999 (in press); astro-ph/9903271.
17. R. A. Wijers and T. J. Galama, Astrophys. J., 1999 (in press); astro-ph/9805341.
18. R. Jager, W. A. Mels, A. C. Brinkman, *et al.*, Astron. Astrophys., Suppl. Ser. **125**, 557 (1997).
19. O. V. Terekhov, D. V. Denisenko, V. A. Lobachev, *et al.*, Pis'ma Astron. Zh. **20**, 323 (1994) [Astron. Lett. **20**, 265 (1994)].
20. M. Tavani, Astrophys. J. Lett. **497**, L21 (1998); astro-ph/9802192.
21. T. Piran and A. Shemi, Astrophys. J. Lett. **403**, L67 (1993).
22. G. J. Fishman, C. A. Meegan, R. B. Wilson, *et al.*, Astrophys. J., Suppl. Ser. **92**, 229 (1994).
23. W. S. Paciesas, C. A. Meegan, G. N. Pendleton, *et al.*, Astrophys. J., Suppl. Ser. **122**, 465 (1999).
24. A. Tkachenko, O. Terekhov, R. Sunyaev, *et al.*, Astrophys. Space Sci. **231**, 131 (1995).
25. S. V. Golenetskij, E. P. Mazets, R. L. Aptekar, and V. N. Ilinskij, Nature **306**, 451 (1983).
26. J. Granot, T. Piran, and R. Sari, Astrophys. J. **513**, 679 (1999).
27. X. Wang, Z. Dai, and T. Lu, Mon. Not. R. Astron. Soc., 2000 (submitted); astro-ph/9906062.

Translated by V. Astakhov

Astronomy Letters, Vol. 26, No. 5, 2000, pp. 277–284. Translated from Pis'ma v Astronomicheskiĭ Zhurnal, Vol. 26, No. 5, 2000, pp. 333–341.

The Polar Stellar Ring and Dark Halo of NGC 5907

V. P. Reshetnikov* and N. Ya. Sotnikova

Astronomical Institute, St. Petersburg State University, Bibliotechnaya pl. 2, Petrodvorets, 198904 Russia

Received December 29, 1998; in final form, November 11, 1999

Abstract—Numerical simulations of the disruption of a dwarf companion moving in the polar plane of a massive galaxy are presented. The constructed model is compared with observational data on the recently discovered low-surface-brightness stellar ring around the galaxy NGC 5907. Constraints on the ring lifetime (≤1.5 Gyr after the first approach of the galaxies), on the structure of the companion—the ring precursor, and on the mass of the dark halo of the main galaxy in whose gravitational field the companion moves are provided. The dark-halo mass within 50 kpc of the NGC 5907 center cannot exceed 3 or 4 "visible" masses. *© 2000 MAIK "Nauka/Interperiodica".*

Key words: *galaxies, groups and clusters of galaxies, intergalactic gas*

1. INTRODUCTION

In recent years, many new approaches to studying the distribution of mass, in particular, dark mass, in galaxies of various types have appeared because of the progress in observing techniques and computer simulation methods. These include methods based on gravitational lensing [1], on the search for patterns in the variations of the H I layer thickness along the galactic radius [2], on the kinematic study of systems of planetary nebulae [3] and dwarf galaxies [4], as well as on the investigation of the dynamics of precessing dust disks in early-type galaxies [5] and circumgalactic polar structures [6]. One of the most interesting and promising ways of inferring the characteristic parameters of dark halos is to analyze the morphology and kinematics of transient, relatively short-lived structures produced by gravitational interaction between galaxies—tidal tails, bars, and the remnants of companions disrupted by interaction [7–11].

Here, we report the results of our numerical simulations of the large-scale, low-surface-brightness optical feature discovered around the galaxy NGC 5907. By all appearances, this structure results from the disruption of a low-mass companion near a massive spiral galaxy. We discuss the results of our calculations in the context of dark-halo effects on this process.

2. THE GALAXY NGC 5907

NGC 5907 is a late-type spiral (Sc) galaxy seen at a large angle to the line of sight ('edge-on') (see Fig. 1a). The galaxy lies relatively nearby (its distance is 11 Mpc for H_0 = 75 km s^{-1} kpc^{-1}), its optical radius ($R_{\rm opt}$) is 19.3 kpc, and the exponential disk scale is 5.7 kpc [12]. Its absolute magnitude is $M_B = -19.10$ ($L_B = 6.8 \times 10^9\ L_\odot^B$). The planes of the gaseous and stellar disks of the galaxy exhibit a large-scale warping [13, 14]. Since no close companions of comparative (or even considerably lower) luminosity have been found near NGC 5907, it has long been considered to be the prototype of noninteracting galaxies with warped equatorial planes. Such objects are very rare and are dynamical puzzles, because interaction with the ambient environment is believed to be mainly responsible for the formation of large-scale warping of galactic planes [15].

In recent years, the view of NGC 5907 as an isolated object has been called into question. Sackett *et al.* [16] discovered that the galaxy is surrounded by an extremely faint ($\mu_R \geq 25^m$ arcsec^{-2}) optical shell, a halo. The existence of this shell was subsequently confirmed by *B*, *V*, and *I* observations [17, 18] and *J*, *H*, and *K* data [19, 20]. Lequeux *et al.* [18] found the color indices of the halo to be typical of the old stellar population of elliptical galaxies. They assumed that the stellar halo around NGC 5907 was produced by the disruption of a relatively low-mass (~$3 \times 10^{10}\ M_\odot$) elliptical galaxy near it. This assumption was illustrated by numerical calculations.

Shang *et al.* [21] reported the discovery of an even fainter (than the halo) ring-shaped feature around NGC 5907 ($\mu_R \sim 27$–28^m arcsec^{-2}). This feature is similar in shape to an ellipse elongated along the galaxy's minor axis, so that the ring turns out to be in the circumpolar galactic plane. The galaxy nucleus lies approximately at the focus of this ellipse (see Fig. 1b). The major axis of the feature itself (~43 kpc) is comparable to the optical diameter of NGC 5907. The total optical luminosity of the ring does not exceed 1% of the galaxy luminosity, and its color index $R - I \sim 0.9$ corresponds to the old stellar population. No H I line emission was detected

* E-mail address for contacts: resh@astro.spbu.ru

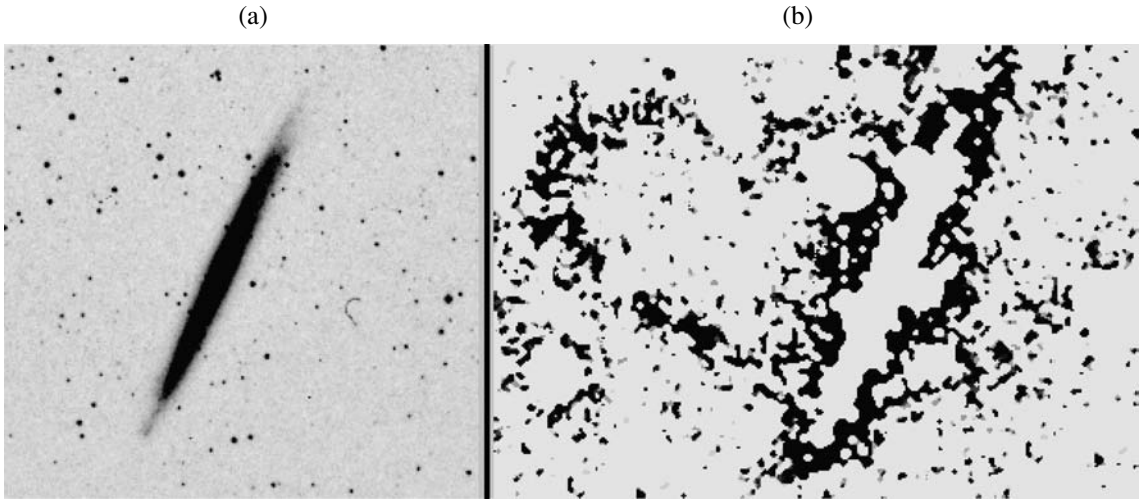

Fig. 1. (a) Reproduction of the NGC 5907 image based on the Digital Sky Survey (DSS)[1]; (b) image of the galaxy's outer regions [21]. To enhance the contrast, the bright central region of NGC 5907 and all foreground stars were removed from the image by masking. The image height is 14′.5; north is at the top, and east is to the left.

from the ring ($M(\mathrm{HI}) \leq 10^8\,M_\odot$), nor are there any traces of Hα and O[III] emission. The authors of the discovery suggested that the ring-shaped feature was a tidal remnant of the dwarf spheroidal galaxy captured by NGC 5907. Shang *et al.* [21] also discovered a dwarf companion with a radial velocity close to that of the central galaxy within 37 kpc of the NGC 5907 center.

It follows from the above data that NGC 5907 can no longer be considered as an isolated galaxy. By all appearances, the peculiarities of its optical structure suggests an ongoing interaction with its low-mass companions.

To test the assumption that the large-scale circumpolar stellar ring is produced by the accretion of a dwarf galaxy onto NGC 5907, we performed a series of numerical simulations, which are describe below.

3. MODEL AND COMPUTATIONAL TECHNIQUE

In the computations, the potential of the main galaxy was assumed to be known. As for the companion, we considered two alternative cases: a model of test particles in the external potential of the companion and a self-gravitating companion.

In the first case, we assumed the companion to be disrupted completely at the time of the closest approach of the galaxies, following which the particles continue to move in the field of the massive galaxy alone.

We simulated the evolution of the self-gravitating companion by using the NEMO package [22]. This is a freeware package designed to numerically solve gravitational *N*-body problems. It consists of subroutines for specifying initial configurations of stellar–dynamical systems (including many standard models) and subroutines for simulating the evolution of these systems based on various numerical schemes. In our computations, we used the scheme for constructing an "hierarchical tree" [23]—a special data structure in which all gravitating particles are separated into different groups, depending on the degree of closeness to the point at which the gravitational potential is determined. The contribution from close particles to the potential is calculated by a simple summation, while the groups of distant particles are treated as a single object. The potential produced at a given point by the distant groups of particles is expanded into a series in which the monopole and, occasionally, quadrupole terms are retained. The maximum number of particles used in our numerical simulations is $N = 100\,000$. In this case, we managed to suppress substantially the effects of pair relaxation and to trace the evolution of the disrupted companion on time scales of ~4–5 Gyr.

According to observations (see Sect. 2), the luminosity of the ring-shaped structure formed from the disrupted companion is much lower than that of the main galaxy. We therefore assumed the mass of the companion itself to be also sufficiently small (~10^{-3} of the mass of the main galaxy). This allowed us to ignore dynamic friction and disregard possible energy exchange between the main galaxy and the companion (see, e.g., [24])

3.1. The Central Galaxy

For the central galaxy, we considered a model consisting of three components: a disk, a bulge, and a dark halo. The disk potential was represented by Miyamoto–Nagai's potential [25]

[1] The Digitized Sky Surveys were produced at the Space Telescope Science Institute under US Government grant NAG W-2166.

Table 1. Models of the mass distribution in NGC 5907

Model	Component	Scale, kpc	Mass within $R_{opt} = 19.3$ kpc, $10^{10} M_\odot$	$r_\odot$, kpc
1	Bulge	1	1.3	–
	Disk	5	9.0	–
		1		
	Halo	20	13.5	18
2	Bulge	1	1.3	–
	Disk	5	9.0	–
		1		
	Halo	20	5.0	∞
3	Bulge	1	1.3	–
	Disk	5	9.0	–
		1		
	Halo	20	13.5	∞

$$\Phi_d(x, y, z) = -\frac{GM_d}{[x^2 + y^2 + (b_d + \sqrt{z^2 + a_d^2})^2]^{1/2}}, \quad (1)$$

where M_d is the disk mass, and a_d and b_d are the parameters characterizing the scale of the mass distribution in the disk.

The galactic bulge was described by Plummer's sphere

$$\Phi_b(r) = -\frac{GM_b}{(r^2 + a_b^2)^{1/2}}, \quad (2)$$

where M_b is the bulge mass, and a_b is the potential-smoothing scale.

The mass distribution in the dark halo of the main galaxy was specified by using the model of a mass-limited isothermal sphere, starting from some distance from the nucleus:

$$M_h(r) = \frac{M_{h0}}{r_c}\left(r - a_h \arctan\left(\frac{r}{a_h}\right)\right)\left(1 - e^{-\frac{r_c}{r}}\right), \quad (3)$$

where M_{h0} is the total mass of the halo, and a_h is the radius of the halo nucleus. The parameter r_c was introduced to avoid the divergence of mass at large distances in the isothermal model. Up to distances of the order of r_c, the halo mass density varies as $\propto r^{-2}$, while the mass $M(r)$ increases as $\propto r$. Starting from r_c, the density drops abruptly, and the mass tends to a finite value of M_{h0}.

In a number of simulations, we did not introduce a restriction by mass. In this case, the density distribution in the isothermal sphere was taken in ordinary form

$$\rho_h(r) = \frac{\rho_{h0}}{1 + (r/a_h)^2}. \quad (4)$$

The model parameters were chosen in such a way that the rotation curve within the optical radius (19.3 kpc) was close to the observed one. The model of mass distribution in NGC 5907 we used is similar to that described in [26] (see also [18]). Table 1 gives parameters of the main galaxy for our three cases. In all cases, the rotation curve has a flat portion in the range 8 to 30 kpc (Fig. 2).

3.2. The Companion

We considered two companion models (see Table 2). One of them is Plummer's spherically-symmetric model

$$\Phi_s(r) = -\frac{GM_s}{(r^2 + a_s^2)^{1/2}}, \quad (5)$$

where M_s is the companion mass, and a_s is the scale length of the mass distribution.

As was already noted above, the choice of companion mass [$(2–5) \times 10^8\ M_\odot$)] was constrained by the observed optical luminosity of the ring, which does not exceed 1% of the NGC 5907 luminosity. For the above companion masses and the total luminosity of the feature under consideration ($\leq 7 \times 10^7\ L_\odot^B$), we found the mass-to-light ratio to be $M_s/L_s(B) \geq 3–7$, in agreement with data for actual dwarf galaxies [27].

Table 2 gives line-of-sight velocity dispersions $\sigma_0 = [GM_s/6a_s]^{1/2}$ for the models of dwarf spheroidal companions. These values also agree with the observed σ_0 for dwarf spheroidal galaxies (see, e.g., the parameters of NGC 147 and NGC 185 in the review [27]).

In the second case, the companion was represented by a disk galaxy with an exponential density distribu-

Table 2. Models of the companion

Disk companion	Exponential scale, kpc	Vertical scale, kpc	Mass, $10^8 M_\odot$
	0.4	0.08	2
			5
Spheroidal companion	Scale (a_s)	σ_0, km s^{-1}	Mass, $10^8 M_\odot$
	0.4	19	2
		30	5

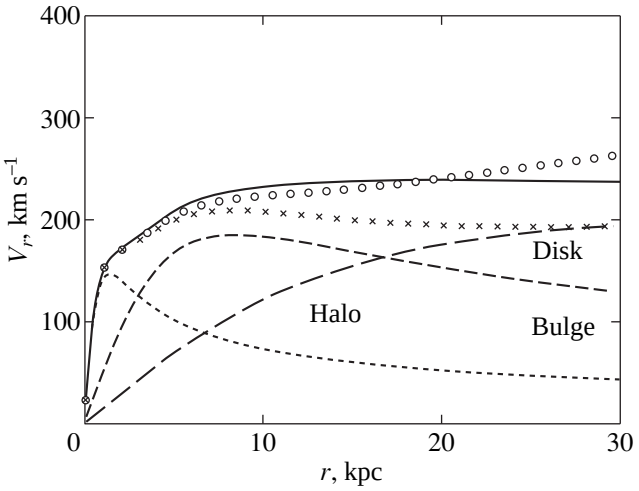

Fig. 2. Rotation curve of NGC 5907. The solid line indicates the rotation curve for model 1, and the dashed lines indicate the contributions of different components. The rotation curves for models 2 and 3 are represented by crosses (×) and circles (○), respectively.

tion and a vertical-to-radial scale ratio of 1 : 5 (Table 2). The Toomre parameter was set equal to $Q_T = 1.5$.

3.3. The Orbit

The companion was assumed to move in the polar plane of the main galaxy (*xz* plane). The initial coordinates of the companion are $x_0 = 0$, $y_0 = 0$, and $z_0 = 52$ kpc. We chose the initial velocity from the following considerations. We specified the distance of the closest approach, $r_{min} = 13$ kpc, and computed the galaxy mass $M(r_{min})$ within r_{min}. If the companion moved in the field of a point mass $M(r_{min})$, then its velocity at point (x_0, y_0, z_0) would correspond to the velocity at the apocenter of an elliptical orbit with eccentricity $e = 0.6$ and semimajor axis $a = (z_0 + r_{min})/2 = 32.5$ kpc. It is this value that we took as the initial velocity. Figure 3 shows the companion orbit for the three models of the main galaxy. The distance of the closest approach proved to be less than the initially specified value (~8–9 kpc) for all three orbits.

For the disk companion, we considered three different initial orientations of the disk plane with respect to the orbital plane and the equatorial plane of the galaxy:

(a) The disk plane is parallel to the galaxy's equatorial plane;

(b) The disk plane is perpendicular both to the galaxy's equatorial plane and to the orbital plane (in the orbital plane, the companion is seen edge-on);

(c) The disk companion moves edge-on with respect to the galaxy plane, with the disk being seen face-on in the orbital plane.

Our computations revealed virtually no differences between the direct and retrograde motions of the disk companion. This is because the stars at the opposite ends of the disk undergo virtually the same perturbation due to the small size of the companion itself. Thus, the difference between the perturbation durations for the direct and retrograde rotation of the companion is of no importance. Below, we report the results of our computations only for direct motions.

4. RESULTS OF COMPUTATIONS

4.1. Test Particles

We assumed that the companion was completely disrupted when the separation between the galaxies was at a minimum. Subsequently, its remnants continue to move only in the gravitational field of the main galaxy. In the course of time, the companion remnants stretch along the initial orbit following its individual turns. We traced the evolution of the disrupted companion within 1.4 Gyr after the first closest approach of the galaxies. Figures 4a and 4b show the results of our computations for the two (spherical and disk) companion models. The spatial orientation of the disk companion corresponds to case (b) in Subsect. 3.3. The main galaxy is represented by model 1 (Table 1).

We see that a diffuse loop-shaped structure resembling that in Fig. 1b forms around the galaxy as the

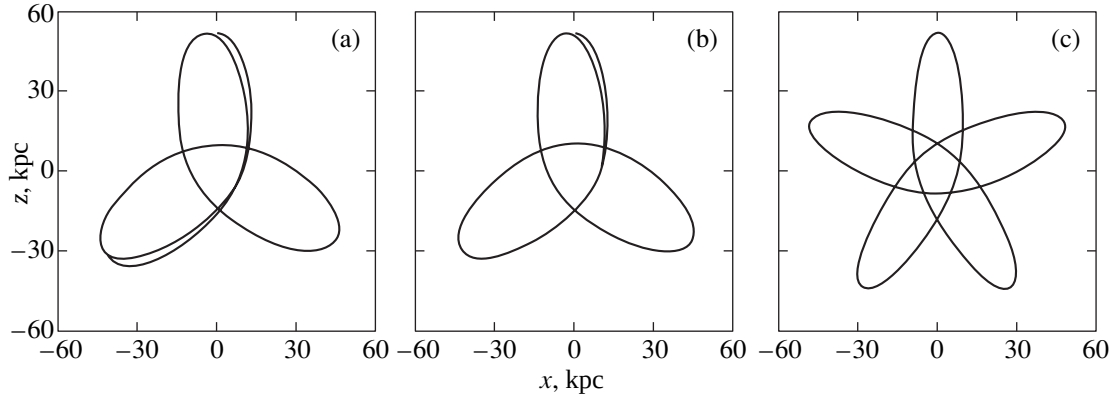

Fig. 3. The orbit of the companion for models 1 (a); 2 (b), and 3 (c).

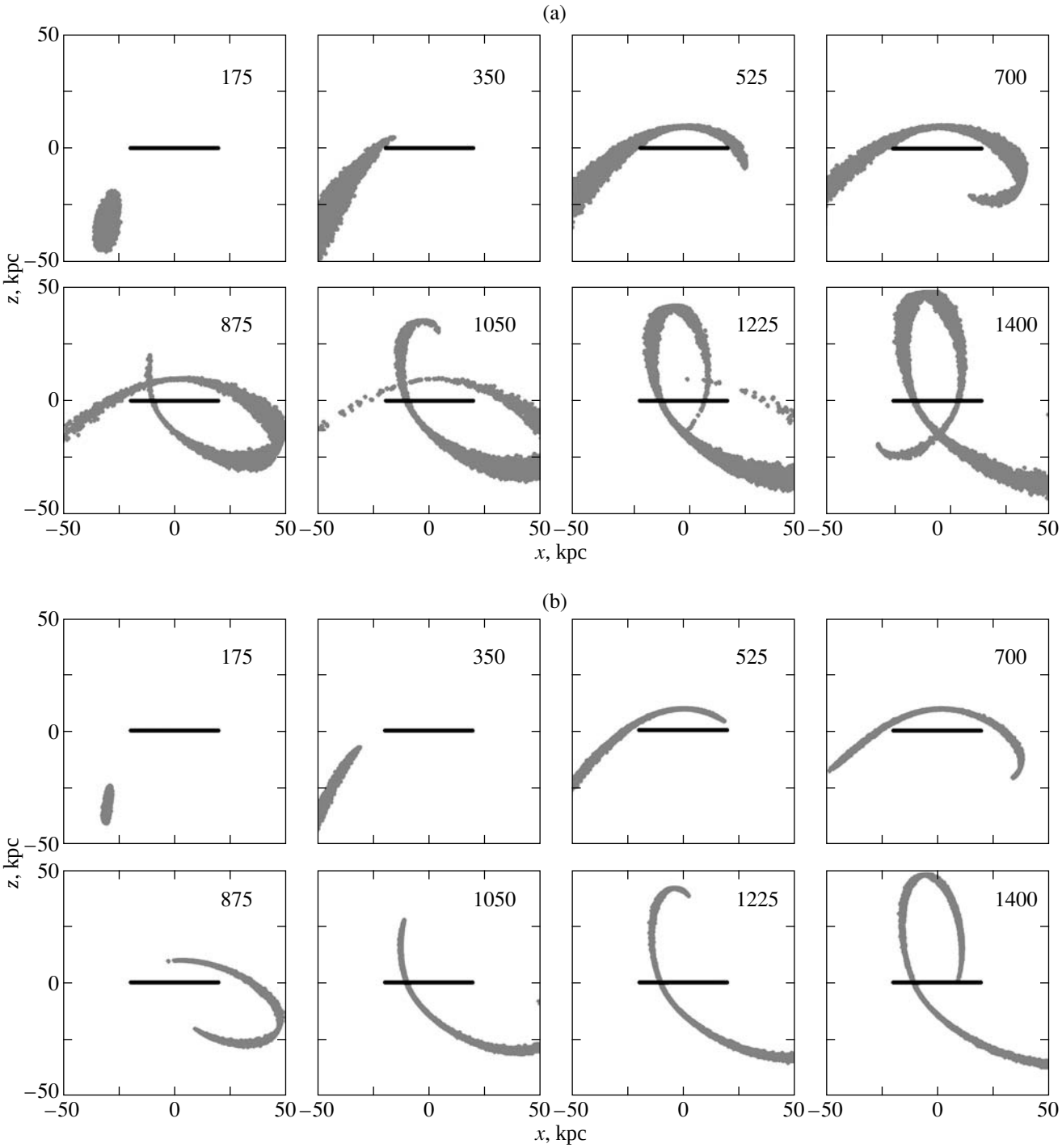

Fig. 4. Evolution of the structure of the dwarf companion in the model of test particles in projection onto the *xz* plane: (a) spherical companion and (b) disk companion. The disk companion was initially located in the *yz* plane. The companion mass is $2 \times 10^8\ M_\odot$ in both cases. A straight-line segment indicates the orientation of the disk of the main galaxy. The segment length corresponds to the optical diameter of NGC 5907. The size of each frame is 100×100 kpc; the time (in Myr) elapsed since the first passage of the companion through the pericenter of the orbit is shown in the upper right corner.

companion is disrupted (by $t \sim 1.4$ Gyr after the first closest approach). Note also that the numerical model predicts the existence of an extended linear feature going off the simulated loop to the left and downward (Fig. 4). NGC 5907 also shows evidence of such a structure (Fig. 1b). Since the companion remnants move exactly in the polar plane, the loop is not washed out by differential precession. For the disk companion, the loop is thinner because of the smaller stellar velocity dispersion along the *x* axis.

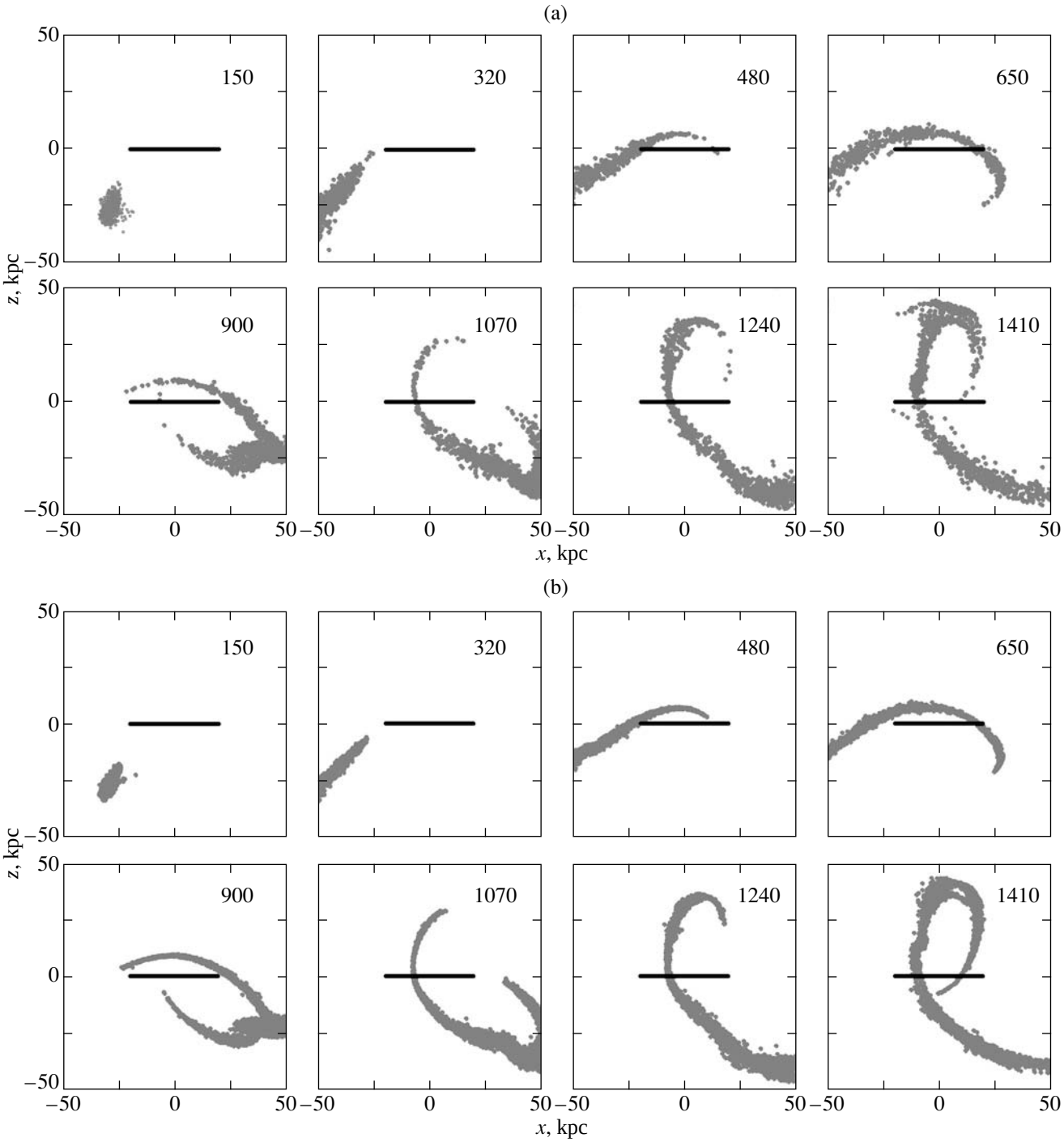

Fig. 5. Same as Fig. 4 but for the model of a self-gravitating companion.

In model 2 (Table 1), the potential of the halo corresponds to the potential of a standard isothermal sphere with infinite total mass. In order that the total mass of dark matter within the region of companion motion (~52 kpc) be approximately the same as that in model 1, we reduced the halo mass within R_{opt}. Our computations show that a structure similar to that in Figs. 4a and 4b is also formed in this case.

It also follows from our computations that model 3 (Table 1) is unacceptable. In this model, the mass of the halo within the region of companion motion is considerably higher than that in models 1 and 2. We see from Fig. 3 that, in this case, the apparent flattening of the turns of the orbit along which the disrupted companion stretches is too small compared to what is observed in the ring-shaped structure of NGC 5907. Consequently,

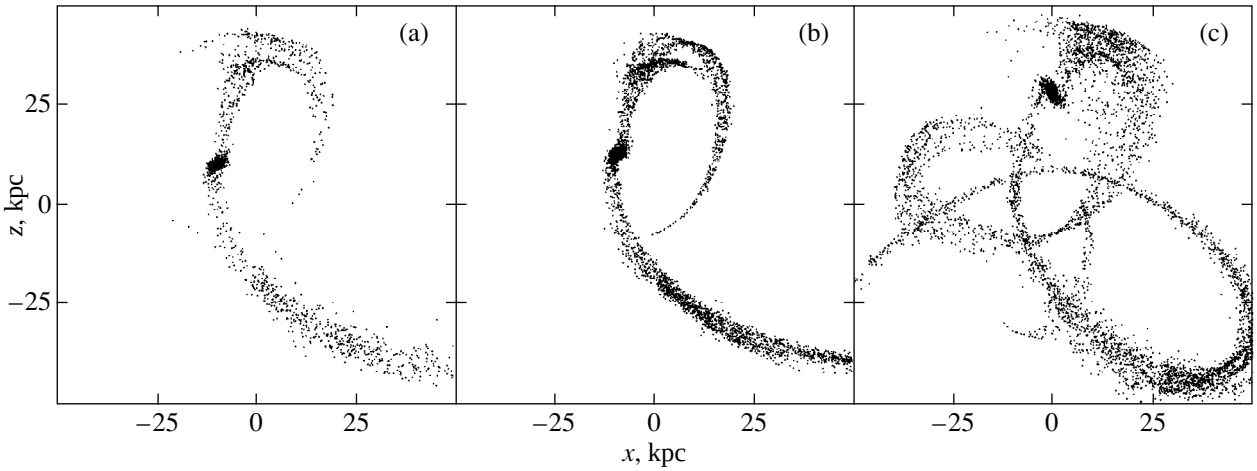

Fig. 6. Morphology of the ring produced by the companion disruption: (a) the model of a spherical companion (t = 1.41 Gyr); (b) early (t = 1.41 Gyr) and (c) late (t = 3.51 Gyr) stages of the ring evolution for the model of a disk companion.

even the morphology itself of the ring-shape feature constrains the mass of the dark halo of NGC 5907 within the ring, M_h (r < 52 kpc)/($M_d + M_b$) ≈ 3–4.

4.2. The Self-Gravitating Companion

To describe the companion disruption in a self-consistent way, we computed several models in the gravitational N-body problem. Figures 5a and 5b show the evolution of the spherical and disk companions. We used N = 50 000 and N = 100 000 in the former and latter cases, respectively. It is not accidental that we took such a large number of particles. We wished to trace the evolution of the companion on time scales of 2–4 Gyr. For a smaller number of particles, this evolution is largely determined by numerical relaxation effects, which cause artifical heating of the system. The relaxation time t_{rh} for a companion with the potential (5) is given by [28]

$$t_{rh} = 0.2\frac{N}{\ln(0.4N)}\sqrt{\frac{a_s^3}{GM_s}}. \quad (6)$$

For N = 50000, $M_s = 2 \times 10^8\ M_\odot$, and a_s = 0.4 kpc, this yields about 8 Gyr.

Qualitatively, the formation of the stellar ring is similar in pattern to that described in Subsect. 4.1. The principal difference is that, even 1.4 Gyr after the galaxies approached each other for the first time, the nucleus of the companion proves to be virtually undisrupted (see Figs. 6a and 6b). By that time, the companion had crossed four times the equatorial plane of the main galaxy. Note that the disk companion is disrupted to a greater extent than the spherical one. Accordingly, the surface density of the ring formed from the remnants of the disk companion (0.1–0.5 $M_\odot$ pc^{-2}) is considerably (approximately a factor of 3) higher than that in the case shown in Fig. 6a. Such a density is in good agreement with the observed surface brightness of the ring (Sect. 2).

Figure 6c shows the late disruption stage of the disk companion (after eight crossings of the galaxy's equatorial plane). A small nucleus is still bound, but the companion remnants no longer form a coherent ring-shaped feature but are distributed along several turns of the orbit. Similar computations by other authors (see, e.g., [29]) on long time scales also yielded highly irregular structures. This constrains the lifetime of the stellar loop observed in NGC 5907 (< 1.5 Gyr).

Note that the behavior of stars differs from the behavior of gas. The gas captured by a massive galaxy forms a long-lived ring, which can give rise to objects called polar-ring galaxies [29–31]. The fate of the stellar ring in NGC 5907 is different: in the course of time, it must turn into a diffuse, virtually unobservable structure.

5. CONCLUSION

Our computations have led us to several conclusions:

(1) The ring-shaped feature discovered around NGC 5907 is satisfactorily described as the remnant of a disrupted low-mass (~10^{-3} of the mass of the main galaxy) companion.

(2) The structure of the stellar loop can be better explained by assuming that the dwarf companion was a disk rather than a spherical one.

(3) In NGC 5907, we are apparently observing a relatively early stage of companion disruption (<1.4 Gyr after the first closest approach of the galaxy and its companion). At late stages, the companion matter is distributed simultaneously along several turns of the orbit.

(4) The ring morphology allows the mass of the dark halo of the main galaxy within the ring radius to be constrained: $M_h(r < 52\ \text{kpc})/(M_d + M_b) \approx 3$–4.

(5) Deep images of galaxies can apparently reveal faint features in some of them similar to the stellar ring around NGC 5907. Our Galaxy is one of such examples. Its dwarf companion in Sagittarius, which was partly disrupted by tidal forces from the Galaxy, forms an extended structure (with a length of 68° or ~30 kpc [32]) consisting of moving stellar groups (the results of numerical simulations are presented in [33]). However, it would be unreasonable to expect the detection of a large number of such loop-shaped features. First, a special encounter geometry is required for a stellar ring to be formed in the polar plane. Second, in contrast to classical polar-ring galaxies, a stellar ring is observed only when the companion matter is distributed along one of the trajectory turns. The structure becomes blurred at late stages and can hardly be detected, because the surface brightness decreases sharply.

ACKNOWLEDGMENTS

We are grateful to Dr. Shang (Texas University), who provided a deep image of NGC 5907 (Fig. 1b). This study was supported by the Integration Program (project no. 578), as well as by the Competitive Center for Basic Science of the Ministry of General and Professional Education and the Russian Foundation for Basic Research (project nos. 97-02-18212 and 98-02-18178).

REFERENCES

1. T. G. Brainerd, R. D. Blandford, and I. Smail, Astrophys. J. **466**, 623 (1996)
2. R. P. Olling, *Thesis Work* (Columbia Univ., New York, 1955).
3. X. Hui, H. C. Ford, K. Freeman, and M. A. Dopita, Astrophys. J. **449**, 592 (1995).
4. D. Zaritsky and S. D. M. White, Astrophys. J. **435**, 599 (1994).
5. T. Y. Steinman-Cameron, J. Kormendy, and R. H. Druisen, Astron. J. **104**, 1339 (1992).
6. B. C. Whitmore, D. B. McElroy, and F. Schweizer, Astrophys. J. **314**, 439 (1987).
7. J. Dubinski, Ch. Mihos, and L. Hernquist, Astrophys. J. **462**, 576 (1996).
8. Ch. Mihos, J. Dubinski, and L. Hernquist, Astrophys. J. **494**, 183 (1998).
9. N. Ya. Sotnikova and V. P. Reshetnikov, Pis'ma Astron. Zh. **24**, 97 (1998) [Astron. Lett. **24**, 73 (1998)].
10. N. Ya. Sotnikova and V. P. Reshetnikov, Izv. Ross. Akad. Nauk, Ser. Fiz. **62**, 1757 (1998).
11. K. V. Johnston, H. Zhao, D. N. Spergel, and L. Hernquist, astro-ph/9807243.
12. P. C. van der Kruit and L. Searle, Astron. Astrophys. **110**, 61 (1982).
13. R. Sancisi, Astron. Astrophys. **53**, 159 (1976).
14. T. Sasaki, Publ. Astron. Soc. Jpn. **39**, 849 (1987).
15. V. Reshetnikov and F. Combes, Astron. Astrophys. **337**, 9 (1998).
16. P. D. Sackett, H. L. Morrison, P. Harding, and T. A. Boroson, Nature **370**, 440 (1994).
17. J. Lequeux, B. Fort, M. Dantel-Fort, *et al.*, Astron. Astrophys. **312**, L1 (1996).
18. J. Lequeux, F. Combes, M. Dantel-Fort, *et al.*, Astron. Astrophys. **334**, L9 (1998).
19. R. J. Rudy, C. E. Woodward, T. Hodge, *et al.*, Nature **387**, 159 (1997).
20. P. James and M. M. Casali, Spectrum **9**, 14 (1996).
21. Zh. Shang, Zh. Zheng, E. Brinks, *et al.*, Astrophys. J. Lett. **504**, L23 (1998).
22. P. J. Teuben, ASP Conf. Ser. **77**, 398 (1995).
23. J. E. Barnes and P. Hut, Nature **324**, 446 (1986).
24. J. Binney and S. Tremaine, *Galactic Dynamics* (Princeton University Press, Princeton, 1987).
25. M. Miyamoto and R. Nagai, Publ. Astron. Soc. Jpn. **27**, 533 (1975).
26. S. Casertano, Mon. Not. R. Astron. Soc. **203**, 735 (1983).
27. M. Mateo, Ann. Rev. Astron. Astrophys. **36**, 435 (1998).
28. L. Spitzer and M. N. Hart, Astrophys. J. **164**, 399 (1971).
29. M. L. Weil and L. Hernquist, Astrophys. J. **405**, 142 (1993).
30. H.-W. Rix and N. Katz, in *Warped Disks and Inclined Rings around Galaxies*, Ed. by S. Casertano, P. D. Sackett, and F. H. Briggs (Cambridge Univ. Press, Cambridge, 1991), p. 112.
31. V. Reshetnikov and N. Sotnikova, Astron. Astrophys. **325**, 80 (1997).
32. M. Mateo, E. W. Olszewski, and H. L. Morrison, Astrophys. J. Lett. **508**, L55 (1998).
33. K. V. Johnston, D. N. Spergel, and L. Hernquist, Astrophys. J. **451**, 598 (1995).

Translated by A. Dambis

Astronomy Letters, Vol. 26, No. 5, 2000, pp. 285–296. Translated from Pis'ma v Astronomicheskiĭ Zhurnal, Vol. 26, No. 5, 2000, pp. 342–354.

Vorontsov-Velyaminov Rows: Straight Segments in the Spiral Arms of Galaxies

A. D. Chernin[1, 2]*, A. V. Zasov[1], V. P. Arkhipova[1], and A. S. Kravtsova[3]

[1] *Sternberg Astronomical Institute, Universitetskiĭ pr. 13, Moscow, 119899 Russia*
[2] *Tuorla Observatory, Turku University, 21500 Piikkio, Finland*
[3] *Moscow State University, Vorob'evy gory, Moscow, 119899 Russia*

Received May 21, 1999; in final form, November 20, 1999

Abstract—The phenomenon of rows—straight features in the spiral patterns of galaxies, which was discovered by Vorontsov-Velyaminov, is investigated. The rows are not artifacts; in several cases, they outline regular spiral arms almost over their entire lengths. The galaxies M 101, M 51, and a number of more distant spirals are used as examples to demonstrate major geometrical and physical properties of these structures. It is shown that the row lengths increase nearly linearly with distance from the disk center, and that the angle between adjacent rows is almost always close to $2\pi/3$. The galaxies with rows generally belong to moderate-luminosity Sbc–Sc systems with low rotational velocities, regular spiral patterns (Grand Design), and an H I content normal for these types of galaxies. Two types of rows are shown to exist, which differ in thickness and appear to be evolutionarily related. The formation mechanism of the rows should probably be sought in the peculiar behavior of the gas-compression wave in spiral density waves. © *2000 MAIK "Nauka/Interperiodica"*.

Key words: *galaxies, spiral pattern, Vorontsov-Velyaminov rows*

1. INTRODUCTION

Almost half a century ago, Vorontsov-Velyaminov [1–3] noticed extended structural features in spiral galaxies, which he called rows. They are "straightened, isolated segments of spiral arms … or isolated, linear features." According to Vorontsov-Velyaminov, these are not small or faint features for which a set of randomly arranged spots can be easily mistaken, but usually conspicuous large, bright spiral-arm segments.

Following this definition, we take such linear structures, whose lengths are comparable to their galactocentric distances (usually 5–15 kpc), as rows. They are often appreciably brighter (and bluer) than other spiral-arm segments in the same galaxy due to sites of intense star formation, which, in fact, produce these structural features.

The linear features are commonly observed in galaxies and may differ in nature. In some cases, they arise from mass ejection during the gravitational interaction of disk systems (tails or bars, which appear straight for a certain spatial orientation). The most dramatic example of this kind is NGC 1532, where a smooth, perfectly straight (in projection onto the sky) stellar band extends over $12'$ (~50 kpc) at a width equal to 1/30 of its length (see, e.g., [4]). However, since the tidal structural elements are not features of the disk spiral pattern (although they can be directly or indirectly associated with it), they do not belong to rows. The same is also true for such elongated features as galaxy bars.

Vorontsov-Velyaminov emphasized from the very outset that galaxies with rows occur rather commonly, although he gave few specific examples. In Section 8 (*Evidence of Magnetic-Like Phenomena*) of Chapter III in his book [5], Vorontsov-Velyaminov classified M 101, NGC 2805, NGC 3134, NGC 309, and NGC 3310 as galaxies with rows.

Of particular interest are galaxies with several rows in their spiral arms. These include the giant spiral M 101, which can be considered to be the archetype of this kind of spirals [5]. It is a nearby (at a distance of ≈5 Mpc) giant galaxy seen almost face-on. Its outer region contains two rows, each with a size of about 15 kpc, clearly distinguishable both in the blue or ultraviolet [6] and by the H I surface density distribution.

In this paper, we study galaxies (in most cases, seen almost face-on) with two or more rows in their spiral arms. Their percentage is estimated to be approximately 10% of the total number of objects in the list of galaxies that we are currently drawing up, in which rows can be detected or suspected using Palomar Sky Survey (PSS) images. In Sect. 2, we briefly review the currently available (not too numerous) results on our subject and consider the spiral patterns of nearby and well-studied galaxies (M 101 and M 51), which serve as a textbook example of Grand-Design spirals. In Sect. 3, we report the results of our study of 13 other galaxies

* E-mail address for contacts: chernin@sai.msu.ru

with two or more rows. A general discussion and conclusions are given in Sect. 4.

2. ROWS IN NEARBY GALAXIES

After Vorontsov-Velyaminov [3, 5] and, probably, independently of him, the existence of rows was pointed out by Arp [7], who noticed the linearity of the chains formed by H II regions in M 81 and found this to be surprising. The linear geometry of long spiral-pattern segments must actually be considered surprising, given that the large-scale structure of the gravitational potential relief associated with spiral density waves contains no linear segments. It should also be added that the rotation of galactic disks on scales of several kpc is by no means rigid, and, consequently, the rows are either short-lived or continuously renewable features. Since M 81 is one of the nearest spiral galaxies, the structure of its arms can be studied in great detail. However, the chains of star-forming regions observed in this galaxy are rather small in size and increase only slightly the local brightness of the spiral arms; therefore, such features can remain unnoticed when searching for rows in more distant galaxies.

Efremov mentioned the linear chains formed by stellar complexes in his book [8], which appears to contain the only (until recently) allusion to Vorontsov-Velyaminov as the discoverer of rows.

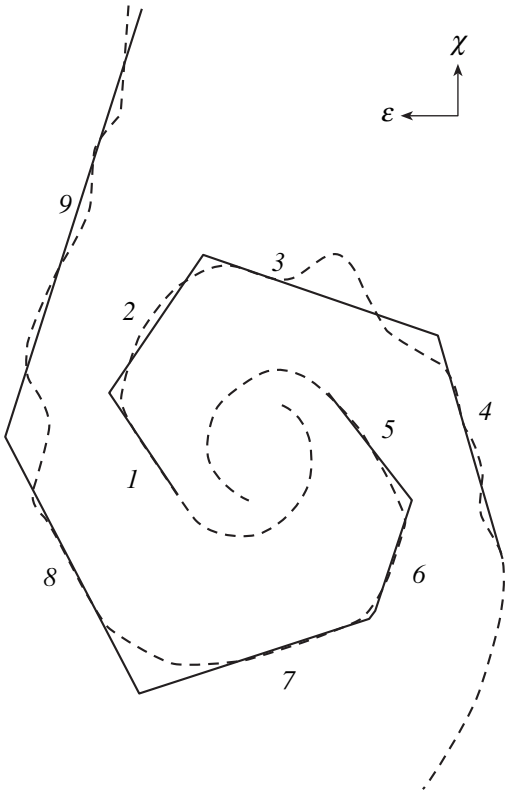

Fig. 1. Arrangement of rows in M 51. The dashed lines indicate the regions of maximum intensity of nonthermal radio emission [12].

This discovery has attracted no attention for several decades. Astronomers may have been cautiously distrustful because of several episodes in the history of studying spatial structures in the sky when regular patterns were seen where they were actually absent (channels on Mars, rings in the stellar distribution on Palomar maps, etc.). This kind of optical illusion is associated with the well-known peculiarity of percepting random geometric patterns, when the human eye and brain seek to connect points into simple sequences and figures. In the case of Vorontsov-Velyaminov rows, such a risk may also exist, especially where distant galaxies whose images were obtained with an insufficient angular resolution or overexposed are involved. However, the picture in nearby stellar systems is fairly clear, and in such galaxies as M 101, huge rows can be seen not only on optical photographs but also, as was pointed out by Vorontsov-Velyaminov [5], on H I maps.

Very interesting data on the spiral structure in M 101 has been obtained recently with the 38-cm ultraviolet telescope onboard the Endeavor Space Shuttle [6]. The overall distribution of stellar complexes scattered over the disk of this galaxy exhibits a complex large-scale spiral pattern in which two quasi-regular arms can be distinguished. The two huge rows mentioned by Vorontsov-Velyaminov [5] are located in the western arm. Waller *et al.* [6] found ten more linear chains with lengths in the range 5 to 20 kpc in this distribution. A more detailed analysis involving additional new data on the H I distribution [9], as well as maps of Hα emission and CO radio emission (see [10] and references therein), yields a slightly different picture: eight rows located in the regular spiral arms can be reliably identified; there are none of them in the flocculent, chaotic arms of the galaxy [11].

Turning to other nearby galaxies with multiple rows, we begin with the remarkable spiral M 51 in Canes Venatici, which is seen, like M 101, almost face-on. It has been served as a classic example of spiral galaxies for more than 150 years since Lord Ross discovered its spiral pattern in 1845. The geometry of its spiral pattern is outlined by bright rows of stellar complexes and, even more clearly, by sharp and narrow dark lanes at the inner edges of the arms. The lanes are clearly traceable virtually over the entire length of both main regular arms—see also the blue, yellow, and red photographs of M 51 in Vorontsov-Velyaminov's book [5].

Of particular importance is the fact that the line of maxima of synchrotron radiation [12] closely coincides with the dark lanes on optical photographs.

Collectively, the above data allow nine main rows to be distinguished in the two principal spiral arms of M 51 (Fig. 1). (Surprisingly, Vorontsov-Velyaminov did not notice very bright rows in this galaxy, while giving several other examples of rows in galaxies more

Table 1. Basic properties of the galaxies

NGC	Type	R, Mpc	V_r, km s^{-1}	Mb	Sp	$(B–V)_T^0$	M_{HI}/L	N_{str}
1	2	3	4	5	6	7	8	9
1232	SAB(rs)c	11.5	1603	–19.8	9	+0.63	0.29	9
2223	SB(r)bc	16	2660	–19.2	9	–	0.23	5
2942	SA(s)c	27	4423	–18.7	9	+0.57	0.35	4
2997	SA(s)c	7.6	1087	–19.3	9	+0.91	0.20	3
3631	SA(s)c	1.6	1156	–20.0	9	+0.58	0.23	3
3938	SA(s)c	6	809	–17.8	9	+0.52	0.32	7
4303	SAB(s)c	7.9	1566	–19.3	9	+0.53	0.21	3
4321	SAB(s)bc	11.5	1571	–20.3	12	+0.70	0.10	2
4535	SAB(rs)bc	10	1961	–19.4	9	+0.63	0.20	5
4548	SB(rs)b	11	490	–19.4	5	+0.76	0.04	3
5161	SA(s)c	3.2	2388	–17.0	(9)	+0.62	0.42	3
6946	SAB(rs)cd	5	48	–18.9	9	+0.80	0.17	8
7137	SAB(rs)c	14.5	1686	–17.8	(9)	+0.67	0.16	3

distant and much more poorly studied than M 51 in his book, besides M 101.) In each of the arms, the rows are virtually everywhere adjacent to one another; as a result, the arm geometry can be represented—in a somewhat simplified and schematic way—as a polygonal line over almost the entire arm length, except for the innermost disk region, where the arm structure is not traceable very well.

The row lengths measured in units of the largest distance from the center, in order of increasing numbers, are 0.35, 0.30, 0.60, 0.80, 0.85, 0.45, 0.50, 0.60, 0.80, and 0.85. As in M 101, the angle between adjacent rows is close to $2\pi/3$.

Comparing the geometries of the principal quasi-regular arms in M 51 and M 101, we can say that, in all cases, they are outlined by similar polygonal lines. Apart from the similarity of the bend angles of these lines, another property of the arms attracts attention: the lengths of the row segments increase nearly linearly with galactocentric distance [11].

The rows in nearby galaxies exhibit yet another remarkable property: they represent most frequently bright, blue spiral-arm segments. Each of them usually contains from 5 to 15–20 bright stellar complexes undergoing violent star formation. If there are superassociations in a galaxy, then the latter are, as a rule, in rows. Thus, for example, one of the western rows in M 101 contains the superassociation known as NGC 5462; the other brightest object in the same row, NGC 5461, can also be considered to be a superassociation. The brightest star-forming regions in M 51 are located in rows *1*, *2*, *3*, and *5*.

3. MORE DISTANT GALAXIES WITH ROWS: GENERAL PROPERTIES

Figure 2 shows examples of galaxies with several rows, which are more distant than M 101 and M 51. We selected the galaxies by using mostly images in the NASA Atlas of Galaxies [4] as objects with two or more rows in their spiral patterns. The galaxy photographs (except NGC 7137) were taken from this atlas. The *R*-band image of NGC 7137 was obtained by A. Moisseev and V. Chavyshyan with the 1-m Zeiss telescope at the Special Astrophysical Observatory of the Russian Academy of Sciences and is shown here from their kind permission. Schematic images of structural features in the galaxies are shown alongside the photos (the linear arm segments are indicated by heavy lines).

Table 1 lists the observed galaxy parameters. The first two columns give NGC galaxy numbers and morphological types of the galaxies, respectively. The distances to the galaxies (third column) correspond to the distance moduli estimated without using their cosmological velocities [13]. The fourth and fifth columns give the cosmological velocities from the RC3 catalog [14] and the absolute magnitudes corresponding to the apparent magnitude B_T^0 (from RC3), respectively. The types of spiral pattern from [15] (estimates for the galaxies absent in the above paper are given in parentheses) and the dereddened color index $(B–V)_T^0$ follow next. The eighth column contains the H I mass-to-light ratio (in solar units) estimated from the H I parameter in RC3 (the absolute magnitude of the Sun was assumed to be $M_B = 5.48$. The last column contains the probable number of rows in the galaxy.

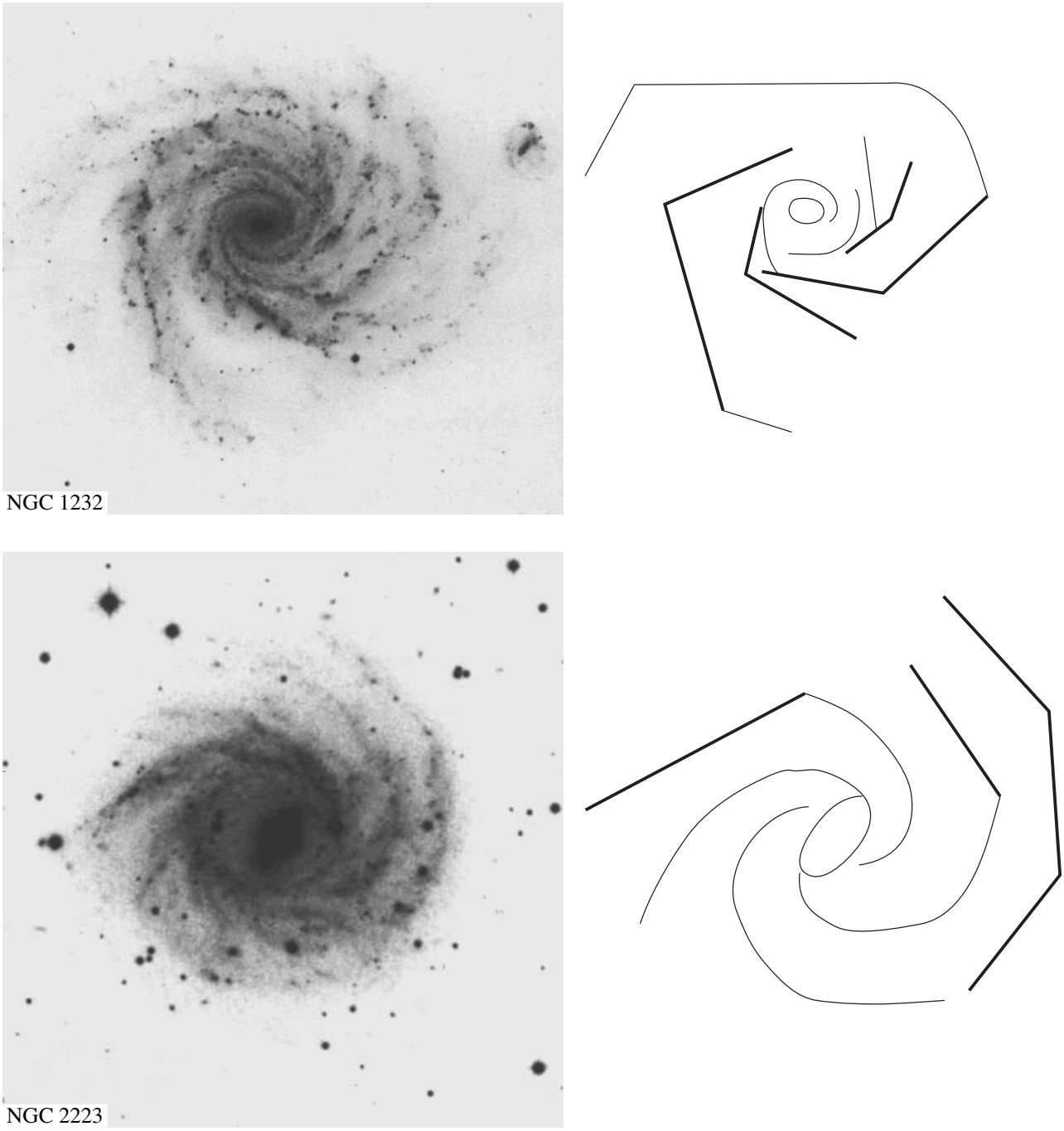

Fig. 2. Examples of galaxies with rows.

Below, we make brief comments on individual galaxies.

NGC 1232. Almost each spiral in this multiarm galaxy is crooked. The longest row is rather blurred, but contains a remarkably narrow, bright chain inside, which is apparently formed by H II regions.

NGC 2223. The most conspicuous rows are located at the ends of its spiral arms. In general, they are rather diffuse, although they are interspersed with bright H II regions. Overall, the galaxy exhibits a complex spiral pattern, which is asymmetric about the galaxy center.

NGC 2942. The rows here seem to be in the stage of disruption. The longest row has a diffuse structure and a low brightness.

NGC 2997. The image in the figure is overexposed, and it is better to use the NASA atlas [4]. Two adjacent rows are formed by narrow chains of H II regions. The total number of rows is apparently more than three.

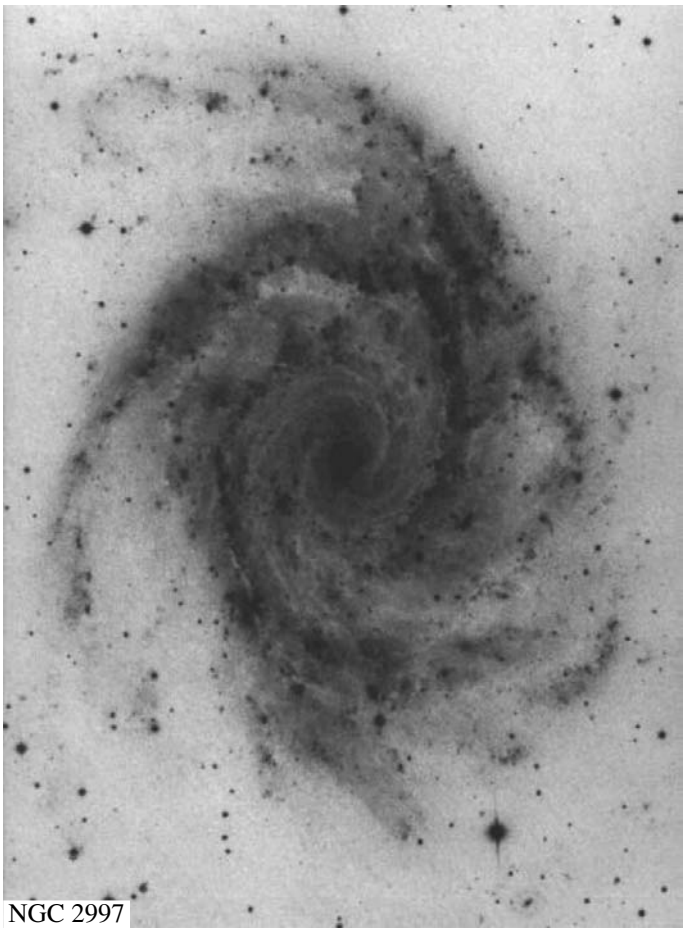

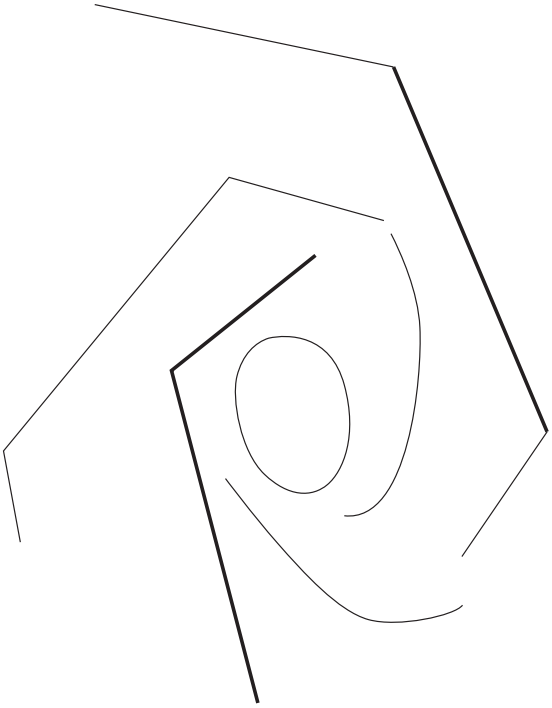

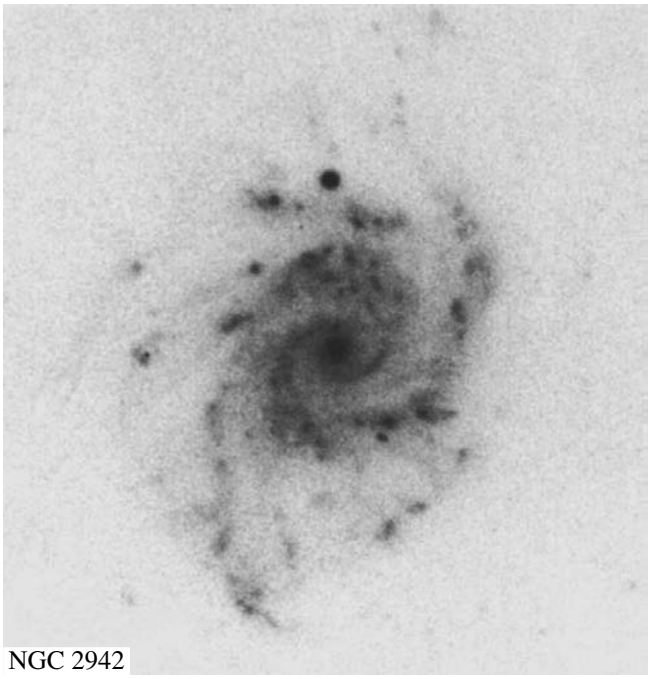

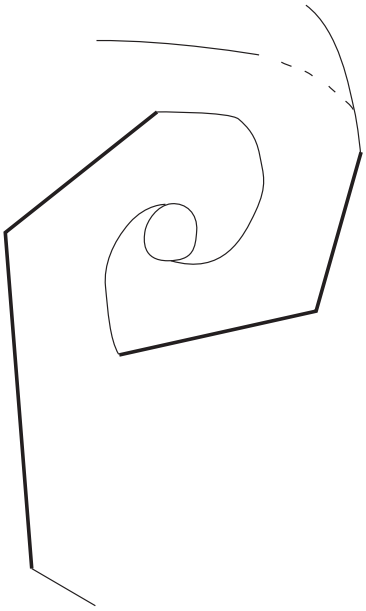

Fig. 2. (Contd.)

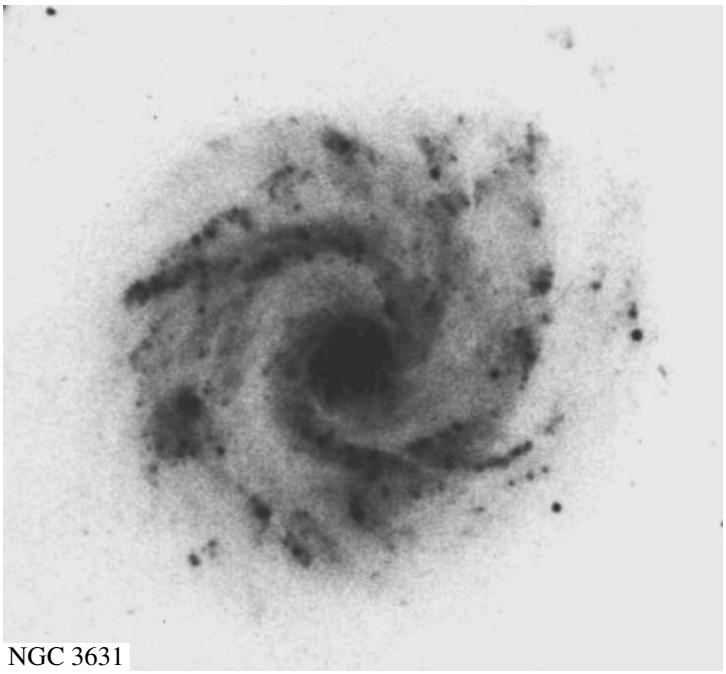

NGC 3631

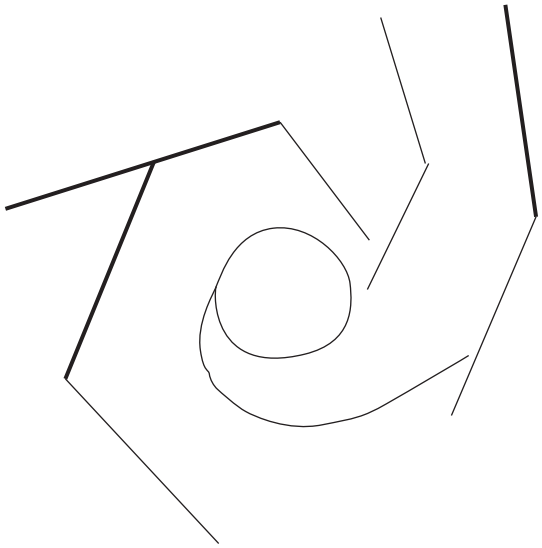

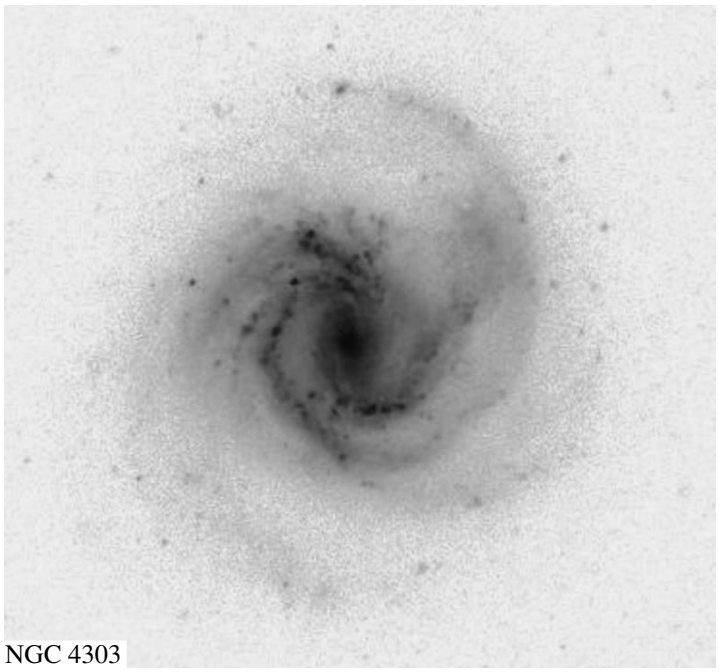

NGC 4303

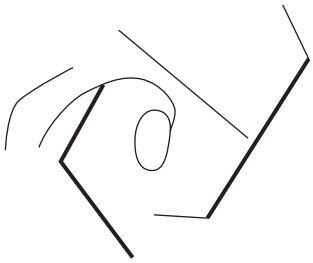

Fig. 2. (Contd.)

NGC 3631. The largest row, as it were splits the spiral arm into two. The only row in the galaxy NGC 5085 looks similarly (see [4]). Remarkably, the spiral on the diametrically opposite side also branches.

NGC 3938. The rows consist of individual bright H II regions with a relatively weak background between them. There may be more rows than are highlighted in the figure.

NGC 4303. Its two adjacent rows have unusually clear-cut outlines.

NGC 4321. The rows are rather blurred and appear as straightened segments of the principal spiral arms. Two long, linear (!) dust lanes are clearly seen on the inside of the largest row.

NGC 4535. Straightened segments are observed at the ends of the spiral arms. The blurred band connecting the end of the inner bright arm with the outer island of star formation appears to be a long row.

NGC 4548. One of the spiral arms contains well-defined rows bordered by a thin dust lane on the inside.

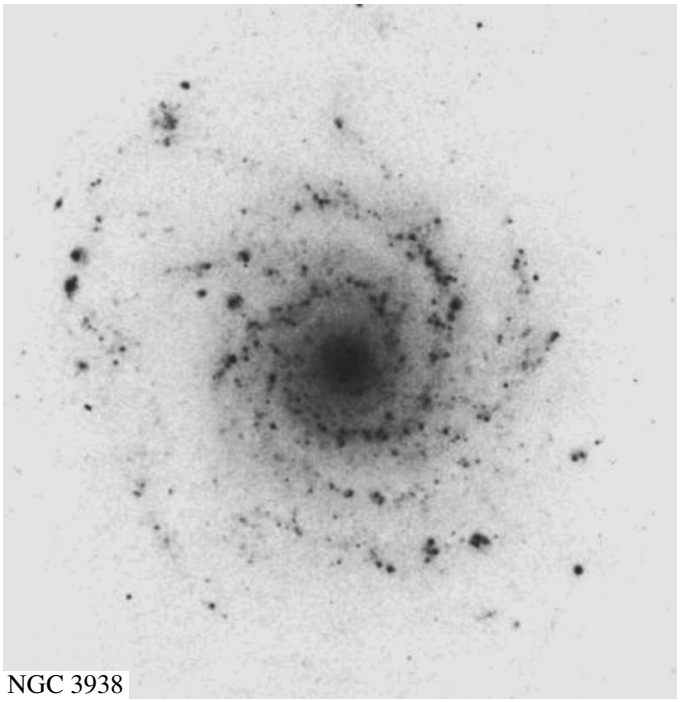

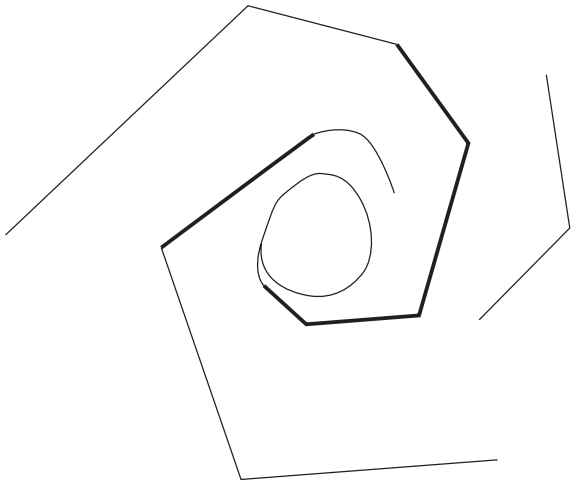

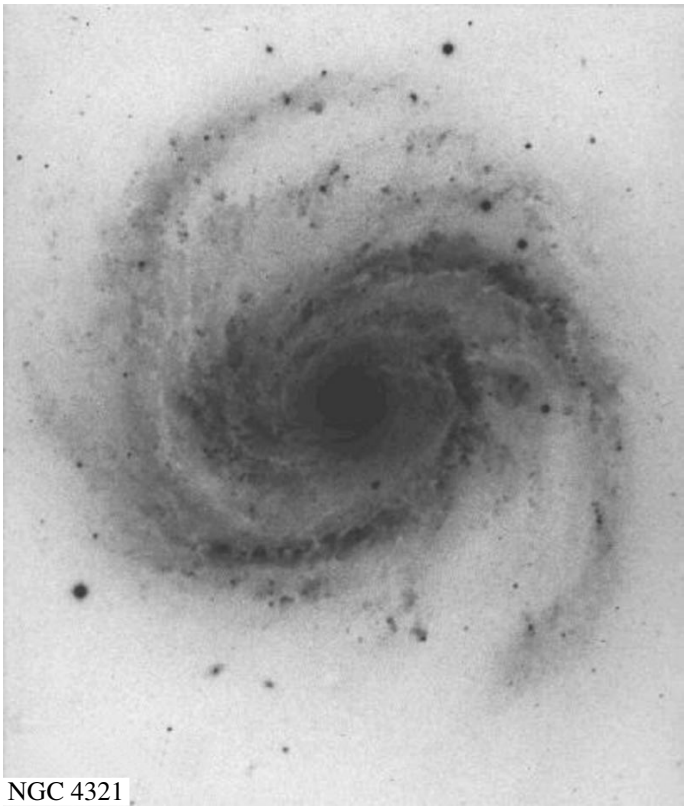

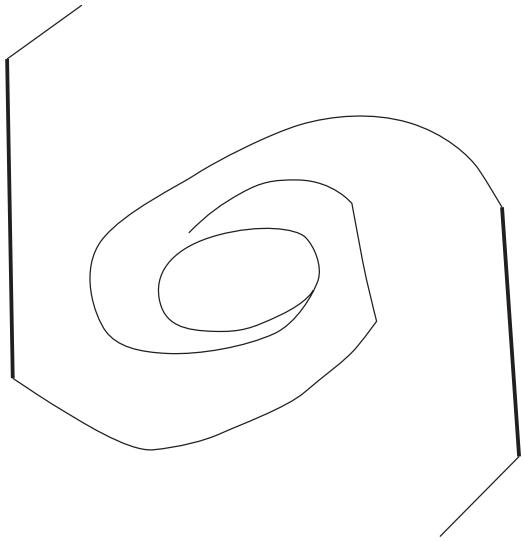

Fig. 2. (Contd.)

NGC 5161. The rows are strikingly straight. The longest one is very thin.

NGC 6946. The rows are rather blurred, especially in the galaxy's outer regions.

NGC 7137. The rows are extremely clear-cut and sharp.

The principal properties shared by the galaxies under consideration are their regular spiral patterns

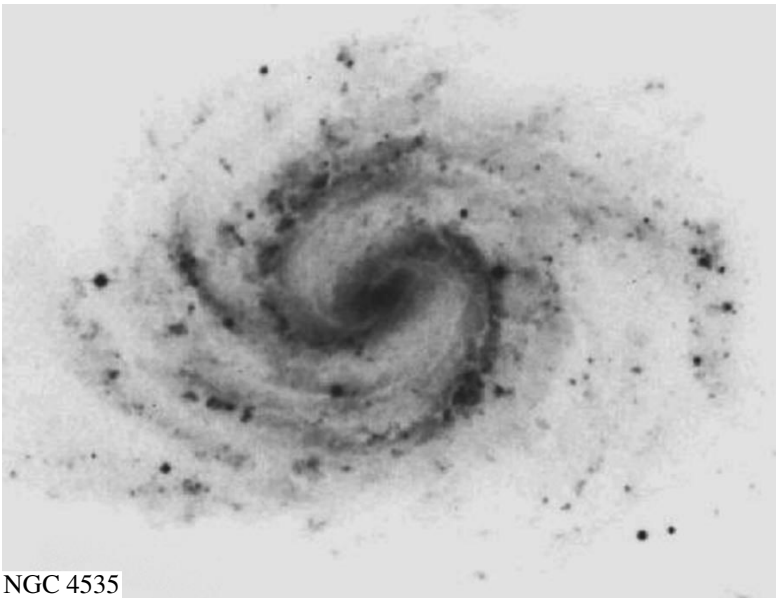

NGC 4535

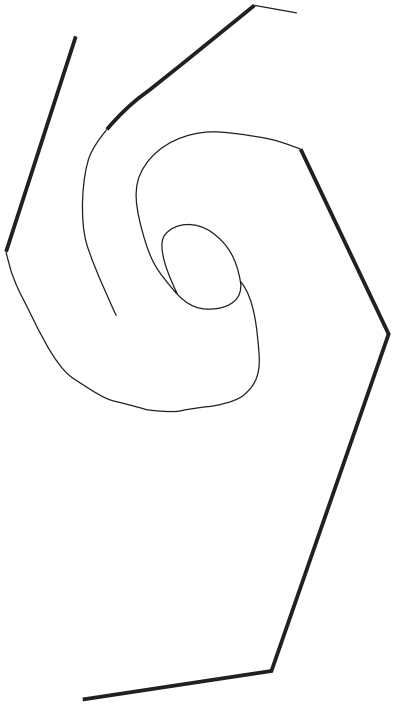

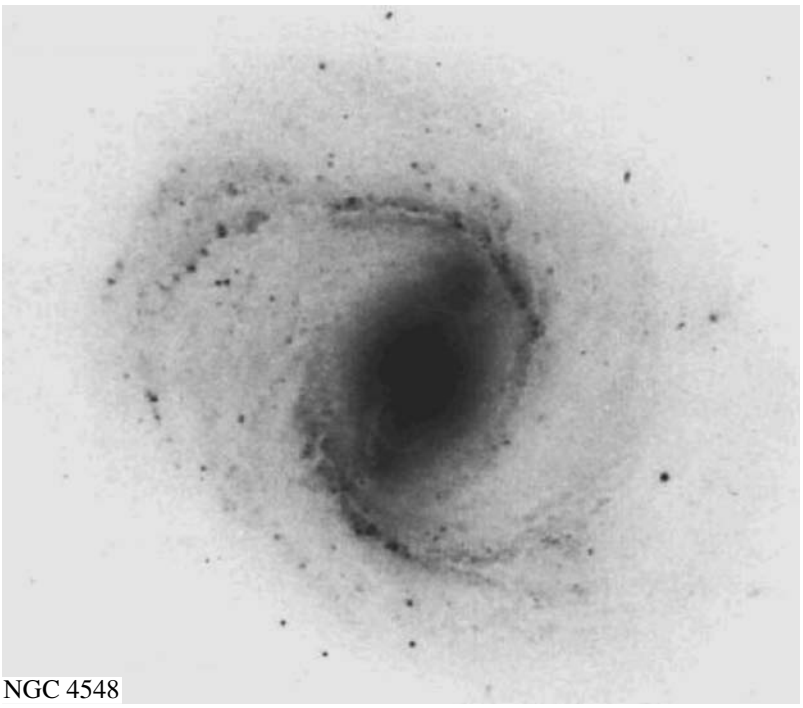

NGC 4548

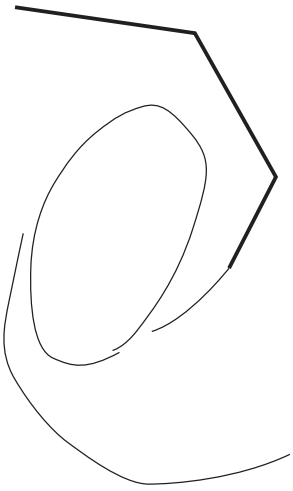

Fig. 2. (Contd.)

(types 9 and 12 in [15] correspond to Grand Design), late morphological types (Sbc–Sd), and relatively low luminosities (apart from NGC 4321, all galaxies have M_B fainter than -20^m). Our list includes both barred galaxies and galaxies without noticeable bars, suggesting that these nonaxisymmetric features are not involved in the formation of rows. The presence of close companions is not a necessary condition for the emergence of rows either: Table 1 contains both galaxies in pairs or groups and fairly isolated systems without any galaxies of comparative brightness within several diameters of them.

In most cases, the angle at which the row is seen from the galaxy center lies in the range 40°–60°. As in M 51 and M 101, the angles formed by adjacent rows are close to 120° (Fig. 3).

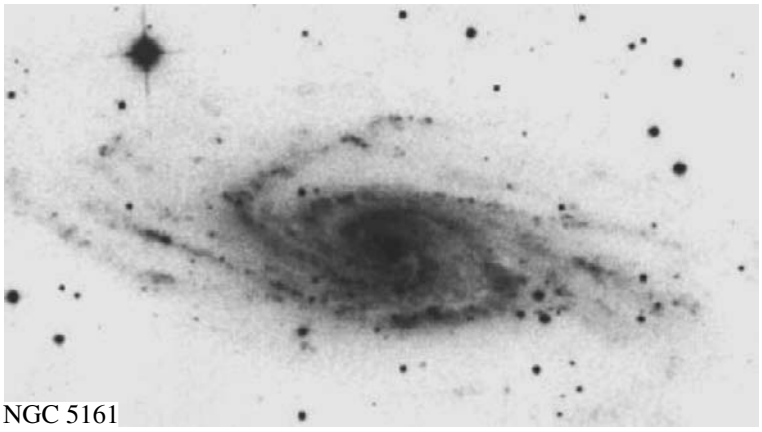

NGC 5161

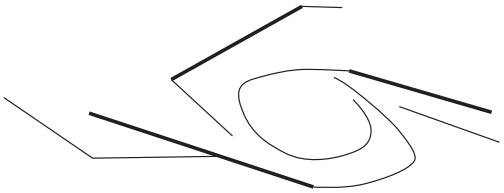

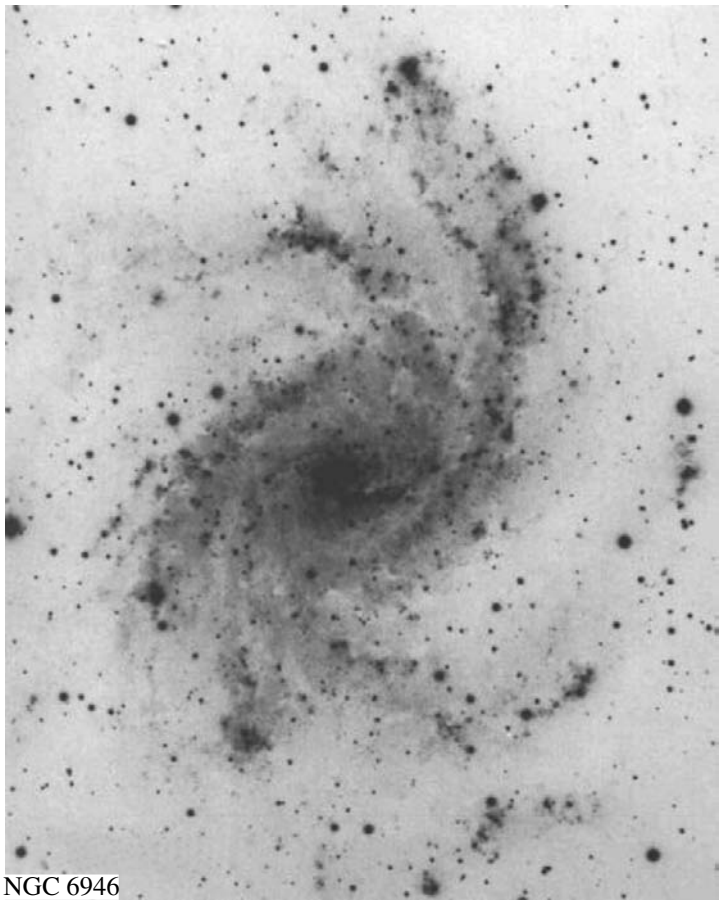

NGC 6946

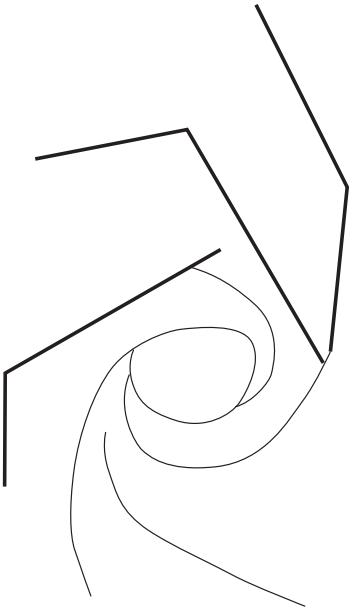

Fig. 2. (Contd.)

As in the case of nearby galaxies considered above, the sizes of rows clearly correlate with their galactocentric distances (Fig. 4). (In this paper, we determined the distance from the far end of each row corrected for projection effects.) This can be considered as independent evidence for the nonrandom nature of the identified features.

The rows and, in the case of multiple rows, the brightest ones observed in a number of galaxies lie on the periphery of the galaxy's regular spiral pattern (apparently near corotation if, following [16], the regular spiral arms are assumed to stretch to the corotation radius).

4. DISCUSSION AND CONCLUSIONS

The linear segments—rows in the spiral arms of galaxies are not artifacts, a freak of the imagination, or

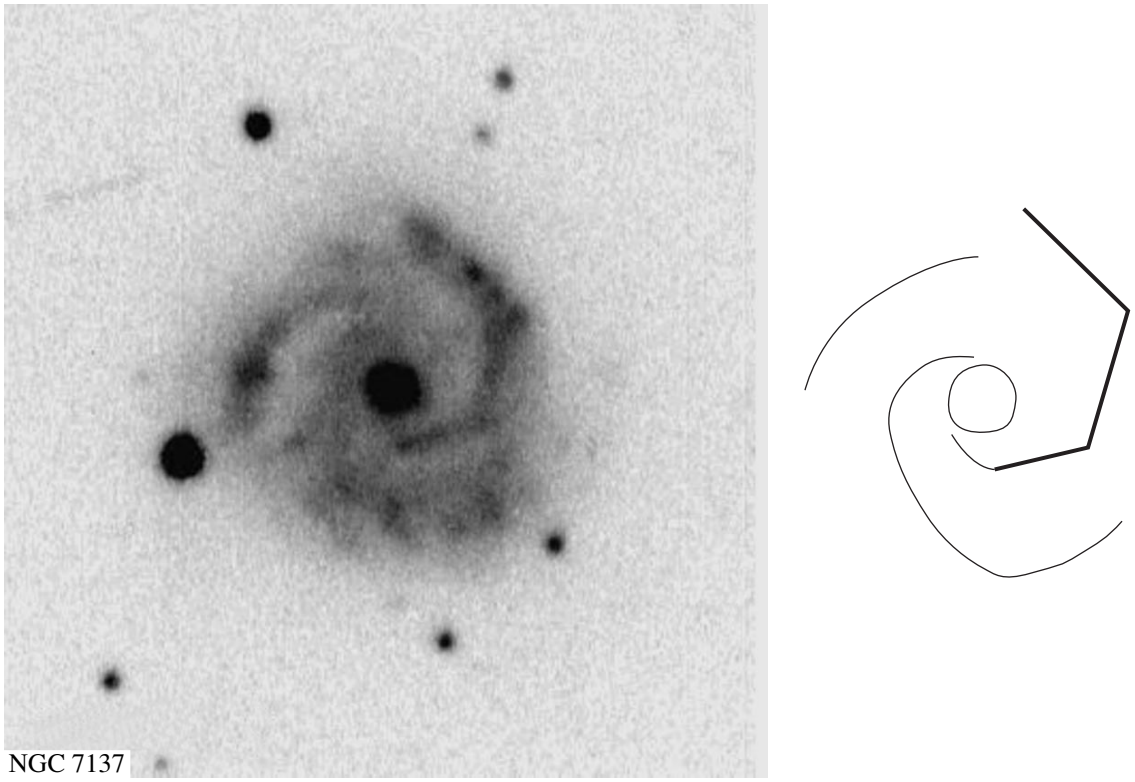

Fig. 2. (Contd.)

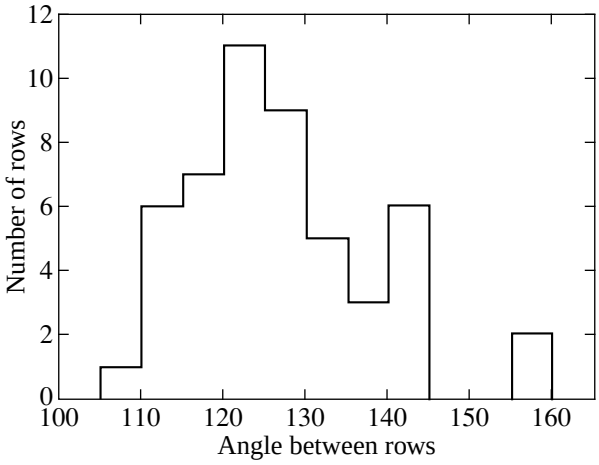

Fig. 3. Histogram of angles between adjacent rows.

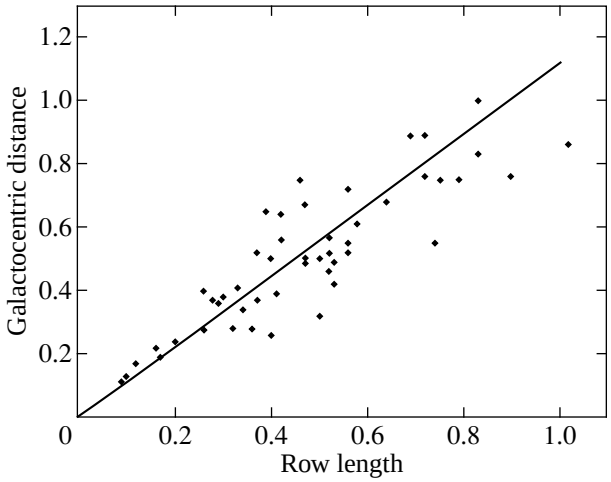

Fig. 4. Row size versus galactocentric distance.

optical illusions. They actually exist in the spirals considered above and in many other galaxies. Galaxies with rows are not distinguished by their global characteristics. As was shown above, they are in most cases normal low-luminosity galaxies with regular spiral patterns. The total star-formation rates in these galaxies are also relatively low, as suggested by the absence of objects with small color indices among them (see Table 1). By their M_{HI}/L ratios, the galaxies under consideration are not distinguished among Sb–Sc galaxies with M_{HI}/L = 0.1–0.3 [17]. The radial H I surface density distributions are available for some of them. The azimuthally averaged gas density in the regions of bright rows is typical of spiral galaxies (Table 2). According to published data, the gas rotation velocities are also rather low in the galaxies (see Table 2, which gives the maxi-

mum gas rotation velocity V_{row} in the row region and the maximum gas rotation velocity in the galaxy V_{max}) and agree well with their total luminosities.

A detailed comparison of galaxies with and without rows requires a considerably larger amount of statistical data and is not given here. However, considering that the galaxies under study exhibit the most conspicuous rows and are, therefore, only "the tip of the iceberg," there is reason to believe that the rows do not constitute a rare exception, at least for regular late-type spirals (Grand Design Sbc–Sc).

The rows are elements of the global spiral pattern with a large-scale density wave standing behind. Undoubtedly, the rows are also of a wave nature: differential rotation of the disk would destroy any "material" linear feature with a length comparable to the radius in a time of the order of one or two rotations (10^8 years).

The observed rows can be somewhat arbitrarily divided into two types. The first type represents straightened and, as a rule (but not always), brighter spiral-arm segments with widths approximately equal to (or larger than) those of the normal, smoothly bending arms of galaxies. They fit well into the overall spiral pattern. These rows are mostly multiple and join at angles close to $2\pi/3$. M 51, M 101, NGC 2223, and NGC 7137 are typical examples. The second type of row represents (occasionally very narrow) linear bright features, isolated or coexisting with the more blurred spirals in the same galaxy region and, in some cases, even crossing these features. NGC 1232, NGC 2942, NGC 3631, NGC 4548, and NGC 5161 can serve as examples. Some galaxies contain spatially separated rows of both types (such as NGC 1232). Despite the apparent isolation, the rows of the second type either lie entirely inside the spiral arms or branch off from them, i.e., always remain connected with the spiral pattern. These features are seen especially clearly in Hα or in the ultraviolet. As a result, the spiral pattern in M 51, which contains both straightened arm segments and narrow rows inside them, is better seen in the emission line than in the *B* band.

Since narrow rows can consist of only very young and short-lived features, it would be natural to assume that they evolve into rows of the first type or continuously replenish them with recently formed stars. The initial stage of row formation can apparently be thin and bright chains of star-forming regions, such as those observed in NGC 1232, NGC 5161, or NGC 7137.

It may be assumed that the star-forming regions in different parts of the same row must arise independently; otherwise, the linearity of the configuration could not be preserved: the time of propagation of acoustic or Alfvén perturbations to a distance of 10 kpc in a gas environment is about one billion years! The row formation mechanism must therefore be associated with a large-scale process: the emergence of a straight front of gas compression that stimulates simultaneous star formation along the entire row length.

Table 2. Gas surface density and maximum rotation velocity in the row regions

NGC	σ_{HI}, 10^{20} cm^{-2}	V_{row}, km s^{-1}	V_{max}, km s^{-1}	Reference
3631	6	130	150	[21]
3938	7	–	–	[22]
4303	10	130	162	[23]
4321	8	250	251	[23]
4535	7	130	186	[23]
4548	1.5	110	166	[23]
6946	9	155	204	[24]

This kind of a mechanism can be associated both with the nature of a spiral density wave and with the peculiar behavior of the compression shock wave in the gas flowing through the gravitational potential relief of the density wave. Although the overall picture of row formation is not yet completely understood, one might expect [11] the hydrodynamic stability of plane shock fronts against the warping of the surfaces of linear spiral-arm segments to be responsible for their emergence. The surface of a weakly curved front is known to tend to straighten out to become flat [18, 19]. In the presence of a sufficiently dense gas, the compression wave synchronizes star formation in flat layers; as a result, the latter may appear as linear segments in the spiral pattern.

As simple gas-dynamical considerations show [20], one might expect the size of the flattening segment of the spiral front to be comparable to the local radius of curvature of the spiral. In this case, the rows must subtend a central angle of ~60°, while the angle between adjacent rows must be close to $2\pi/3$, in agreement with observations. Since the radius of curvature of the spiral increases with distance to the center, the size of the segment, being comparable to the radius of curvature, must also increase linearly with galactocentric distance, as corroborated by observations.

We can thus offer a general explanation for the principal geometric properties of the observed rows. In the future, we plan to quantitatively test our approach by numerical simulations.

ACKNOWLEDGMENTS

We are grateful to Yu.N. Efremov and G. Byrd for useful discussions. This study was supported by the Program "Universities of Russia," the Federal Program "Astronomy" (project no. 1.2.4), and the Russian Foundation for Basic Research (project no. 98-02-17102).

REFERENCES

1. B. A. Vorontsov-Velyaminov, Astron. Zh. **28**, 43 (1951).
2. B. A. Vorontsov-Velyaminov, *Atlas and Catalog of Interacting Galaxies* (Moscow Univ., Moscow, 1959), Part 1.
3. B. A. Vorontsov-Velyaminov, Astron. Zh. **41**, 814 (1964).

4. A. Sandage and J. Bedke, *Atlas of Galaxies Useful for Measuring the Cosmological Distance Scale* (Space Telescope Science Inst., Baltimore, Md, 1988).
5. B. A. Vorontsov-Velyaminov, *Extragalactic Astronomy* (Nauka, Moscow, 1978).
6. W. H. Waller, R. C. Bohlin, R. H. Cornett, *et al.*, Astrophys. J. **481**, 169 (1997).
7. H. C. Arp, IEEE Trans. Plasma Sci. **PS-14**, 748 (1986).
8. Yu. N. Efremov, *Star Formation Regions in Galaxies: Star Complexes and Spiral Arms* (Nauka, Moscow, 1989).
9. R. J. Allen and W. M. Goss, Astron. Astrophys., Suppl. Ser. **36**, 135 (1979).
10. J. H. Knapen, J. E. Beckman, J. Cepa, and N. Nakai, Astron. J. **308**, 27 (1996).
11. A. D. Chernin, Astrofizika **41**, 609 (1998).
12. D. S. Mathewson, P. C. van der Kruit, and W. N. Brouw, Astron. Astrophys. **17**, 468 (1972).
13. L. Bottinelli, L. Gouguenheim, G. Paturel, and G. de Vaucouleurs, Astron. Astrophys., Suppl. Ser. **56**, 381 (1984).
14. G. de Vaucouleurs, A. de Vaucouleurs, H. Corwin, *et al.*, *Third Reference Catalogue of Bright Galaxies* (Springer, New York, 1991).
15. B. G. Elmegreen and D. M. Elmegreen, Astrophys. J. **314**, 3 (1987).
16. B. G. Elmegreen and D. M. Elmegreen, Astrophys. J. **445**, 591 (1995).
17. J. S. Young and P. M. Knezek, Astrophys. J. Lett. **347**, L55 (1989).
18. S. P. Dyakov, Zh. Éksp. Teor. Fiz. **27**, 288 (1954).
19. V. M. Kontorovich, Zh. Éksp. Teor. Fiz. **33**, 1527 (1957).
20. A. D. Chernin, Mon. Not. R. Astron. Soc. **308**, 321 (1999).
21. J. H. Knapen, Mon. Not. R. Astron. Soc. **286**, 403 (1997).
22. P. C. van der Kruit and G. S. Shostak, Astron. Astrophys. **105**, 351 (1982).
23. V. Cayatte, C. Kotanyi, and C. Balkowski, Astron. J. **107**, 1003 (1994).
24. K. J. Gordon, N. H. Remage, and M. S. Roberts, Astrophys. J. **154**, 845 (1968).

Translated by A. Dambis

Astronomy Letters, Vol. 26, No. 5, 2000, pp. 297–308. Translated from Pis'ma v Astronomicheskiĭ Zhurnal, Vol. 26, No. 5, 2000, pp. 355–368.

A Catalog of X-ray Sources as Observed by the TTM/COMIS Telescope Onboard the Mir–Kvant Observatory in 1988–1998

A. N. Emelyanov[1]*, N. L. Aleksandrovich[1], and R. A. Sunyaev[1, 2]

[1] *Space Research Institute, Russian Academy of Sciences, Profsoyuznaya ul. 84/32, Moscow, 117810 Russia*
[2] *Max-Planck-Institut fuer Astrophysik, Karl Schwarzschild Strasse 1, 86740 Garching bei Muenchen, Germany*

Received May 11, 1999; in final form, October 19, 1999

Abstract—A catalog of X-ray sources as observed by the TTM/COMIS telescope onboard the Mir–Kvant observatory is presented. Brief information about the 67 sources detected at a confidence level higher than 4σ between 1988 and 1998 is provided. X-ray properties and characteristic spectra of different types of sources are briefly described. © *2000 MAIK "Nauka/Interperiodica".*

Key words: *catalog, Mir–Kvant, Roentgen, TTM, X-ray novae, transients, bursters, black-hole candidates*

INTRODUCTION

This catalog aims at systematizing the data accumulated over ten years of operation of the TTM/Roentgen telescope onboard the Mir orbiting station. Since TTM observations of X-ray sources began well before the launch of X-ray observatories, such as ASCA (1993), RXTE (1994), and BeppoSAX (1996), they provide unique data for 1988–1993 on a number of objects, which later were intensively studied by these observatories. We give complete information about all the sources included in the catalog by sessions: the total number of sessions, their total exposure time, the total time of object "visibility" with TTM, and the relative time of source stay in "active" state (if observed). The catalog also provides the number of sessions of HEXE, which, given its harder operating range (see below for brief data on this instrument), yield more complete information about the source spectra.

The catalog contains data on the 67 sources known to date (see Table 1), 18 of which are transients (the designation U-S stands for "ultrasoft"), 13 are pulsars, 18 are bursters, and 17 are black-hole candidates (BHC), two microquasars (MQ) with an apparent superluminal component separation velocity—GRS 1915+105 [1] and GRO J1655–40, a supernova remnant (SNR)—the Crab nebula, two galaxies—NGC 4151 and Cen A, and six X-ray novae (XN) (see, e.g., [2, 3]). Fifteen objects can be classified as high-mass X-ray binaries (HMXRB), and another 46 can be classified as low-mass X-ray binaries (LMXRB). Of the 67 objects in the catalog, only six (SMC X-1, LMC X-1, LMC X-2, LMC X-4, NGC 4151, and Cen A) do not belong to our Galaxy (EXTR). We also briefly analyze the spectra for typical representatives of each of the classes.

INSTRUMENTS AND OBSERVATIONS

The Kvant module with onboard astrophysical instruments was docked with the Mir space station in 1987 and is still in operation. It includes four instruments sensitive to high-energy photons: TTM/COMIS, HEXE, GSPC, and Pulsar X-1. One of these instruments is a coded-mask camera called COMIS (COded-Mask Imaging Spectrometer) or TTM.

The TTM X-ray telescope is a wide-field camera that uses a coded mask as the entrance aperture to determine the positions of sources. The instrument operates in the 2–30-keV energy band with a $15° \times 15°$ total field of view. The detector geometrical area is 655 cm^2. The angular resolution can reach 2 arcmin, the temporal resolution is 1 s [4], and the energy resolution is 18–20% at 6 keV.

HEXE (High-Energy X-ray Experiment) is an X-ray spectrometer that consists of four identical phoswich detectors sensitive to X-ray emission in the range 15 to 200 keV. The field of view of each detector is $1.^\circ 6 \times 1.^\circ 6$ (full width at half maximum) and is bounded by a swinging collimator, which turns every two minutes to measure X-ray background. The geometrical area of each detector is 200 cm^2. The maximum time resolution is 0.3–25 ms. More details on the HEXE design and performance can be found in [5].

* E-mail address for contacts: emelyanov@hea.iki.rssi.ru

1063-7737/00/2605-0297$20.00 © 2000 MAIK "Nauka/Interperiodica"

Table 1. The catalog of X-ray sources as observed by the TTM/COMIS telescope

Source	R.A.(2000)	Decl.(2000)	Date of peak flux	Peak flux, mCrab	T_{tot}, h	T_{obs}, h	T_{100}, h	T_{obs}/T_{tot}	T_{100}/T_{tot}	HEXE (session)	Comments*
SMC X-1	01:17:03.6	–73:26.2	Jan. 11, 1989	45.9 ± 4.3	3.95(19)	2.99(14)	0(0)	0.7570	0.0000	14	EXTR, HMXRB PULSAR
4U 0115+63	01:18:34.0	+63:43.8	May 28, 1994	37.6 ± 3.2	0.96(3)	0.96(3)	0(0)	1.0000	0.0000	3	HMXRB PULSAR TRANSIENT
GRO J0422+32	04:21:46.8	+32:55.0	Sept. 16, 1992	495.9 ± 6.7	5.90(27)	2.39(9)	2.39(9)	0.4051	0.4051	9	LMXRB BHC XN U-S TRANSIENT
LMC X-2	05:20:34.5	–71:56.2	June 13, 1989	17.6 ± 4.4	18.14(94)	0.54(2)	0(0)	0.0298	0.0000	0	EXTR, LMXRB
LMC X-4	05:32:54.1	–66:21.0	Jan. 05, 1989	31.1 ± 5.6	18.14(94)	4.92(23)	0(0)	0.2711	0.0000	3	EXTR, HMXRB PULSAR
Crab nebula	05:34:30.5	+21:66.0	Apr. 14, 1989	1238 ± 47	5.83(27)	5.65(26)	5.65(26)	0.9685	0.9685	7	SNR
A0535+26	05:38:54.5	+26:18.6	Feb. 19, 1994	2182 ± 32	5.83(27)	3.31(17)	3.31(17)	0.5673	0.5673	17	HMXRB PULSAR
LMC X-1	05:39:43.4	–69:43.5	Jan. 04, 1989	20.9 ± 4.3	18.14(94)	1.30(7)	0(0)	0.0718	0.0000	4	EXTR, HMXRB BH
GRS 0834–430	08:35:56.0	–43:10.5	Nov. 01, 1992	126.6 ± 4.2	24.36(88)	4.78(16)	0.32(1)	0.1963	0.0130	15	HMXRB TRANSIENT PULSAR
Vela X-1	09:02:06.6	–40:32.9	Nov. 24, 1992	663 ± 13	24.04(87)	17.52(64)	8.78(34)	0.7285	0.3651	33	HMXRB PULSAR
GRS 1009–45	10:13:35.6	–45:04.9	Sept. 30, 1993	531.1 ± 9.8	5.42(24)	5.42(24)	5.42(24)	1.0000	1.0000	22	LMXRB BHC XN U-S TRANSIEN
Cen X-3	11:21:16.3	–60:36.4	Jan. 09, 1993	324 ± 39	11.41(48)	9.96(42)	6.51(27)	0.8734	0.5705	32	HMXRB PULSAR
NGC 4151	12:10:31.5	+39:23.3	Dec. 20, 1991	154 ± 30	3.16(13)	0.29(2)	0.13(1)	0.0919	0.0414	0	EXTR, SEYFERT GALAXY TYPE 1
GX 301-2	12:26:36.8	–62:45.6	June 04, 1994	558 ± 32	12.20(51)	11.30(47)	4.11(19)	0.9265	0.3372	41	HMXRB PULSAR
4U 1254–690	12:57:36.1	–69:17.2	Jan. 09, 1993	59.8 ± 11.1	9.46(39)	1.04(4)	0(0)	0.1103	0.0000	0	LMXRB BURSTER
Cen A	13:25:17.9	–43:00.6	Jan. 02, 1993	24.9 ± 2.5	1.20(4)	1.02(3)	0(0)	0.8527	0.0000	3	EXTR, AGN GALAXY
Cir X-1	15:20:41.3	–57:09.8	Oct. 10, 1993	1681 ± 21	9.53(43)	9.53(43)	7.85(37)	1.0000	0.8236	42	LMXRB BURSTER
4U 1543–624	15:47:54.5	–62:33.2	Jan. 30, 1989	65.2 ± 10.9	11.84(52)	0.87(4)	0(0)	0.0738	0.0000	0	LMXRB
4U 1608–522	16:12:41.7	–52:25.7	Mar. 25, 1989	154 ± 37	1.55(6)	0.29(1)	0.29(1)	0.1866	0.1866	0	LMXRB BURSTER
Sco X-1	16:19:54.5	–15:38.2	July 18, 1998	2443 ± 61	0.20(1)	0.20(1)	0.20(1)	1.0000	1.0000	0	LMXRB QPO FLARES
3U 1626–67	16:32:15.9	–67:27.4	Oct. 29, 1989	57.1 ± 7.9	3.32(13)	3.07(12)	0(0)	0.9254	0.0000	8	LMXRB PULSAR
4U 1630–47	16:33:57.9	–47:23.2	Mar. 25, 1989	259.8 ± 19.5	3.54(18)	1.44(5)	1.44(5)	0.4075	0.4075	0	LMXRB BHC U-S TRANSIENT
4U 1636–536	16:40:52.0	–53:44.8	Mar. 13, 1994	114.9 ± 19.7	1.85(7)	1.85(7)	1.14(4)	1.0000	0.6173	0	LMXRB BURSTER
GX 340+0	16:45:45.1	–45:36.4	Oct. 11, 1994	701 ± 165	6.61(28)	6.35(26)	6.35(26)	0.9608	0.9608	0	LMXRB QPO
GRO J1655–40	16:53:60.0	–39:50.9	Sept. 30, 1994	710 ± 17	5.73(25)	4.49(15)	4.49(15)	0.7841	0.7841	10	LMXRB BHC MQ U-S TRANSIENT
Her X-1	16:57:50.0	+35:20.5	July 25, 1994	126.9 ± 3.2	18.89(65)	2.17(7)	0.33(1)	0.1151	0.0177	5	LMXRB PULSAR ECLIPSING
GX 339–4	17:02:50.3	–48:46.3	Mar. 13, 1994	340.1 ± 8.9	3.07(12)	2.11(8)	2.11(8)	0.6883	0.6883	7	LMXRB BHC
4U 1700–37	17:03:56.9	–37:50	Oct. 01, 1994	285 ± 22	6.59(28)	3.34(11)	2.18(7)	0.5066	0.3312	3	HMXRB PULSAR
GX 349+2	17:05:42.5	–36:26.0	Sept. 29, 1994	1398 ± 27	8.03(35)	6.92(28)	6.92(28)	0.8613	0.8613	3	LMXRB QPO
4U 1705–44	17:08:54.6	–44:05.8	Mar. 24, 1989	418.5 ± 22.8	8.05(34)	4.57(16)	3.53(13)	0.5681	0.4385	0	LMXRB BURSTER
KS J1716–389	17:15:58.4	–38:52.3	Oct. 08, 1994	83.3 ± 18.2	9.88(40)	0.26(1)	0(0)	0.0261	0.0000	0	LMXRB
GRS 1716–249	17:19:37.3	–25:01.0	Oct. 07, 1993	515.1 ± 13.6	24.61(104)	2.62(9)	2.06(7)	0.1064	0.0838	4	LMXRB BHC XN U-S TRANSIENT
Terzan-2	17:27:33.1	–30:48.5	Oct. 24, 1992	65.5 ± 15.9	27.05(115)	0.87(3)	0(0)	0.0323	0.0000	1	LMXRB BURSTER CLUSTER

Table 1. (Contd.)

Source	R.A.(2000)	Decl.(2000)	Date of peak flux	Peak flux, mCrab	T_{tot}, h	T_{obs}, h	T_{100}, h	T_{obs}/T_{tot}	T_{100}/T_{tot}	HEXE (session)	Comments*
GX 9+9	17:31:43.9	–16:57.2	Sept. 04, 1989	562 ± 103	3.46(17)	2.53(11)	2.53(11)	0.7293	0.7293	0	LMXRB
GX 354+0	17:31:57.0	–33:49.2	Sept. 12, 1989	262.4 ± 11.9	25.16(107)	11.27(45)	8.81(35)	0.4479	0.3502	0	LMXRB BURSTER
GX 1+4	17:32:02.2	–24:45.1	Aug. 16, 1989	51.6 ± 10.8	24.63(106)	0.58(2)	0(0)	0.0234	0.0000	1	LMXRB PULSAR
MXB 1730–335	17:33:24.3	–33:23.1	May 09, 1994	97.4 ± 13.3	26.08(112)	0.66(2)	0(0)	0.0255	0.0000	0	LMXRB BURSTER
KS 1730–312	17:33:32.9	–31:14.0	Sept. 27, 1994	591.1 ± 17.3	26.41(113)	1.17(4)	0.86(3)	0.0443	0.0324	0	XRB BHC XN U-S TRANSIENT
GRO J1735–27	17:34:07.3	–26:52.0	Oct. 20, 1992	129 ± 27	26.80(116)	0.58(2)	0.26(1)	0.0217	0.0098	0	LMXRB TRANSIENT
KS 1731–260	17:34:12.1	–26:05.0	Feb. 20, 1997	256 ± 46	26.63(115)	18.72(76)	12.59(53)	0.7028	0.4728	38	LMXRB BURSTER
X 1735–444	17:39:00.9	–44:27.7	Oct. 01, 1994	403 ± 91	5.55(20)	2.66(9)	2.37(8)	0.4791	0.4270	0	LMXRB BURSTER
GRS 1739–278	17:42:40.7	–27:45.4	Mar. 01, 1996	552 ± 34	26.80(116)	1.78(8)	1.78(8)	0.0663	0.0663	8	LMXRB BHC XN HARD TRANSIENT
1E1740.7–2942	17:43:53.7	–29:44.3	Mar. 21, 1989	59.3 ± 13.5	26.80(116)	0.83(3)	0(0)	0.0311	0.0000	1	LMXRB BHC
GRO J1744–28	17:44:34.2	–28:45.2	Feb. 04, 1996	1940 ± 29	26.80(116)	3.02(13)	3.02(13)	0.1126	0.1126	13	LMXRB QPO PULSAR BURSTS HARD TRANSIENT
H1741–322	17:45:39.6	–32:12.2	Feb. 04, 1996	97 ± 24	27.01(116)	0.23(1)	0(0)	0.0086	0.0000	0	LMXRB BHC U-S TRANSIENT
MXB 1743–293	17:45:47.0	–29:17.2	Sept. 12, 1989	415.3 ± 18.9	26.80(116)	0.42(3)	0.42(3)	0.0158	0.0158	0	LMXRB BURSTER
GX 3+1	17:47:56.0	–26:34.0	Sept. 04, 1989	625 ± 25	26.80(116)	25.71(109)	25.52(108)	0.9593	0.9523	0	LMXRB BURSTER
KS J1748–248	17:48:06.4	–24:45.0	May 12, 1994	113 ± 26	25.46(110)	1.46(5)	0.51(2)	0.0572	0.0201	0	TRANSIENT
A1744–36	17:48:13.4	–36:08.0	Aug. 22, 1989	82.7 ± 7.8	16.82(72)	2.41(9)	0(0)	0.1431	0.0000	0	LMXRB SOFT TRANSIENT
4U 1745–203	17:48:58.5	–20:24.9	Oct. 21, 1988	61.1 ± 13.9	15.05(62)	0.19(1)	0(0)	0.0126	0.0000	0	LMXRB GLOBULAR CLUSTER BURSTER
NGC 6441	17:50:13.0	–37:02.8	Aug. 22, 1989	42.8 ± 9.7	16.40(69)	1.91(6)	0(0)	0.1164	0.0000	2	LMXRB BURSTER
Sco X-6	17:58:40.4	–33:48.2	Aug. 16, 1989	339 ± 74	22.54(93)	9.53(38)	2.00(8)	0.4227	0.0886	2	LMXRB BHC TRANSIENT
GX 5-1	18:01:07.9	–25:04.0	Mar. 05, 1996	1548 ± 58	25.59(110)	25.59(110)	25.59(110)	1.0000	1.0000	5	LMXRB QPO
GX 9+1	18:01:31.7	–20:31.0	Aug. 21, 1989	1058 ± 150	9.15(36)	7.55(30)	7.55(30)	0.8251	0.8251	0	LMXRB BHC
GX 13+1	18:14:31.3	–17:09.0	Mar. 19, 1989	370 ± 25	1.36(8)	1.19(7)	1.19(7)	0.8746	0.8746	0	LMXRB BURSTER
GX 17+2	18:16:02.4	–14:01.9	Mar. 19, 1989	726 ± 57	1.19(7)	1.19(7)	1.19(7)	1.0000	1.0000	0	LMXRB BURSTER
NGC 6624	18:23:40.6	–30:21.4	Sept. 09, 1989	554 ± 25	4.83(23)	2.09(11)	2.09(11)	0.4330	0.4330	0	LMXRB BURSTER CLUSTER
4U 1822–37	18:25:49.0	–37:07.2	Sept. 10, 1989	52.8 ± 4.8	1.66(8)	0.53(4)	0(0)	0.3202	0.0000	2	LMXRB ECLIPSING
GRS 1915+105	19:15:11.5	+10:56.3	Nov. 13, 1995	1449 ± 17	2.65(9)	2.65(9)	2.65(9)	1.0000	1.0000	9	LMXRB BHC MQ SOFT TRANSIENT
4U 1943+36	19:45:13.4	+36:31.3	Sept. 04, 1992	53.1 ± 11.1	18.06(74)	0.25(1)	0(0)	0.0138	0.0000	0	
KS 1947+300	19:49:34.2	+30:12.6	June 08, 1989	118.6 ± 15.1	18.79(78)	0.97(3)	0.33(1)	0.0515	0.0175	0	HMXRB TRANSIENT
4U 1954+31	19:55:59.1	+32:05.0	Sept. 05, 1992	127.1 ± 12.7	23.71(94)	1.23(5)	0.22(1)	0.0517	0.0092	0	HMXRB
Cyg X-1	19:58:21.7	+35:12.2	July 21, 1994	990.3 ± 16.8	24.86(98)	24.12(95)	23.19(92)	0.9703	0.9328	34	HMXRB BHC SUPERGIANT
XTE J2012+381	20:12:30.7	+38:09.1	Aug. 09, 1998	80.1 ± 18.3	10.70(48)	1.01(4)	0(0)	0.0947	0.0000	0	LMXRB
4U 2028+42	20:20:35.8	+44:03.6	July 11, 1989	103.9 ± 24.9	10.32(35)	0.30(1)	0.30(1)	0.0290	0.0290	0	
GS 2023+338	20:24:03.4	+33:51.8	June 09, 1989	358.9 ± 8.2	25.20(99)	14.78(52)	9.84(35)	0.5865	0.3904	32	LMXRB BHC XN U-S TRANSIENT
Cyg X-3	20:32:21.1	+40:57.3	July 10, 1989	509.7 ± 14.9	16.24(59)	13.77(48)	11.51(40)	0.8478	0.7091	11	HMXRB BHC

Note: Designations: LMXRB for low-mass X-ray binaries, HMXRB for high-mass X-ray binaries, BHC for black-hole candidates, XN for X-ray novae, U-S for ultrasoft, SNR for supernova remnants, AGN for active galactic nuclei, EXTR for extragalactic sources, and ECLIPSING for eclipsing sources.

The height of the Mir orbit is ~400 km, its inclination is 52°, and the orbital period is 92 min. Since the charge-particle background is too strong at high latitudes and when the Brazilian anomaly is crossed, only the equatorial segment of the orbit is used for observations, and the accumulation time on a single turn does not exceed 26 min. The Mir orientation can be maintained over this period of time with an accuracy of the order of one arcminute. At each instant of time, only a 20°-wide band of the sky along the Mir orbital plane is accessible to observation—the solar-panel orientation imposes this restriction. Since the orbital plane precesses with a period of 2.5 months, in general, only regions around the north and south celestial poles are inaccessible for the Mir instruments.

After the star sensor broke down in March 1988, the pointing accuracy was determined and checked by using solely TTM data. In this case, the observing sessions can be divided into three groups:

(1) Sessions with two or more identified sources. The precise orientation of the TTM field of view was restored for them. It should be noted, however, that there are less than half of such sessions.

(2) Sessions with one central source. The orientation of the spectrometer field of view is not known for these data.

(3) Sessions with no identified sources, the so-called empty fields.

A statistical analysis of 154 sessions with various sources near the center of the TTM field of view [3] shows that the distribution of pointing errors is similar to a Gaussian distribution with a mean of 25′ and a standard deviation of 8′. Thus, only the coordinates of the center of the TTM field of view are known with $\pm 0\overset{\circ}{.}5$ accuracy for the last two groups of sessions (see [6]).

When reducing the data in sessions with the restored orientation of the field of view, we assumed a source to be visible and identified if there was an emission peak at a confidence level no lower than 4σ (here, σ is the ratio of flux to its error) within one mask pixel (i.e., ~1.8 arcmin) of its position according to the catalog.

As a result of our study at a 3σ confidence level, we detected 209 X-ray sources. However, the confidence of this detection for individual sessions is dubious. A data analysis revealed that, for a 3σ confidence limit, the probability of identifying a "peak–source" with background fluctuations (i.e., the probability of detecting an emission peak in the field of view because of background fluctuations, with the position of this peak coinciding with that of a known source) exceeding 3σ is ~14% for densely populated regions, such as the Galactic center, and ~1.4% for sparsely populated regions, such as, for example, the vicinities of the pulsar A0535+26 and the Crab Nebula. At the same time, the probability of the identification error for the same regions but with a 4σ confidence limit is a mere ~1 and 0.06%, respectively. The lower confidence limit was therefore raised, and the number of reliably detected sources for each observing session decreased sharply. The distribution of identified sources over the entire X-ray sky and in the Galactic-center region is shown in Figs. 1 and 2.

It should be particularly emphasized that the Roentgen observations do not cover the entire sky but are mostly grouped in the region of the Galactic plane and near bright sources and their clusters. This is clearly seen in Fig. 3, which shows a map of total TTM exposures. When constructing this map, we took the field of view in sessions with unknown orientation as a circle of 14° diameter. It is worth noting that, the larger the inclination of the parallel incoming beam of emission from a point source to the telescope optical axis, the larger its fraction falls not on the detector but on the side walls and is lost. The signal-to-noise ratio is therefore at a maximum near the center of the field of view and drops to zero at its edges; as a result, the usable field of view does not exceed $14^\circ \times 14^\circ$.

In sessions with nonrestored orientation, a source was assumed to fall within the TTM field of view if it lay within $7\overset{\circ}{.}0$ of the field center. For such sessions, the central source was assumed to be identified if there was an emission peak at a confidence level no less than 6σ near the center of the spectrometer field of view (normally fewer than 20 mask pixels). Occasionally, during observing sessions of a single source, its coordinates on the TTM detector changed from session to session fairly predictably (i.e., given the direction and velocity of the Mir drift during a series of observations, the direction of shift in the source coordinates on the TTM detector can be determined); in this case, the source can be identified with an intensity peak at a confidence level of 5σ or higher. Information about sources was gathered for individual sessions.

DESCRIPTION OF THE CATALOG

The catalog (see Table 1) was divided into 12 columns.

Column 1 gives source names. Most of the names were borrowed from the catalogs compiled from Uhuru, Ariel [7], and HEAO 1 [8] satellite data and from the EINSTEIN catalog [9]. Several sources were discovered by the TTM telescope itself and the Granat observatory (see, e.g., [2, 10]. Their names in the catalog begin with KS (Kvant Source) and GRS (Granat Source), respectively.

Columns 2 and 3 list equatorial coordinates of the sources (at epoch 2000) in hours, minutes, seconds (right ascension) and degrees, arcminutes (declination).

Columns 4 and 5 give dates of peak flux and recorded peak (2–30 keV) fluxes from the sources with a 1σ error (in mCrabs), respectively.

Column 6 contains information about the total exposure time (in hours), when the source was within the

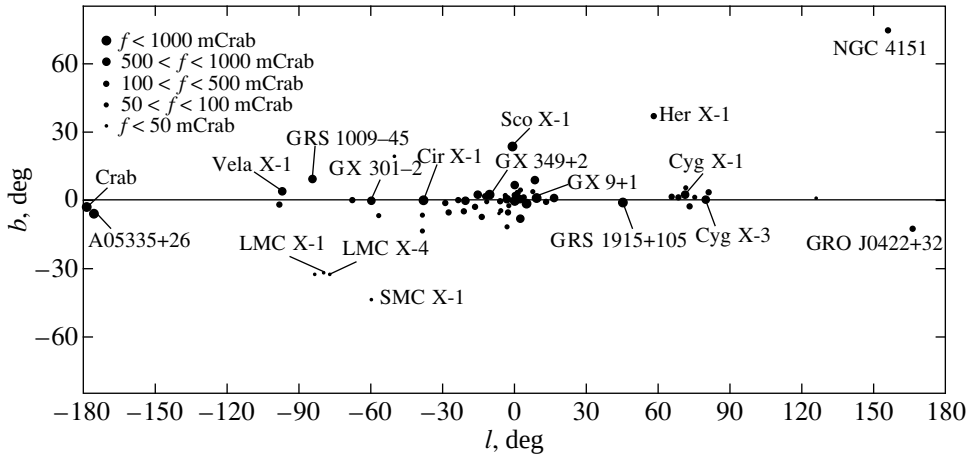

Fig. 1. The sky distribution of bright X-ray sources as constructed from TTM/COMIS data. The map is in rectangular Galactic coordinates; the circle sizes correspond to peak fluxes f from the sources.

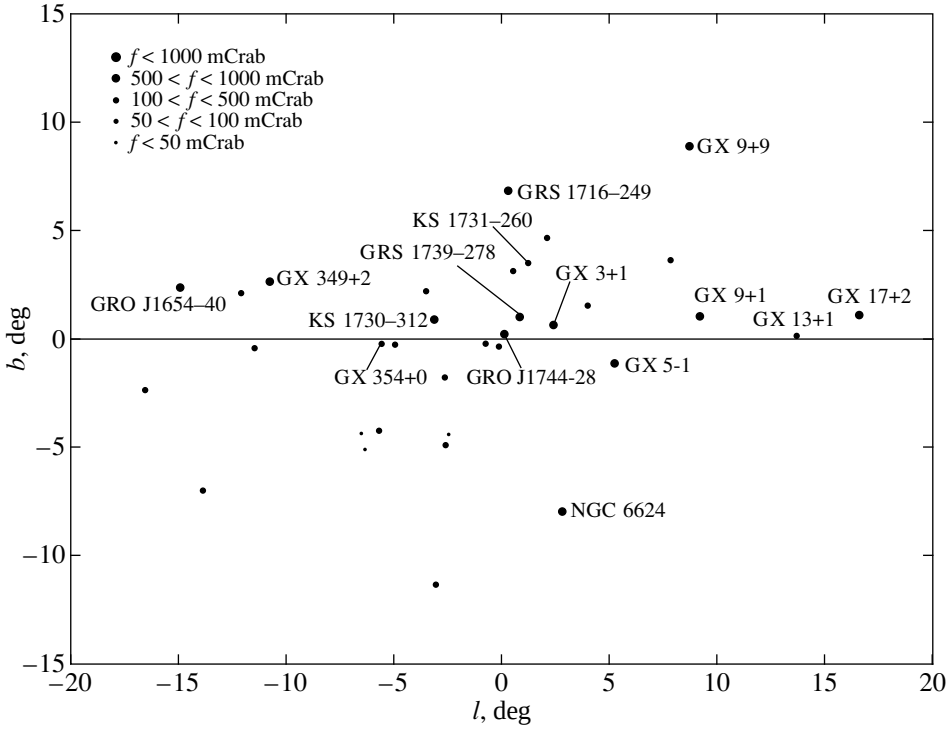

Fig. 2. The distribution of bright X-ray sources in the Galactic-center region. The map is in rectangular Galactic coordinates; the notation is the same as in Fig. 1.

TTM field of view, and column 7 gives the time (also in hours) during which the source was identified.

Column 8 gives the number of hours when the flux from the source was higher than 100 mCrab (2–30-keV band). In such sessions, information about the source spectrum can be obtained for individual sessions.

The numbers given in columns 6, 7, and 8 in parentheses contain the same information but expressed in terms of the number of sessions.

Column 9 indicates the ratio of the time during which the source was visible to the total time during which it was within the TTM field of view.

Column 10 indicates the ratio of the time during which the flux from the source was higher than 100 mCrab to the total exposure time.

Column 11 gives the number of sessions for each source during which it was identified by TTM, with the HEXE efficiency being nonzero.

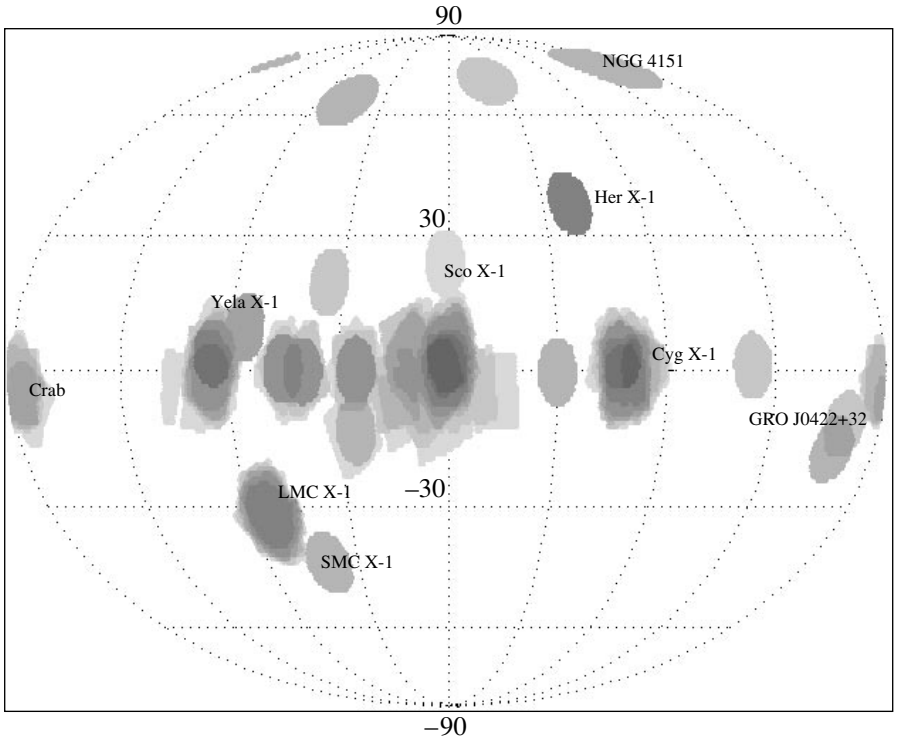

Fig. 3. The TTM exposure map for the entire sky from 1988 until 1998. The shades of gray denote exposures from less than one hour (light gray) to 42 hours (black).

Column 12 contains comments regarding the presumed nature of the source and its type.

CLASSIFICATION OF THE SOURCES

The catalog presents several classes of X-ray sources (see above). As can be seen from Table 2, some sources simultaneously belong to several classes. For example, GRO J1744–28 combines the properties of a pulsar, a burster, and a transient simultaneously. The subclass of X-ray novae in the class of transient sources may seem somewhat incomplete, because all X-ray transients are occasionally meant by this term. However, for each such group, we give a brief description, i.e., explain precisely which type of sources belongs to a given class to avoid a wrong interpretation of our classification, and provide energy spectra for one or more representatives of each designated class.

Transient sources. These are variable X-ray sources whose fluxes during outbursts can exceed their quiescent fluxes by several orders of magnitude. The outburst time scale ranges from several days to several months, while the interval between outbursts can be several years or decades. The sources of this type can be divided into two more subclasses: black-hole candidates (for example, 4U 1630-47, GRS 1915+105, or GRO J0422+32) and neutron stars (for example, 4U 0115+63 or A0535+26). Naturally, representatives of these subclasses have markedly different spectra. The class of transients is represented in our catalog by 18 sources. Three of them belong to the class of high-mass binary systems, 14 are low-mass binaries, and the system parameters for two sources are uncertain. They are all located within the Galaxy and lie in its plane. As was already said above, there are widely differing transient sources; therefore, we do not provide here any particular source. Examples of transients are considered in other classes (subclasses).

The subclass of X-ray novae. These are flaring X-ray sources from which no detectable emission is recorded most of the time. However, the flux during outbursts reaches a maximum in a few days, and the source becomes one of the brightest in the X-ray band. Subsequently, the flux begins to fall off exponentially with a time scale of 25–40 days. The X-ray novae form a subclass of transient sources. The catalog contains six such sources. Remarkably, all sources of this subclass (see Table 2) are black-hole candidates, and, as studies show, belong to low-mass binaries. Many objects of this subclass exhibit an intense soft spectral component with a characteristic temperature of ~1 keV under the assumption of a blackbody spectrum. This allowed Wait and Marshall [11] to separate them into a subclass of soft X-ray novae. Before the outburst of GS 2023+338 (and, subsequently, also GRO J0422+32 and GRS 1716–249), the presence of an intense soft component was assumed to be evidence typical of all X-ray novae [11]. It turned out that there are X-ray

Table 2. The classes of sources

Transients	Pulsars	Bursters	X-ray novae	Black-hole candidates	Extragalactic sources
GRO J0422+32	SMC X-1	4U 1254–690	GRO J0422+32	GRO J0422+32	SMC X-1
GRS 1009–45	4U 0115+63	Cir X-1	GRS 1009–45	LMC X-1	LMC X-2
4U 1630–47	LMC X-4	4U 1608–522	GRS 1716–249	GRS 1009–45	LMC X-4
GRO J1654–40	A0535+26	4U 1636–536	GRS 1739–278	4U 1630–47	LMC X-1
GRS 1716–249	GRS 0834–430	4U 1705–44	KS 1730–312	GRO J1654–40	NGC 4151
KS 1730–312	Vela X-1	Terzan-2	GS 2023+338	GX 339–4	Cen A
A0535+26	Cen X-3	GX 354+0		GRS 1716–249	
GRS 1739–278	GX 301–2	MXB 1730–335		KS 1730–312	
GRO J1744–28	3U 1626–67	NGC 6624		GRS 1739–278	
H1741–322	Her X-1	KS 1731–260		1E 1740.7–2942	
KS J1748–248	4U 1700–37	X1735–444		GS 2023+338	
A1744–36	GX 1+4	MXB 1743–293		Sco X-6	
Sco X-6	GRO J1744–28	GX 3+1		Cyg X-3	
GRS 1915+105		4U 1745–203		GRS 1915+105	
KS 1947+300		NGC 6441		Cyg X-1	
GS 2023+338		GX 13+1			
GRO J1735–27		GX 17+2			
4U 0115+63		GRO J1744–28			

novae with an abnormally hard spectrum without a soft component similar to the spectrum of Cygnus X-1 in its normal hard state. Possible reasons for the existence of such novae were discussed by Grebenev *et al.* [12]. Let us consider the soft X-ray nova GRS 1009–45 in Vela as an example of a representatives of this class.

GRS 1009–45 was discovered by the WATCH instrument onboard the Granat satellite on September 12, 1993 [13]. The source intensity rapidly increased to 0.5 Crab in the TTM standard X-ray band. The observations from September through November revealed an intense soft component and a variable hard component in the source spectrum. However, the hard component makes a much smaller contribution to the luminosity than the soft one. The spectrum obtained during the observations can be described by a blackbody (2–10 keV) and power-law (10–100 keV) approximation (see [3] for more detail). The source luminosity, as inferred from TTM data, was $1.5 \times 10^{36} \times d^2$ erg s^{-1} late in September and $8.1 \times 10^{36} \times d^2$ erg s^{-1} in November, where d is the distance to the source in kpc. The ratio of optical and X-ray energy fluxes is ~10^{-3} and shows that we have to do with a low-mass X-ray binary (LMXRB). Figure 4 displays the energy spectrum of GRS 1009–45 (for a better perception, this spectrum was displaced vertically). Also shown here for comparison is the spectrum of the hard X-ray nova GRO J0422+32.

An interesting example of X-ray novae is also the bright transient KS 1730–312 in Scorpius. It is peculiar in that its transition from the hard state to the soft one was recorded during the observations.

KS 1730–312 was discovered by TTM in September 1994. Between September 23 and 27, the (2–27 keV) flux from the source increased from 75 to 550 mCrab [14]. As the soft X-ray (2–10 keV) flux increased, the hard X-ray (10–27 keV) flux decreased. The source (2–27 keV) luminosity was ~10^{38} erg s^{-1} (the distance to the source was assumed to be ~8.5 kpc). During the TTM and SIGMA observations of the transient, we recorded its transition from the hard spectral state to the soft one. The studies based on Mir–Kvant, Granat, and GINGA data lead us to conclude that KS 1730–312 is a also black-hole candidate [15]. The source energy spectra in the two states are shown in Fig. 5. See [16] for an analysis of the best-fit parameters and a discussion of spectrum peculiarities.

X-ray pulsars. These are variable sources of periodic X-ray emission—rotating neutron stars with strong (~10^{11}–10^{14} G) surface magnetic fields emitting radiation due to accretion. The luminosities of most X-ray pulsars lie in the range ~10^{35}–10^{39} erg s^{-1}, and the pulse repetition periods range from ~0.5 s (GRO J1744–28) to several hundred seconds (for example, the period for the pulsar 4U 0535+30 is 835 s). Our catalog contains 13 such sources. As can be seen from Table 2, almost all representatives of this class from those observed by TTM lie within the Galaxy. Only two sources from the list belong to other galaxies: the Large and Small Magellanic Clouds; these are LMC X-4 and SMC X-1. The X-ray pulsars in high-mass binaries (there are nine such sources in our catalog except for the two extragalactic sources mentioned above) are mostly located near the Galactic plane. By contrast, the pulsars in low-mass binaries belong to the spherical component of the Galaxy. Two pulsars belonging to the LMXRB class and, nevertheless, lying in the Galactic plane, GX 1+4

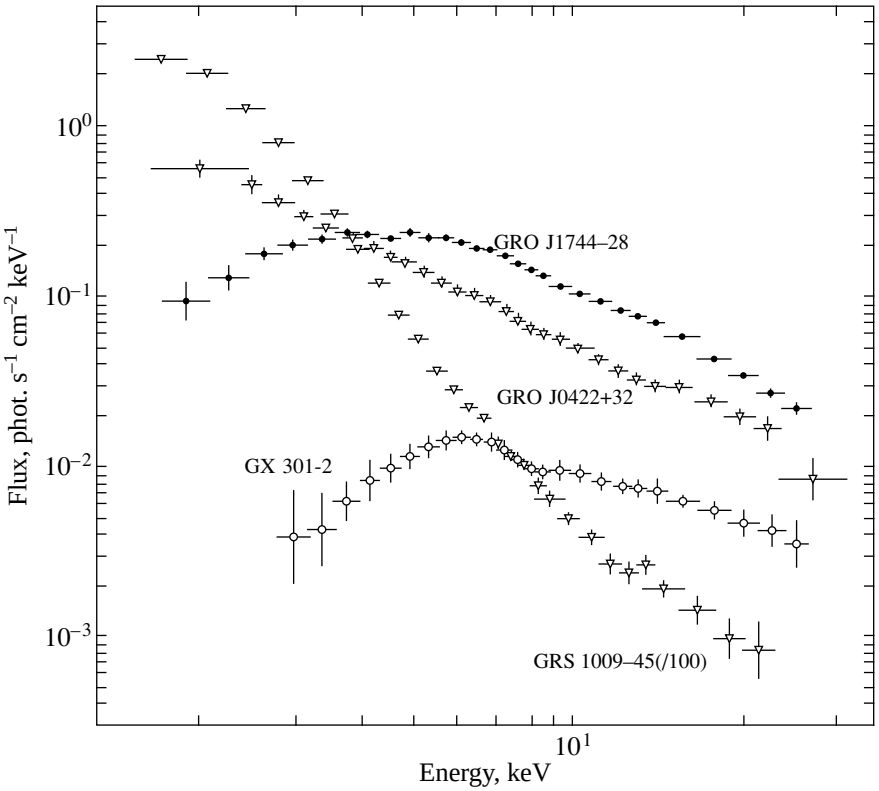

Fig. 4. TTM energy spectra for the typical pulsar GX 301-2, the transient bursting pulsar GRO J1744–28, the soft X-ray nova GRS 1009–45 (see text), and the hard X-ray nova GRO J0422+32.

and GRO J1744–28, are probably exceptions. Of all the X-ray pulsars in our catalog, only GRO J1744–28, A0535+26, GRS 0834–42, and 4U 0115+63 are transients; the flux from the remaining pulsars in the standard X-ray band varies only slightly. Let us consider GRO J1744–28 as an example.

GRO J1744–28 flared up in December 1995. This unique source combines the properties of a transient, a pulsar, and a burster. Over the period of TTM observations of the source, its flux dropped from ~800–900 mCrab during the first sessions (February 6–7, 1996) to ~270–540 mCrab during the last sessions (late March 1996 and February 1997). The source light curve exhibits two pronounced outbursts separated by about a year. Such light curves are typical of the Galactic microquasars GRS 1915+105 [17] and GRO J1655–40 [18] and were also observed for low-mass binaries with neutron stars, for example, 4U 1608–522 [19]. The pulsar belongs to a low-mass binary system and is a neutron star, in contrast to many transients—X-ray novae, which are universally accepted black-hole candidates. The shape of its spectrum (a power law with an exponential factor in the hard part, photon index $\gamma = 1.36$; see [20]) is typical of X-ray pulsars (see [21] for an in-depth analysis of spectrum peculiarities). As was revealed by ASCA and RXTE data and confirmed by TTM and HEXE observations, the source spectra at outburst maximum and minimum differ only slightly. For comparison, Fig. 4 shows the spectra of GRO J1744–28 and GX 301–2, a typical X-ray pulsar. The pulsation period for GRO J1744–28 is 467 ms [22, 23]. The distance to the source is assumed to be ~8 kpc. Its luminosity at maximum light was $(3.37 \pm 0.06) \times 10^{38}$ erg s^{-1} [21], which exceeds the Eddington luminosity limit for an $M \sim 1M_\odot$ star by at least a factor of 2.5. During all TTM sessions, the pulsar 2–27-keV luminosity exceeded or was approximately equal to the Eddington limit for a 1 $M_\odot$ neutron star (1.3×10^{38} erg s^{-1}). It was several tens of times higher during outbursts [24] and approximately an order of magnitude higher during bursts.

As was already said above, the pulsar standard spectrum has an exponential cutoff at energies above 5–30 keV (see [25] for a theoretical justification of this spectrum shape). As a result, emission at energies above 80 keV is detected only from a pair of the brightest objects. Thus, for example, TTM and HEXE recorded an unusually hard spectrum of the X-ray pulsar 4U 0115+63 during its outburst late in May 1994. It was described by a power law with $\gamma = 1.94 \pm 0.04$ ($\chi^2 = 36/37$) in the 2–100-keV band. Yet another pulsar, SAX J1808.4–3658 = XTE J1808–369, has recently been discovered, which also exhibits a hard power-law spectrum with an index of 2. The mechanism for the formation of a hard power-law spectrum in neutron stars has not yet been studied.

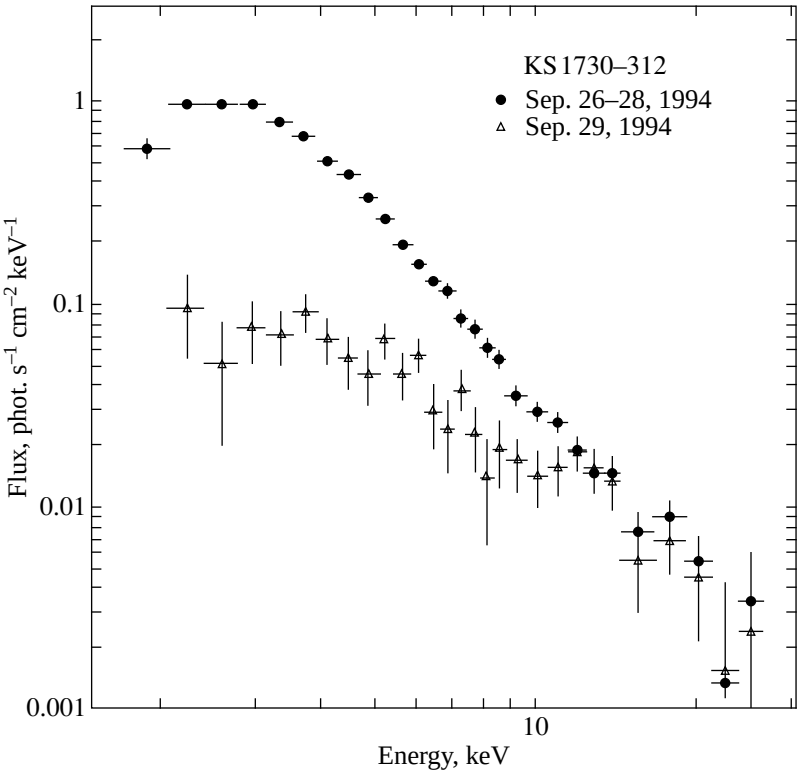

Fig. 5. TTM energy spectra for the transient X-ray nova KS 1730–312.

Bursters. These are bursting X-ray sources with burst repetition periods from several hours to several days and durations of several seconds. The interval between bursts is not constant; it varies in the range 30 and 50%. As the mean luminosity increases, the time between bursts decreases, and bursts disappear completely as a critical luminosity (~10^{37} erg s^{-1}) is reached. The radiation spectrum during bursts is similar to the spectrum of a blackbody with a temperature of ~6 keV. Between bursts, the bursters are X-ray sources with slowly varying fluxes and mean luminosities of ~10^{36}–10^{37} erg s^{-1}. All bursters belong to low-mass binaries and are located within the Galaxy. Moreover, most bursters lie within 30° of the Galactic-center direction, suggesting that they belong to the spherical subsystem of the Galaxy. Among the sources of this class (see Table 2), only GRO J1744–28 can be classified as a transient. The fluxes from the remaining sources are more or less constant.

Eighteen sources in our catalog can be classified as bursters. Here, one of the typical representatives is 4U 1705–44.

The X-ray burster 4U 1705–44 was observed by TTM in two spectral states, high/soft (a flux higher than 90 mCrab) and low/hard (a flux lower than 90 mCrab), similar to those previously observed by EINSTEIN and EXOSAT. The burster 4U 1705-44 in quiescence is a constant, bright X-ray source (see [26] for an in-depth analysis of the spectrum and radiation mechanisms for this source). Its 2–11-keV flux varied between ~0.3 and ~7×10^{-9} erg s^{-1} cm^{-2} [27]. The presumed period of the binary system is 222.8 days [28], and its distance is estimated to be 7.4 kpc [29]. An upper limit on the high-state 35–200-keV luminosity was found from SIGMA data to be 2.5×10^{36} erg s^{-1} (2σ), which accounts for less than 3% of the source total X-ray luminosity at a total (2–200 keV) luminosity of 8.7×10^{37} erg s^{-1} [26]. The high- and low-state 2–20-keV luminosities are ~2–6×10^{37} and ~1.5×10^{37} erg s^{-1}, respectively. The high- and low-state spectra of the source are shown in Fig. 6.

Black-hole candidates. According to current ideas, massive stars at the end of their evolution can contract (collapse) to turn into a black hole. No emission can leave a black hole. However, it was shown in the 1960s (see [30]) that, if a black hole is a member of a binary system, the attraction by this massive object can cause mass transfer from the companion star to produce an accretion disk. In this case, the hot plasma of the accretion disk emits X-ray radiation. The most solid argument that a source belongs to black holes is measurement of the mass of the compact object. To this end, the system's mass function is determined from optical observations, which is an absolute minimum mass of the compact object that does not depend on the distance to the system and the mass of the optical component. Theoretical calculations show that $M = 3M_\odot$ can be taken as a stringent upper limit on the neutron-star

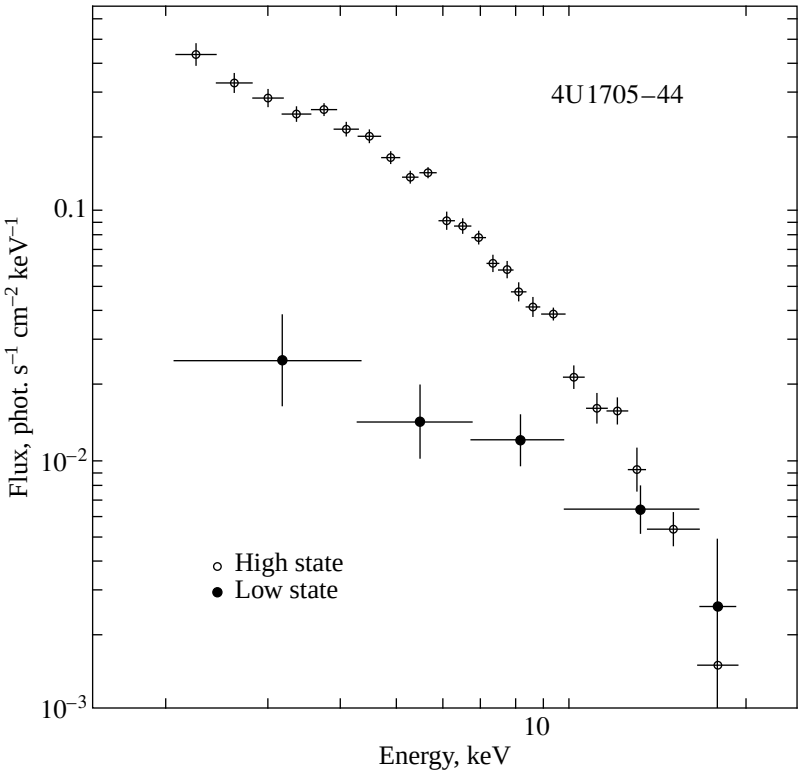

Fig. 6. TTM/COMIS energy spectra for the X-ray burster 4U 1705–44 in the high and low states.

mass. Seventeen sources in our catalog presumably belong to this class. Only three of them (LMC X-1, Cyg X-1, and Cyg X-3) are high-mass binaries, and the remaining ones are low-mass binaries. In addition, 11 sources are transient X-ray novae. All objects of this class lie in the Galactic plane, with the extragalactic source LMC X-1 in the Large Magellanic Cloud constituting an exception.

A distinctive feature of the black-hole candidates is their bimodal behavior, i.e., a transition from the soft state to the hard one and back. As a characteristic example of this kind of objects, let us consider the well-known quasi-stationary X-ray source Cyg X-1.

Cyg X-1 is a binary system with an orbital period of 5.6 days. It consists of a blue giant and a compact object, which is one of the most reliable black-hole candidates [31] because of the large mass function [$f(M) > 9.5M_{\odot}$] [31]. In the standard X-ray band (up to 20 keV), the source was observed in two states: high state (HS), in which it exhibits strong soft and weak hard components, and low state (LS), in which the component ratio reverses. During a transition from one state to the other, the flux variations in the soft and hard spectral parts are anticorrelated [32, 33]. The source spends ~90% of its time in the low state. Peculiarities of the spectrum, best-fit parameters, and low-frequency noise in the power spectrum, as inferred from TTM and HEXE data, can be found in [34]. Energy spectra of the source are shown in Fig. 7.

Extragalactic sources. As can be seen from the catalog itself or from Table 2, there are six sources of this class. Most of them are the same X-ray systems as those discussed above but located in the Large (LMC) and Small (SMC) Magellanic Clouds. The two remaining sources are the Seyfert 1 galaxy NGC 4151 and the radio galaxy Cen A. Of the sources belonging to the Magellanic Clouds, three have massive optical components, and one is a low-mass binary. Let us consider one of the objects of this class.

The radio galaxy Cen A was discovered in X rays about 30 years ago [35] and has since been observed by virtually all X-ray observatories. Cen A is the nearest galaxy with an active nucleus located at a distance of ~3.5 Mpc. Active galaxies account for ~1% of the normal galaxies (with inactive nuclei) by number. Optically, Cen A is a giant elliptical galaxy with a curved dust lane at the center, which obscures the central regions. The formation of Cen A can be explained as resulting from a collision of elliptical and spiral galaxies [36]. Cen A is one of the brightest extragalactic X-ray sources and a bright radio source. In the radio band, apart from the point source (nucleus), jets are observed, which are also visible in the soft X-ray band [37]. The source spectrum can be described by a power law with $\gamma \sim 1.51$–1.96, an emission line at energy of about 6.4 keV (an equivalent width of ~100 eV), and strong absorption $N_{\rm H} \sim (0.94$–$1.7) \times 10^{23}$ cm^{-2}. A data analysis suggests that the central nucleus of the galaxy is sur-

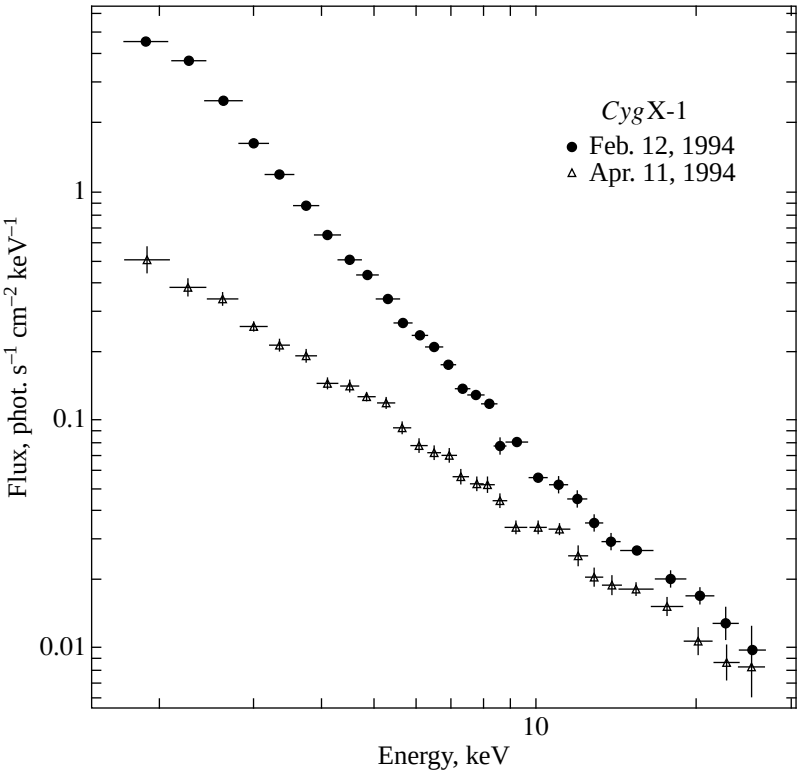

Fig. 7. TTM energy spectra for the black-hole candidate Cyg X-1.

rounded by a thick disk with inner and outer radii of 80 and 325 pc, respectively, and a thickness of ~80 pc [38]. The power-law spectrum of the source extends up to energies ~1 MeV [39], whereas some radio-quiet Seyfert galaxies, such as NGC 4151, emit radiation only up to several hundred keV. A study of radiation peculiarities, presumed models, and an in-depth analysis of the energy spectrum for this object can be found in [40–42] and references therein.

CONCLUSION

Based on data from the TTM/COMIS X-ray spectrometer of the Roentgen observatory onboard the Kvant module of the Mir orbiting station, we have analyzed the observations of bright sources by individual sessions and compiled their catalog. TTM had long remained the only instrument that could effectively observe the Galactic center and other densely populated regions of the X-ray sky because of its high angular resolution and fairly wide field of view. This unique information is systematized and presented here. We also investigated the main classes of sources included in the catalog, gave their brief descriptions, considered examples typical of each class, elucidated the radiation mechanisms, and presented the energy spectra. The observations span the period from October 21, 1988, through December 1998. One of the first results of the Roentgen observatory is the observation of hard X-ray emission from the supernova SN 1987A exploded in 1987 in the Large Magellanic Cloud [43–47]. Currently, the software for the reduction of observing sessions is being updated, and the work will subsequently be continued. Based on TTM data, we plan to carry out studies by using information for the sum of sessions.

ACKNOWLEDGMENTS

This study was supported in part by the Russian Foundation for Basic Research (project nos. 97-02-16264 and 96-15-96343). We wish to thank K.N. Borozdin and V.A. Aref'ev for a discussion of the results and valuable remarks, as well as V.G. Rodin, A.V. Prudkoglyad, and the staff of the Flight Control Center, who operated the station and the scientific instrumentation. We are also grateful to A.N. Ananenkova for a preliminary reduction of telemetry data.

REFERENCES

1. N. Aleksandrovich, K. Borozdin, and R. Sunyaev, IAU Circ., No. 6080 (1994).
2. N. Aleksandrovich, V. Aref'ev, K. Borozdin, *et al.*, Pis'ma Astron. Zh. **21**, 486 (1995) [Astron. Lett. **21**, 431 (1995)].
3. R. Sunyaev, K. Borozdin, N. Aleksandrovich, *et al.*, Pis'ma Astron. Zh. **20**, 890 (1994) [Astron. Lett. **20**, 777 (1994)].

4. A. Brinkman, J. Dam, W. Mels, *et al.*, in *Non-thermal and Very High Temperature Phenomena in X-ray Astronomy*, Ed. by G. C. Perola and M. Salvati (Inst. Astron., Rome, 1985), p. 263.
5. C. Reppin, W. Pietsch, J. Truemper, *et al.*, in *Non-thermal and Very High Temperature Phenomena in X-ray Astronomy*, Ed. by G. C. Perola and M. Salvati (Inst. Astron., Rome, 1983), p. 279.
6. N. Aleksandrovich, V. Aref'ev, K. Borozdin, and A. Prudkoglyad, Preprint No. 1959 (Inst. Kosmich. Issled. Ross. Akad. Nauk, 1996).
7. P. Amnuel, O. Guseinov, and Sh. Rakhamimov, Astrophys. J., Suppl. Ser. **41**, 327 (1979).
8. K. Wood, F. Meekins, D. Yentis, *et al.*, Astrophys. J., Suppl. Ser. **56**, 507 (1984).
9. K. Long, D. Helfand, and D. Grabelsky, Astrophys. J. **248**, 925 (1981).
10. R. Sunyaev, M. Gilfanov, E. Churazov, *et al.*, Pis'ma Astron. Zh. **16**, 136 (1990) [Sov. Astron. Lett. **16**, 55 (1990)].
11. N. White and F. Marshall, Astrophys. J. **281**, 354 (1984).
12. S. Grebenev, R. Sunyaev, and M. Pavlinsky, Adv. Space Res. **19**, 15 (1997).
13. I. Lapshov, S. Sazonov, and R. Sunyaev, IAU Circ., No. 5864 (1993).
14. K. Borozdin, N. Aleksandrovich, and R. Sunyaev, IAU Circ., No. 6088 (1994).
15. S. Trudolyubov, M. Gilfanov, E. Churazov, *et al.*, Pis'ma Astron. Zh. **22**, 740 (1996) [Astron. Lett. **22**, 664 (1996)].
16. K. Borozdin, N. Aleksandrovich, V. Aref'ev, *et al.*, Pis'ma Astron. Zh. **21**, 243 (1995) [Astron. Lett. **21**, 212 (1995)].
17. S. Sazonov, R. Sunyaev, I. Lapshov, *et al.*, Pis'ma Astron. Zh. **20**, 901 (1994) [Astron. Lett. **20**, 787 (1994)].
18. S. Zhang, K. Ebisawa, R. Sunyaev, *et al.*, Astrophys. J. **479**, 381 (1997).
19. J. Lochner and D. Roussel-Dupré, Astrophys. J. **435**, 840 (1994).
20. T. Dotani, Y. Ueda, M. Ishida, *et al.*, IAU Circ., No. 6337 (1996).
21. N. Aleksandrovich, K. Borozdin, V. Aref'ev, *et al.*, Pis'ma Astron. Zh. **24**, 10 (1998) [Astron. Lett. **24**, 7 (1998)].
22. M. Finger, C. Robinson, B. Harmon, and B. Vaugham, IAU Circ., No. 6530 (1997).
23. V. Borkus, A. Kaniovskiĭ, R. Sunyaev, *et al.*, Pis'ma Astron. Zh. **23**, 483 (1997) [Astron. Lett. **23**, 421 (1997)].
24. S. Sazonov, R. Sunyaev, and N. Lund, Pis'ma Astron. Zh. **23**, 326 (1997) [Astron. Lett. **23**, 286 1997)].
25. R. Sunyaev, V. Aref'ev, K. Borozdin, *et al.*, Pis'ma Astron. Zh. **17**, 975 (1991) [Sov. Astron. Lett. **17**, 409 (1991)].
26. M. Revnivtsev, M. Gilfanov, E. Churazov, *et al.*, in *Proc. 2nd INTEGRAL Workshop "The Transparent Universe,"* ESA SP-382 (St. Malo, France, 1996), p. 185.
27. J. Brandt and J. McClintock, Ann. Rev. Astron. Astrophys. **21**, 13 (1983).
28. W. Priedhorsky, Astrophys. Space Sci. **126**, 89 (1986).
29. F. Haberl and L. Titarchuk, Astron. Astrophys. **299**, 414 (1995).
30. Ya. B. Zel'dovich, Dokl. Akad. Nauk SSSR **155**, 67 (1964).
31. N. Walborn, Astrophys. Lett. **179**, 123 (1973).
32. J. Dolan, C. Crannel, B. Dennis, *et al.*, Nature **267**, 813 (1977).
33. Y. Ogawara, K. Midsuda, and K. Massai, Nature **295**, 675 (1982).
34. V. Borkus, A. Kaniovskiĭ, V. Efremov, *et al.*, Pis'ma Astron. Zh. **21**, 883 (1995) [Astron. Lett. **21**, 794 (1995)].
35. C. Bowyer, M. Lampton, J. Mack, and G. de Mendonca, Astrophys. J. Lett. **161**, L1 (1970).
36. K. Ebneter and B. Balick, Publ. Astron. Soc. Pacif. **95**, 675 (1983).
37. E. Feigelson, E. Schreier, J. Delvaille, *et al.*, Astrophys. J. **251**, 31 (1981).
38. F. Israel, E. van Dishoeck, F. Baas, *et al.*, Astron. Astrophys. **227**, 342 (1990).
39. H. Steinle, K. Bennett, H. Bloemen, *et al.*, Astron. Astrophys. **330**, 97 (1998).
40. M. Maisak, E. Kendziorra, B. Mony, *et al.*, Astron. Astrophys. **262**, 433 (1992).
41. D. Rothschild, P. Band, D. Blanco, *et al.*, Astrophys. J. **510**, 651 (1999).
42. M. Sugizaki, H. Inoue, T. Sonobe, *et al.*, Publ. Astron. Soc. Jpn. **49**, 59 (1997).
43. R. Sunyaev, A. Kaniovskii, V. Efremov, *et al.*, Nature **330**, 230 (1987).
44. R. Sunyaev, A. Kaniovskiĭ, V. Efremov, *et al.*, Pis'ma Astron. Zh. **13**, 136 (1987) [Sov. Astron. Lett. **13**, 431 (1987)].
45. R. Sunyaev, V. Efremov, A. Kaniovskiĭ, *et al.*, Pis'ma Astron. Zh. **14**, 579 (1988) [Sov. Astron. Lett. **14**, 247 (1988)].
46. R. Sunyaev, A. Kaniovskiĭ, V. Efremov, *et al.*, Pis'ma Astron. Zh. **15**, 291 (1989) [Sov. Astron. Lett. **15**, 125 (1989)].
47. R. Sunyaev, A. Kaniovskiĭ, V. Efremov, *et al.*, Pis'ma Astron. Zh. **16**, 403 (1990) [Sov. Astron. Lett. **16**, 171 (1990)].

Translated by V. Astakhov

Astronomy Letters, Vol. 26, No. 5, 2000, pp. 309–318. Translated from Pis'ma v Astronomicheskiĭ Zhurnal, Vol. 26, No. 5, 2000, pp. 369–379.

Non-LTE Effects for Na I Lines in X-ray Illuminated Stellar Atmospheres

N. A. Sakhibullin and V. V. Shimansky*

Kazan State University, ul. Lenina 18, Kazan, 420008 Tatarstan, Russia

Received June 8, 1999

Abstract—The formation of Na I lines in X-ray illuminated atmospheres is investigated by abandoning the assumption of local thermodynamic equilibrium (LTE). Calculations are performed on the basis of a 21-level Na I model atom for the LTE model atmospheres of irradiated F–G stars obtained with allowance for a reflection effect in the first approximation. The state of extreme "overrecombination" is shown to exist for the populations of all Na I levels in the case of external illumination. Absorption features in the profiles of "cool" and "normal" Na I lines have been found to be enhanced compared to the LTE approximation. Effects of the angle of incidence and intensity of the external radiation on the formation of level populations and line profiles when abandoning LTE are analyzed. The existence of overrecombination for Na I is explained by the small X-ray heating function and the large optical cooling function. Na I level populations are shown to depend weakly on the presence of "overionization" for Na II in the atmospheres of irradiated stars. *© 2000 MAIK "Nauka/Interperiodica".*

Key words: *stars—structure and evolution, binary stars, stellar atmospheres*

INTRODUCTION

The theoretical studies of externally illuminated stellar atmospheres carried out over the last twenty years show that, in most cases, they have thick hot chromospheres and coronas and qualitatively differ in structure from normal atmospheres. A significant difference between the absorption coefficients at the frequencies of intrinsic and external radiation, which are the cofactors in the cooling and heating functions of the medium, is mainly responsible for this phenomenon. The computed LTE temperature distributions in irradiated atmospheres reflect the ratios of only total (i.e., integrated over all elements) absorption coefficients in different spectral ranges. For atoms and ions of individual elements, these ratios can be markedly different, and the existing temperature distribution does not reflect the ionization and radiative balance for them. As a result, many elements will have significant departures from LTE; i.e., their level populations can differ greatly from those derived from the Saha and Boltzmann formulas. Similar effects are also present in the atmospheres of normal stars, but they are considerably weaker there, because all radiation concentrates in a relatively narrow spectral range.

An exact non-LTE modeling of externally illuminated stellar atmospheres is currently running into significant difficulties, which are associated with the need for a simultaneous constant recalculation of the radiative and collisional processes for a large number of elements in several ionization stages. In addition, reliable data on the oscillator strengths and ionization cross sections are not available for all major elements, while the parameters of collisional processes for many atoms and ions are not known at all.

It is for these reasons that non-LTE studies of irradiated atmospheres has just begun, and two approaches are used in them. In their studies devoted to the formation of radiation in the spectrum of HZ Her, several authors [1–3] used floating ionization equilibrium with allowance for the rates of recombination and ionization from the ground levels of several successive stages of six to eight major elements when computing model atmospheres. More accurate calculations of ionization equilibrium were performed by London *et al.* [4] and Anderson [5], who partially took into account the influence of hydrogen and helium lines. These authors showed that the H I and He I atoms with low ionization potentials are heavily overpopulated compared to LTE ("overrecombination"), while the He II ion with a high ionization potential is underpopulated ("overionization").

Another approach was used by Mitskevich and Tsymbal [6], who computed the illumination effect from the coronas of B stars on the basis of LTE model atmospheres and a 128-level He I model atom. They established that, at the lowest X-ray flux (10^{-7}–10^{-8} of the total stellar flux), the He I atom makes a transition to the state of strong overionization, while its absorption lines weaken and can become emission ones. Proga *et al.* [7] computed departures from LTE for

* E-mail address for contacts: Slava.Shimansky@ksu.ru

1063-7737/00/2605-0309$20.00

12 major elements with allowance for lines together with the determination of the temperature distribution on the basis of balance between the cooling and heating functions. The calculations were performed for the atmospheres of G–M giants and supergiants belonging to the group of symbiotic stars. These authors were able to obtain synthetic non-LTE spectra for such systems with observable emission lines of several species (H, He I, Mg II, Ca II, Fe II).

To summarize, we can say that non-LTE effects in illuminated atmospheres have been investigated by relatively few authors. The main problem solved by these authors was to determine specific non-LTE departures for the selected lines in specific stars. Attention was focused on elements that were most affected by external illumination, and the analysis of the physical mechanisms responsible the emergence of departures from LTE was very limited. Meanwhile, comprehending the nature of non-LTE effects in irradiated atmospheres makes it possible to extend the results obtained to other objects with different atmospheric and external-illumination parameters and provides a means of predicting non-LTE departures for other elements. Here, by analyzing non-LTE corrections for Na I lines in the illuminated atmospheres of F–K stars, we therefore attempt to understand the physics of the phenomenon for elements with low ionization potentials and to predict their behavior in irradiated atmospheres in the non-LTE case.

METHOD OF CALCULATION

Here, we used a two-step method of studying possible non-LTE departures in the atmospheres of illuminated stars:

(1) Model atmospheres of the illuminated stars were computed in the LTE approximation by using the BINARY3 code for computing blanketed model atmospheres [8] and the BINARY2 code for allowing for a reflection effect in the semi-gray approximation [9];

(2) Non-LTE departures for specific atoms and ions were computed by using the NONLTE3 software package [10], which was specially modified to include ionization by external X-ray radiation.

We investigated non-LTE effects mostly for Na I lines, which can form only in stars with low effective temperatures, $T_{\rm eff}$ = 4000–9000 K. Blanketed models of irradiated atmospheres with convective transfer are very difficult to compute, and the grid of computed models is clearly not adequate for non-LTE studies. We therefore used models computed by using the BINARY2 code with allowance for a reflection effect, which is not quite suitable for describing deep layers of convective models but yields a uniform grid of models that are not subject to errors of the iteration process. The method of allowing for a reflection effect in the semi-gray approximation was described in [9] and modified in [8, 11]. We used Kurucz's models [12] as the input ones. A power-law spectrum of the external radiation, $I_x(\nu) = I_x\nu^{-1.0}$, with cutoff energy E_0 = 1.0 keV was used in all calculations. This X-ray spectrum is typical of many sources, such as HZ Her etc.

The Na I model atom containing 21 levels (all Na I levels with $n \le 7$, $l \le 3$ and the Na II ground state $1s^22s^22p^6{}^1S_0$) includes 80 bound–bound and 20 bound–free transitions, 46 of which (mostly transitions from the 3*s*, 3*p*, 3*d*, 4*s*, 4*p*, 5*s*, and 4*d* levels) were linearized (i.e., they were recalculated during iterations) and 54 transitions (including all bound–free ones) were fixed. The corresponding Grotrian diagram is shown in Fig. 1. This model atom is a generalized version of the 20-level model that has been repeatedly used to study normal stars [13–18]. The level energies $E_{\rm ex}$ were taken from [19]. To compute the photoionization rates σ_ν for all levels, we used Hofsaess's data [20] fitted by the formula

$$\sigma_\nu = \left(\alpha + \frac{E_{\rm ion}}{\Delta E_\nu}\right)^2 \sigma_0 \nu^s, \qquad (1)$$

where $E_{\rm ion} = h\nu_{\rm ion}$ is the threshold energy of ionization from the level; $\Delta E_\nu = h\nu$ is the transition energy at a given frequency; and σ_0, α, s are the fitting coefficients.

Complete data on the levels of our model atom and on the fitting coefficients for the ionization cross sections are given in Table 1. When determining the set of oscillator strengths, we used a compilation of several sources [21–26], whose data differ by no more than 5–10%.

The rates of collisions by free electrons were computed by using the data of several authors [27–31]. For permitted transitions, we also took into account collisional excitation and ionization by hydrogen atoms, as estimated by Steenbock and Holweger [32]. Experience shows that the derived collision rates are overestimated, and they are commonly used with the scaling factor k = 0.1–1.0. A non-LTE analysis of the solar spectrum [18] yielded the range of scaling factor k = 0.1–0.33. Here, we assumed k to be 0.20.

In addition, we took into account ionization from the inner 1*s*, 2*s*, and 2*p* shells by the external X-ray flux. The cross sections for ionization from these shells were taken in accordance with the six-parameter formula derived by Yakovlev *et al.* [33]. We performed our non-LTE calculations for the Na I atom by assuming that ionization from its inner shells gives rise to Na II, because this is the dominating ionization stage, and the subsequent ionization does not affect the statistical equilibrium of Na I. Below, we show the validity of this assumption. The cross sections were computed only for unexcited atoms and ions. However, we used them to allow for ionization from all levels, because the degree of excitation of an outer electron affects only slightly the inner-shell configuration. Since the contribution of Na I inner shells to the total X-ray absorption coefficient is extremely small (no more than 10^{-10}), we assumed the radiation field in a given region to be inde-

pendent of the sodium level populations and the corresponding transitions to be fixed.

The line profiles and equivalent widths were computed by taking into account Stark, Doppler (with typical microturbulence V_{turb} = 2 km s^{-1}), and Van der Waals broadenings and natural damping. We took the constants C_4 and C_6 from [13, 34] and the constants of natural damping γ_R from [21]. Complete data on the lines under study and the constants are presented in Table 2. Several lines exhibit fine and hyperfine splittings [22, 35], which were also taken into account.

We performed our non-LTE calculations by using the NONLTE3 software package, which realizes the complete linearization method in the version of Auer and Heasley [36] and was described in detail by Sakhibullin [10]. To carry out these studies with the NONLTE3 package, we made changes associated with calculation of the X-ray radiation field and additional ionization and recombination rates. The START code included the POPS and PFSAHA subroutines from the ATLAS5 package [37] to compute LTE populations of the twenty most important elements and the OPREN and OPRALL subroutines from the BINARY3 package [8] to compute the opacities and the X-ray radiation field.

RESULTS

Figures 2a and 2b show the distributions of *b*-factors ($b_i = \frac{n_{\text{non-LTE}}}{n_{\text{LTE}}}$, where $n_{\text{non-LTE}}$ and n_{LTE} are the non-LTE and LTE populations of level *i*) on the scales of Rosseland optical depths for a model with T_{eff} = 6000 K and $\log g$ = 4.0 with external illumination (with the intensity of incident X-ray flux $K_x = \frac{\mu J_x}{\sigma T_{\text{eff}}^4}$ = 1.00, in units of the total emitted flux from an unilluminated atmosphere, and the cosine of the angle of incidence of the external radiation μ = 1.00) and without it. Let us briefly describe the mechanism of departures from LTE for Na I in unilluminated atmospheres established in [13–18, 21, 38].

In deep layers, the LTE approximation holds with a high accuracy, because the collision rates in them are much larger than the radiative ones and because the mean intensity is equal to the source function at all frequencies. Departures begin above a depth $\tau\nu \approx 1.0$ for the ground-level (mostly 3*p* and 3*d*) continua. The phenomenon of "overionization," which was established for a number of neutral atoms in the atmospheres of F–K stars, does not show up for Na I, because the cross section of its ground state is small. The inverse phenomenon of "overrecombination" therefore takes place, which is caused by the drop in large quantities of atoms from upper states to lower ones over the channel 4*f*, 5*f*, 6*f*, 7*f*–3*d*, 4*d*–3*p*–3*s*. As a result, the lower Na I

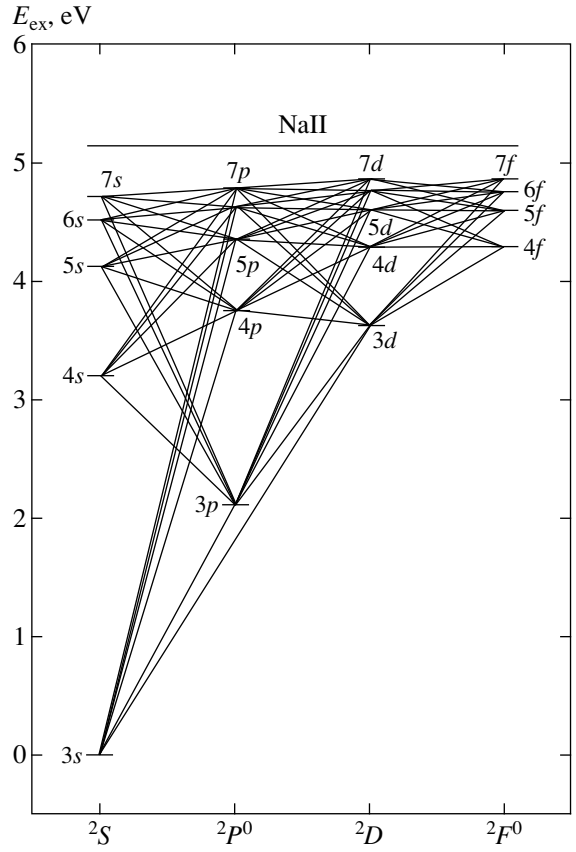

Fig. 1. The Na I model atom.

states are overpopulated, while the lines are enhanced because of an increase in the source function

$$S_{ji} = \frac{2h\nu^3}{c^2}\frac{1}{\frac{n_i g_j}{n_j g_i} - 1} = \frac{2h\nu^2}{c^2}\frac{1}{\frac{b_i}{b_j}e^{\frac{h\nu}{kT}} - 1} \approx \frac{b_j}{b_i}B_\nu(T) \quad (2)$$

(where b_i and b_j are the *b* factors of the lower and upper transition levels, respectively), and the displacement of their formation depth to higher, cooler layers. A complete depopulation of the upper levels is prevented by collisional pumping on them of atoms from the continuum as soon as their populations become smaller than their LTE values.

A comparison of the *b* factors for illuminated and unilluminated models revealed a significant difference in the formation of non-LTE populations in them. The populations of all levels, including the uppermost ones, in irradiated atmospheres turn out to be larger than those for LTE. Thus, there is no collisional pumping of atoms to the Na I state in these atmospheres, and direct radiative transitions from the continuum to all levels take place. The number of atoms ionized by radiation at a given frequency is proportional to the mean intensity $J_\nu \approx WS_\nu$ (τ_ν = 1.0) (where the dilution factor *W* ranges from 1/2 to 1), while the number of recombined atoms is

Table 1. Data on the levels in the Na I model atom (ν_{ion} is the threshold ionization frequency; g_i is the statistical weight; and σ_0, α, s are the fitting parameters for the ionization cross section)

Level	$\nu_{ion} \times 10^{-14}$	g_i	σ_0, Mb	α	s
$3s^2S$	12.426176	2	3.079	–0.801	–1.731
$3p^2P^0_{1/2}$	7.3435062	2	0.00011	–247.9	–3.588
$3p^2P^0_{3/2}$	7.3386702	4	0.00011	–247.9	–3.588
$4s^2S$	4.7095837	2	3.991	–0.534	–1.352
$3d^2D$	3.6804502	10	5.207	–2.861	–4.186
$4p^2P^0$	3.3817466	6	0.00037	–219.8	–1.161
$5s^2S$	2.4729452	2	5.277	–0.360	–3.300
$4d^2D$	2.0688118	10	16.84	–2.428	–3.743
$4f^2F^0$	2.0573508	14	17.29	–2.023	–4.985
$5p^2P^0$	1.9211027	6	2.152	–4.740	–1.040
$6s^2S$	1.5219143	2	6.919	–0.251	–3.287
$5d^2D$	1.3197923	10	52.85	–1.960	–3.640
$5f^2F^0$	1.3165582	14	0.706	–9.984	–4.230
$6p^2P^0$	1.2449084	6	9.268	–3.148	–0.950
$7s^2S$	1.0305585	2	8.836	–0.181	–3.243
$6d^2D$	0.9181373	10	85.54	–1.864	–3.498
$6f^2F^0$	0.9142400	14	173.2	–1.580	–4.450
$7p^2P^0$	0.8719696	6	19.91	–2.678	–3.187
$7d^2D$	0.6741082	10	122.6	–1.796	–3.389
$7f^2F^0$	0.6717110	14	301.5	–1.509	–4.278
NaII	114.36000	1			

proportional to the source function S_ν. At any depth τ_r, there is a frequency ν in unilluminated models below and above which the conditions $J_\nu < S_\nu$ and $J_\nu > S_\nu$, respectively, are satisfied; this determines the dominance of recombination or ionization in these spectral ranges. As we showed previously [8], a chromospheric region with an electron temperature higher than the temperature at the continuum formation depth is formed in the high layers of irradiated models. In these layers, the condition $J_\nu < S_\nu$ is satisfied for all frequencies, and recombination takes place in them. Additional ionization by external X-ray radiation proves to be inefficient for Na I, because its contribution to the total absorption coefficient is very small ($\sim 10^{-10}$) in the X-ray band and relatively large ($\sim 10^{-4}$) in the optical band. Thus, ionization by an external X-ray flux has virtually no effect on the statistical equilibrium of Na I, and the latter is determined by the atmospheric structure alone. Cascade transitions in the Na I atom in illuminated models are also enhanced because of the enhancement of the source function. As a result, the lower atomic levels are greatly overpopulated up to $b_i = 40$ in the 3*s* ground state.

Figures 2c and 2d show the distributions of *b* factors for models with a smaller illumination ($K_x = 0.25$, $\mu = 1.00$) and a larger angle of incidence ($K_x = 1.00$, $\mu = 0.25$). The overrecombination for Na I is rapidly enhanced at a small external illumination ($K_x < 0.10$), which is attributable to the emergence of a negative temperature gradient $\frac{dT_e}{d\tau_r}$ in the high layers. Collisional transitions begin to hinder a further enhancement of overrecombination, because the difference between the level *b* factors becomes great. An increase in the angle of incidence of the external radiation affects differently the statistical equilibrium in the uppermost and deeper layers. At small μ, the main heating displaces to the region with $\log\tau_r < -3$, where a thick chromosphere with a steep rise in temperature emerges. At the continuum formation depth, the temperatures changes only slightly, and the condition $J_\nu \ll S_\nu$ is satisfied for such atmospheres. This causes the overrecombination to be further enhanced in the chromospheric layers. In

Table 2. Data on the Na I lines

λ	Transition	$f_{i,j}$	$\gamma_R \times 10^8$	$C_4 \times 10^{-14}$	$C_6 \times 10^{-30}$
5889.97	$3s^2S$–$3p^2P^0_{3/2}$	0.647	0.629	0.126	0.066
5895.84	$3s^2S$–$3p^2P^0_{1/2}$	0.322	0.630	0.126	0.067
6154.23	$3p^2P^0_{1/2}$–$5s^2S$	0.014	0.754	9.05	1.67
6160.75	$3p^2P^0_{3/2}$–$5s^2S$	0.014	0.758	9.05	1.67
5688.21	$3p^2P^0_{3/2}$–$4d^2D$	0.097	0.820	4.51	1.86
5682.64	$3p^2P^0_{1/2}$–$4d^2D$	0.097	0.816	4.51	1.86
8183.26	$3p^2P^0_{1/2}$–$3d^2D$	0.830	0.720	9.05	0.452
8194.82	$3p^2P^0_{3/2}$–$3d^2D$	0.833	0.720	9.05	0.452

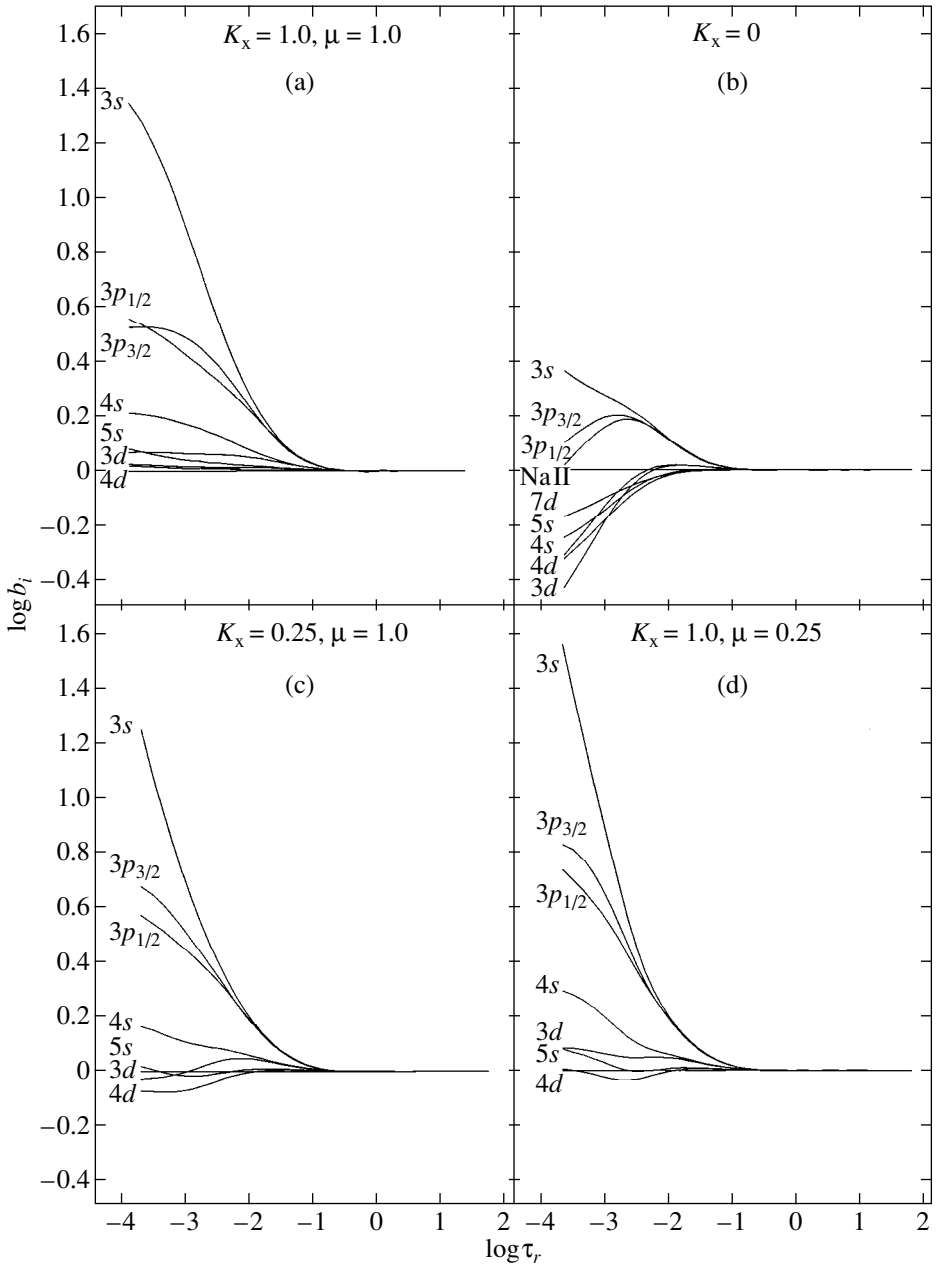

Fig. 2. The distributions of *b* factors for the Na I ground levels with Rosseland depth τ_r for model atmospheres with $T_{\rm eff}$ = 6000 K and log *g* = 4.0 with [(a) K_x = 1.00, μ = 1.00; (c) K_x = 0.25, μ = 1.00; (d) K_x = 1.00, μ = 0.25] and without external illumination (b).

deeper layers, the rise in temperature is attributable to the constant term of the heating function $S_3 = \frac{\mu J_0}{\sqrt{3}}$ alone [9], and it changes with depth only slightly. As a result, the initial temperature gradient for unilluminated atmospheres is preserved, and the overrecombination is reduced compared to the vertically incident radiation.

Departures from LTE in level populations are responsible for the changes in the Na I line profiles, some of which are shown in Fig. 3. The Na I ionization potential is 5.14 eV, which corresponds to $E_{\rm ion} \approx (7–10)kT_{\rm eff}$ at $T_{\rm eff}$ = 4000–7000 K, and the sodium lines in the atmospheres of F–G stars, according to our classification [11], can be classified as "cool" and "normal" ones. Several peculiarities can be noted in the LTE and non-LTE profiles of these lines:

(1) There is a general weakening of the Na I lines both under and without the assumption of LTE.

(2) The departures from LTE are the same over a wide range of temperatures ($T_{\rm eff}$ = 4000–7000 K) and surface gravities ($\log g$ = 1.5–4.5), which is attributable to the fact that the Na I lines invariably belong to the groups of cool and normal lines.

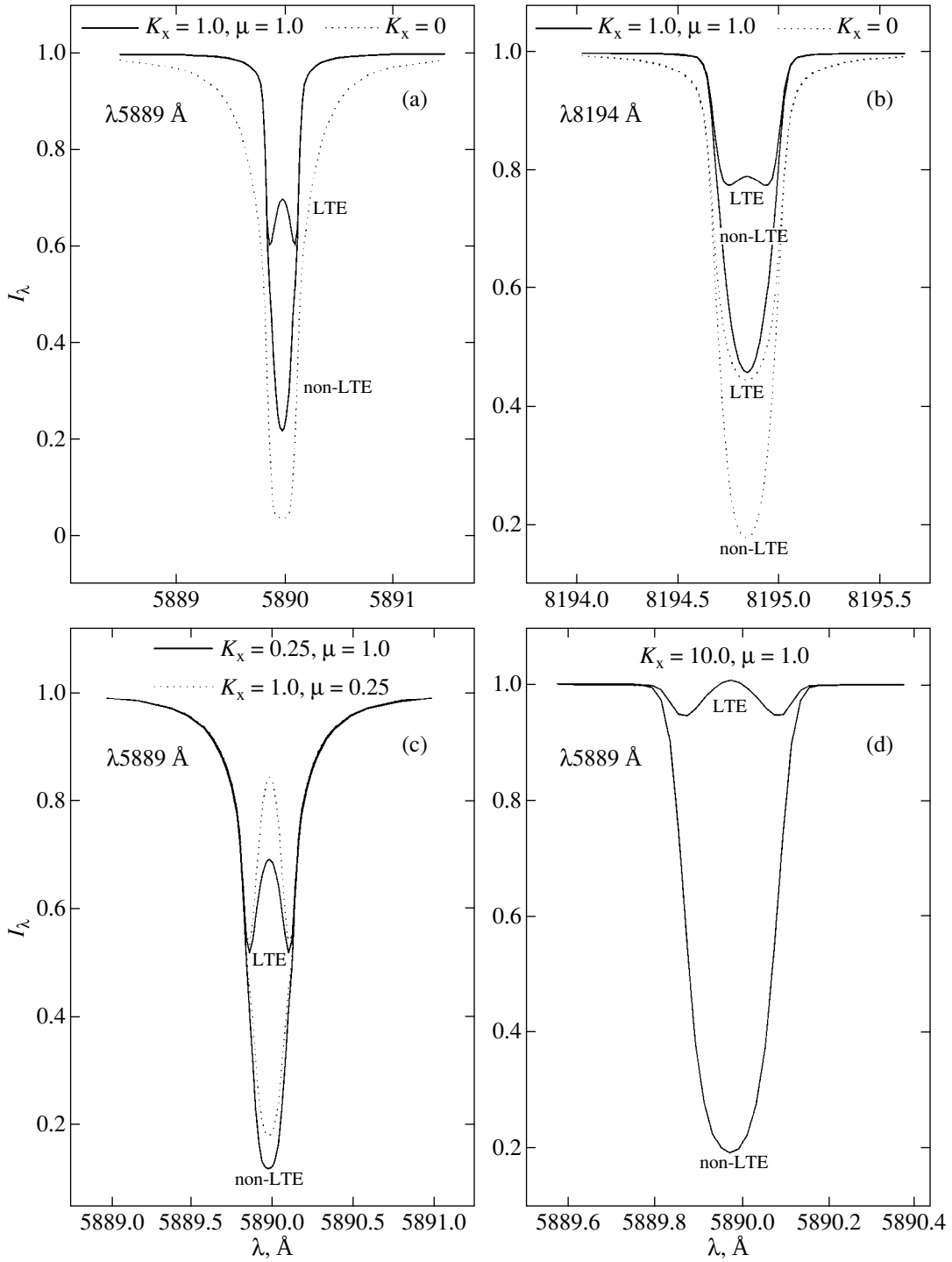

Fig. 3. The λ = 5895, 8194 Å Na I line profiles for stellar model atmospheres with T_{eff} = 6000 K, log g = 4.0 (a)–(c) and T_{eff} = 4000 K, log g = 4.0 (d) for various external illuminations and without it.

(3) There is a significant enhancement of the departures from LTE with the emergence of external radiation for the resonance and subordinate lines. In this case, the LTE profiles of the λ = 5889, 5895 Å resonance lines under external radiation must have weak emission cores, which is typical of normal lines [9]. The non-LTE profiles of these lines exhibit no such cores and may well be classified as cool lines.

(4) For the same illuminating flux $H_x = \mu K_x$, the larger line weakening shows up at small μ for both the LTE and non-LTE profiles. For cases with different angles of incidence of the radiation, the differences in residual intensities $I_\lambda(\mu_1) - I_\lambda(\mu_2)$ are the same for the LTE and non-LTE profiles.

(5) Cases are possible (Fig. 3d) where the Na I lines prove to be weak emission ones in the LTE approxima-

tion and absorption ones with equivalent widths up to 300 mÅ in the absence of LTE. *Thus, given the non-LTE effects, not only quantitative but also qualitative changes can occur in the Na I line spectrum!*

The described non-LTE changes in the line profiles can be readily explained by using formula (1). As was pointed out above, the level overpopulation grows with decreasing excitation energy, the b factor of the 3s ground state is 4 to 8 times larger than the b factor of the excited 3p level, and, hence, the non-LTE source function decreases by the same factor compared to the Planck function. Thus, although the Planck function is larger for chromospheric layers than that at the continuum formation depth (by a factor of 1.5–2.5), the non-LTE source function for them proves to be smaller (by a factor of ≤ 5). The 3p state is also more overpopulated than the higher-lying 3d, 4d, and 5s levels. This determines the enhancement of all subordinate lines, given the departures from LTE.

To characterize departures from LTE, we propose to use the quantity

$$\Delta = \frac{W_{\text{non-LTE}}}{W_{\text{LTE}}}, \quad (3)$$

where W_{LTE} and $W_{\text{non-LTE}}$-LTE are the line equivalent widths for LTE and non-LTE, respectively. We abandoned the commonly used characteristic

$$\Delta X = X_{\text{non-LTE}} - X_{\text{LTE}}, \quad (4)$$

where $X_{\text{non-LTE}}$ and X_{LTE} are the sodium abundances derived from the same W_λ in two (non-LTE and LTE) approaches. This characteristic for irradiated models has no physical meaning and, occasionally, cannot be determined at all (see Fig. 3d). Figure 4 shows variations of Δ for various intensities of external illumination K_x and various angles of incidence. For different lines, we found no distinct maximum of departures from LTE at various K_x. For weak lines, the maximum generally occurs earlier and is associated with the passage of the line to a linear segment of the curve of growth and with the displacement of its formation region to very deep layers, where the b factors of the upper and lower levels come close together. The maximum for the resonance lines is reached at the largest illumination ($K_x = 20$), and the point of this maximum depends on stellar temperature. As the angle of incidence of the external radiation varies, a distinct maximum of departures from LTE appears for all lines. For obliquely incident radiation, the heating of chromospheric layers is largest compared to continuum heating. This causes an enhancement of emission features in the line profiles and, hence, a growth of the non-LTE effects that offset this enhancement. Note that the position of the maximum displaces to smaller μ with decreasing temperature and increasing external radiation, but, in general, lies in the range $\mu = 0.33$–0.50.

To summarize, we conclude that, for cool and normal lines of atoms at an ionization stage that is not the main one in X-ray illuminated atmospheres, non-LTE effects must exist, which cause an enhancement of the absorption components of such lines. Such effects arise, because the ionization of Na I atoms by the external X-ray radiation is insignificant, and because their optical cooling function is large. Concurrently, part of the absorbed external radiation is reradiated in the Paschen and Balmer continuum bands and causes the ionization in the Na I atom to be enhanced. As a result, the Na I absorption lines weaken compared to unilluminated atmospheres, even in the absence of LTE.

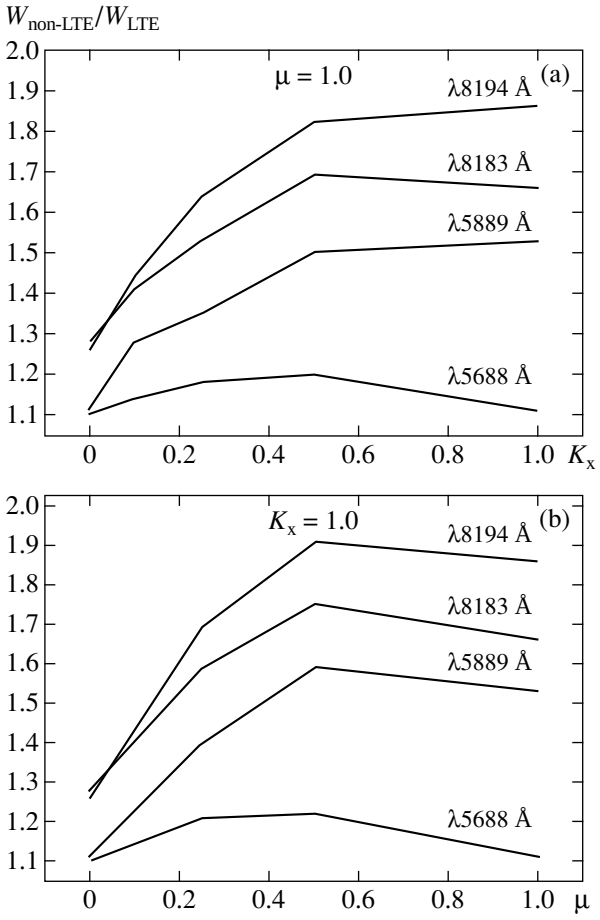

Fig. 4. Variations of non-LTE corrections $\Delta = W_{\text{non-LTE}}/W_{\text{LTE}}$ for different Na I lines with intensity of external radiation K_x (a) and with cosine of the angle of incidence μ (b) for a model atmosphere with $T_{\text{eff}} = 6000$ K and $\log g = 4.0$.

However, opposite cases are possible where the ionization by external radiation is large, while the cooling function is small. Such cases are realized for elements in the main or next ionization stages, for which the absorption coefficient at the frequencies of maximum of the Planck function is small. For such elements, the emergence of overionization, i.e., the overpopulation of higher ionization stages relative to lower ones, is realistic. In cases with an extremely small cooling function, the overionization is very strong and is mainly limited

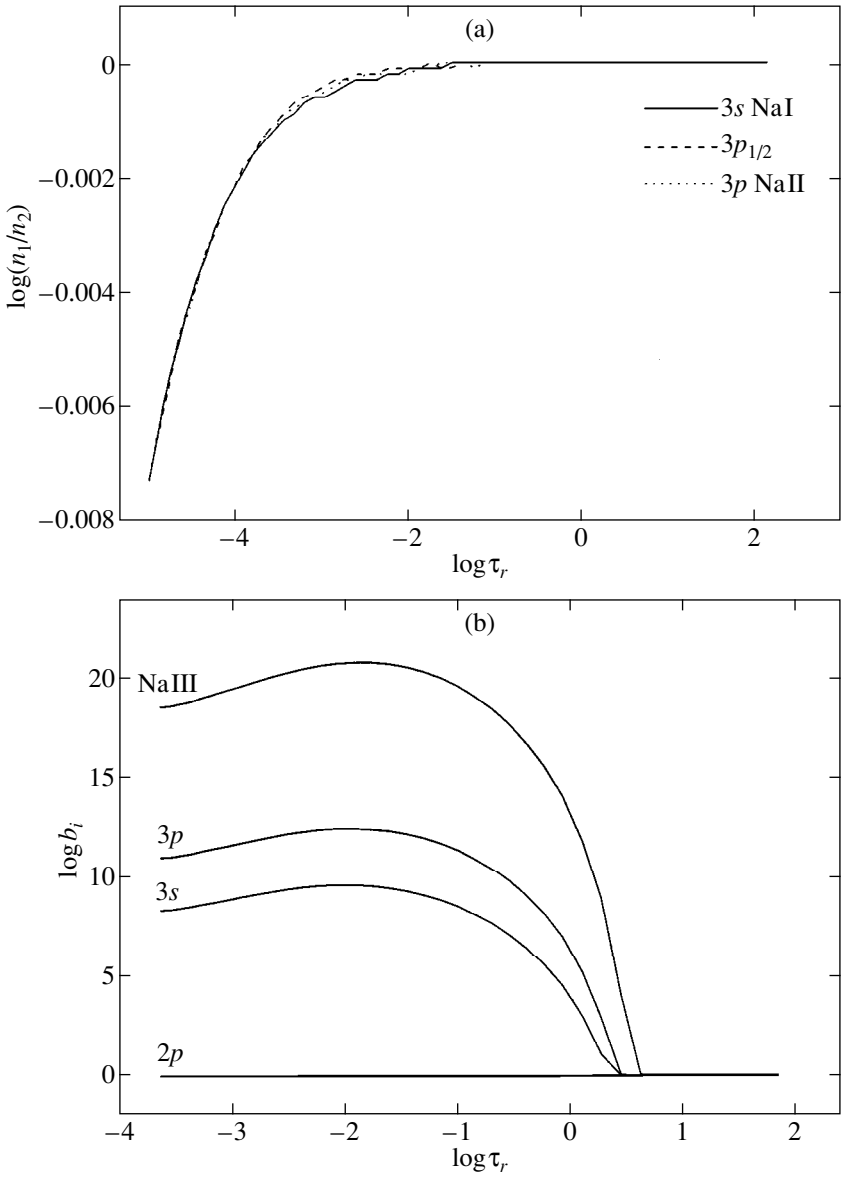

Fig. 5. (a) The ratio of the populations of Na I levels and Na II ground state for a model with $T_{\rm eff}$ = 6000 K, log g = 4.0, $K_{\rm x}$ = 1.00, and μ = 1.00 obtained with and without allowance for Na II/Na III ionization equilibrium. The distributions of b factors for Na II levels for a model atmosphere with $T_{\rm eff}$ = 5770 K, log g = 4.44, $K_{\rm x} = 10^{-8}$, and μ = 1.00 (b).

by the intensity of collisional processes. Non-LTE effects of this type, which were previously studied for atomic helium in the solar atmosphere [39, 40] and B stars [6], cause the He I ground state to be depopulated significantly. Since Na II and He I have similar ionization potentials and level structure, we additionally investigated the effect of statistical equilibrium in the Na II ion on Na I level populations.

We used a test 8-level Na I–Na II–Na III model to estimate possible non-LTE effects. Since this model is only an estimation one, we do not provide its detailed data. The model consisting of three Na I levels (3s, $3p_{1/2}$, $3p_{3/2}$), four Na II levels (2p, 3s 3s', 3p), and the Na III ground state (model 1) included six bound–bound and six bound–free transitions. In our calculations, we took into account the rates of all collisional and radiative transitions permitted in this model. In addition, we took into consideration additional ionization and recombination between excited Na I and Na II levels, as well as autoionization. To compare the results, we performed our calculations with the model (model 2) that included only three Na I levels and the Na II ground state.

Figure 5a shows the ratio of the populations of Na I 3s and $3p_{1/2}$ levels and Na II ground state obtained in the calculations with models 1 and 2 for a model atmosphere with $T_{\rm eff}$ = 6000 K, log$g$ = 4.0, $K_{\rm x}$ = 1.00, and μ = 1.00. The overionization of Na II proves to be strong enough to reduce the population of the Na II

state in the upper atmosphere by 1 or 2%. As a result, the populations of all Na I levels are reduced similarly. We detected no other effects of statistical equilibrium in the Na II system on Na I level populations, nor did we find any effects of Na I atomic structure on Na II level populations. Thus, the non-LTE effects for Na I and Na II level populations can be calculated separately. In addition, we concluded that Na II overionization during external illumination of moderate intensity ($K_x < 10.0$) weakens Na I overrecombination only slightly.

We also computed Na II level populations for Kurucz's solar model [22] with intensity of external irradiation $K_x = 10^{-8}$–10^{-10}, which corresponds to the solar coronal radiation. The results of our calculations of the *b* factors are shown in Fig. 5b. We see an enormous overpopulation of the Na III state and excited Na II levels down to the X-ray continuum formation depth. The absolute reduction in the populations of the Na II ground state does not exceed 10^{-9}; however, as we see from formula (2), the source function is proportional to the ratio of *b* factors for the upper and lower levels, and it increases by a factor of 10^5–10^7 for the Na II resonance lines. As a result, there must be two Na II resonance emission lines at $\lambda = 376$ and 372 Å. The $\lambda = 376$ Å line actually exists; we found it in the spectra of the quiet and active Sun [41]. The $\lambda = 372$ Å line is blended with the stronger Mg IX ($\lambda = 373$ Å) line and is unobservable. The $\lambda = 372$ Å emission line calculated in the LTE approximation with a solar model atmosphere that includes the chromosphere using data from [42] turns out to be weaker than the observed one by a factor of 70–90. Thus, the observed intensity of this line cannot be obtained with LTE models. The presence of the $\lambda = 376$ Å line in the solar spectrum proves the existence of non-LTE effects in the Na II atom produced by the coronal X-ray illumination and shows the need for such non-LTE calculations to describe the far-ultraviolet solar spectrum and to construct empirical model solar chromospheres. Note that the overpopulation of excited Na II levels does not lead to the formation of subordinate lines, because the populations of these levels remain very small.

CONCLUSION

Our results, which are useful in analyzing the spectra of close binary systems with illumination effects, are listed below.

(1) The departures from LTE for Na I are enhanced in X-ray illuminated atmospheres and their allowance seems necessary when computing synthetic spectra of close binary systems.

(2) In the X-ray illuminated atmospheres of late-type stars, the easily ionizable atoms with low ionization potentials (such as Na I) are in the state of extreme overrecombination caused by their small contribution to the total absorption coefficient in the hard spectral range. Non-LTE profiles of the cool and normal lines of such elements exhibit enhanced absorption cores and wings.

(3) The Na I line intensity depends weakly on the chromospheric temperature distribution and on the external-radiation parameters and is a good criterion for estimating the parameters of an unilluminated atmosphere. In addition, the Na I lines can be used to estimate the coefficient of reradiation of the external X-ray emission in continuum with $\lambda < 3000$ Å.

(4) The presence of external hard radiation gives rise to overionization for Na II and strong emission lines at $\lambda = 376$ and 372 Å. Na II overionization has a marginal effect on Na I level populations.

ACKNOWLEDGMENTS

We wish to thank A.M. Cherepashchuk, V.F. Suleĭmanov, and V.Ya. Shabert for comprehensive help with our studies. This study was supported by the Russian Foundation for Basic Research (project no. 96-02-16306-a). N.A. Sakhibullin is particularly grateful to the management of the Max Planck Institut fuer Astrophysik (Garching) and the International Program "Soros Professors," and V.V. Shimansky is grateful to the International Foundation for Basic Physics (Moscow) and the International Program "Soros Postgraduates."

REFERENCES

1. M. L. Alme and J. R. Wilson, Astrophys. J. **194**, 147 (1974).
2. M. Milgrom and E. E. Salpeter, Astrophys. J. **196**, 583 (1975).
3. M. Milgrom and E. E. Salpeter, Astrophys. J. **196**, 589 (1975).
4. R. A. London, R. McGray, and L. H. Auer, Astrophys. J. **243**, 970 (1981).
5. L. Anderson, Astrophys. J. **244**, 555 (1981).
6. A. S. Mitskevich and V. V. Tsymbal, Astron. Astrophys. **260**, 303 (1992).
7. D. Proga, S. J. Kenyon, J. C. Raymond, and J. Micolaewska, Preprint No. 4323 (Series of the Harvard–Smithsonian Center for Astrophysics, 1996).
8. N. A. Sakhibullin and V. V. Shimansky, Astron. Zh. **73**, 793 (1996).
9. N. A. Sakhibullin and V. V. Shimansky, Astron. Zh. **73**, 73 (1996).
10. N. A. Sakhibullin, Trudy Kazan Gos. Astron. Obs. **48**, 9 (1983).
11. N. A. Sakhibullin and V. V. Shimansky, Astron. Zh. **74**, 432 (1997).
12. R. L. Kurucz, Astrophys. J., Suppl. Ser. **40**, 1 (1979).
13. A. A. Boyarchuk, I. Hubeny, I. Kubat, *et al.*, Astrofizika **28**, 335 (1988).
14. N. A. Sakhibullin, Astron. Zh. **64**, 1269 (1987).
15. L. I. Mashonkina, N. A. Sakhibullin, and V. V. Shimansky, Astron. Zh. **70**, 372 (1993).

16. L. I. Mashonkina, N. N. Shimanskaya, and V. V. Shimansky, ASP Conf. Ser. **78**, 389 (1995).
17. L. I. Mashonkina, N. N. Shimanskaya, and V. V. Shimansky, Odessa Astron. Publ. **9**, 78 (1996).
18. D. V. Ivanova and V. V. Shimansky, Odessa Astron. Publ. **9**, 66 (1996).
19. T. Gehren, Astron. Astrophys. **38**, 289 (1975).
20. D. Hofsaess, At. Data Nucl. Data Tables **24**, 285 (1979).
21. J. H. Bruls, R. J. Rutten, and N. Shchukina, Astron. Astrophys. **265**, 237 (1992).
22. R. L. Kurucz, *SAO CD-ROMS, MA02138* (Cambridge, USA, 1994).
23. W. L. Wiese, M. W. Smith, and B. Miles, *Atomic Transition Probabilities, NSRDS–NBS Ref. Data Ser. 22* (Natl. Bur. Standards, Washington, 1967), Vol. 1.
24. R. L. Kurucz and E. Peytremann, SAO Spec. Rep., No. 362 (1975).
25. E. Biemont and N. Grevesse, At. Data Nucl. Data Tables **12**, 217 (1973).
26. A. A. Radtsig and B. M. Smirnov, *Parameters of Atoms and Atomic Ions* (Énergoatomizdat, Moscow, 1986).
27. H. van Regemorter, Astrophys. J. **132**, 906 (1962).
28. C. Park, J. Quant. Spectrosc. Radiat. Transf. **11**, 7 (1971).
29. J. I. Castor and H. Nussbaumer, Mon. Not. R. Astron. Soc. **155**, 293 (1972).
30. L. A. Vainshtein, I. I. Sobelman, and E. A. Yukov, *Atomic Excitation and Line Broadening* (Nauka, Moscow, 1979).
31. M. J. Seaton, Planet. Space Sci. **12**, 55 (1964).
32. W. Steenbock and H. Holweger, Astron. Astrophys. **130**, 319 (1984).
33. D. G. Yakovlev, L. M. Band, M. B. Trzhaskovskaya, and D. A. Verner, Astron. Astrophys. **237**, 267 (1990).
34. W. Fullerton and C. W. Cowley, Astrophys. J. **165**, 643 (1971).
35. A. McWilliam and G. W. Preston, Astron. J. **109**, 2757 (1995).
36. L. H. Auer and J. Heasley, Astrophys. J. **205**, 165 (1976).
37. R. L. Kurucz, SAO Spec. Rep., No. 309, 1 (1970).
38. Y. Takeda and M. Takada-Hidai, Publ. Astron. Soc. Jpn. **46**, 395 (1994).
39. R. W. Milkey, J. N. Heasley, and H. A. Beebe, Astrophys. J. **186**, 1043 (1973).
40. S. H. Avrett, J. E. Vernazza, and J. L. Linsky, Astrophys. J. Lett. **207**, L199 (1976).
41. J. E. Vernazza and E. M. Reeves, Astrophys. J., Suppl. Ser. **37**, 485 (1978).
42. P. Maltby, E. H. Avrett, M. Carlsson, *et al.*, Astrophys. J. **306**, 284 (1986).

Translated by V. Astakhov

Astronomy Letters, Vol. 26, No. 5, 2000, pp. 319–321. Translated from Pis'ma v Astronomicheskiĭ Zhurnal, Vol. 26, No. 5, 2000, pp. 380–383.

Linear Polarization of Precataclysmic Variables

N. F. Voĭkhanskaya*

Special Astrophysical Observatory, Russian Academy of Sciences, Nizhniĭ Arkhyz, 357147 Russia

Received April 5, 1998; in final form, September 27, 1999

Abstract—The optical linear polarization of three precataclysmic variables was measured in *B* and *R*. A noticeable polarization was detected only in BD +50°2869. In the other two cases, the polarization is probably interstellar in origin. © *2000 MAIK "Nauka/Interperiodica".*

Key words: *stars—variable and peculiar*

INTRODUCTION

Precataclysmic variables are detached binary systems with periods from several hours to several days, which consist of a white dwarf or a hot subdwarf and a low-mass unevolved companion of a late spectral type. Such systems are formed during evolution in the common envelope that is produced when the more massive component of the original wide pair becomes a red giant and swallows up its low-mass companion. At this stage, the system loses large amounts of mass and orbital angular momentum to become a close, though still detached binary. A study of the properties of precataclysmic binaries undistorted by the sources of accretion luminosity gives an idea of the components of cataclysmic variables. Their properties are difficult, and occasionally even impossible, to determine directly from observations. In particular, it is not yet known for sure whether the components of cataclysmic variables possess magnetic fields and what is the field strength. To obtain information about magnetic fields of the components, we started polarization measurements for precataclysmic variables. Here, we report the results for three variables: BD +50°2869, BD +26°2405, and V471 Tau.

BD +50°2869 (HD 186924, SAO 31951) is located at the center of the planetary nebula NGC 6826 (PK 83+12.1). Its spectral type is O3f. Its brightness variability was discovered by Kazaryan [1]. Its binary nature was established by Noskova [2], who obtained the radial-velocity curve using He II absorption lines and found the system's period to be $0^{d}.2384$. Becker *et al.* [3] constructed a spatial kinematic model of the nebula. It follows from this model that the envelope ejection probably occurred in two stages and has continued up until now in the form of a bipolar wind. The P Cyg profiles of some ultraviolet lines suggest a continuing mass outflow [4].

Polarization measurements were carried out by Rudnikova [5] and Hamilton and Liller [6]. Rudnikova measured photographic images of the nebula in a band close to *V* and obtained a linear polarization of $(8.7 \pm 1.9)\%$. Hamilton and Liller performed their measurements with a two-channel photoelectric polarimeter in *UBV*. Since these authors did not publish the size of their entrance aperture, the ratio of fluxes from the nucleus and the nebula is difficult to estimate. As for most other studied planetary nebula, no linear polarization was found for NGC 6826: $\bar{P} = (0.2 \pm 0.1)\%$. The authors assume the polarization to be interstellar.

The star **BD +26°2405** (HD 112313, SAO 82570, IN Com) lies at the center of the planetary nebula LoTr 5 (PK 339+88.1). Its spectral type is G5 III. Since such a star cannot excite the nebula, it was assumed to have a hot faint companion. This companion was discovered by Feibelman and Kaler [7] during IUE observations. The subdwarf's temperature was found to be $\approx 2 \times 10^5$ K, with the bolometric luminosity being no lower than that of a G giant. This implies that it is one of the hottest known stars in the Galaxy, as was confirmed by Fruscione *et al.* [8] during EUVE observations. Optically, however, the dwarf is 6^{m} fainter than a G star. As a result, a possible eclipse would be unobservable, though we can hope to see a reflection effect.

Photoelectric *UBV* photometry of the star was performed by Schnell and Purgathofer [9], Noskova [10], and Malasan *et al.* [11]. They revealed modest brightness variability, which results from reflection in the binary system. In addition, the authors of each paper obtained four or five significant periods, and as yet no unambiguous choice has been made between them. Spectroscopic studies [11, 12–14] did not clarify the situation. The authors of each paper obtained several periods that differed from one another and from photometric periods. Furthermore, the system was assumed to be triple.

* E-mail address for contacts: adm@sao.ru

1063-7737/00/2605-0319$20.00 © 2000 MAIK "Nauka/Interperiodica"

Thus, the result of the above studies was the conclusion that the light and radial-velocity curves varied with time, the assurance that the central star in LoTr 5 was a multiple system, and the complete failure to determine the period.

V471 Tau (BD +16°516) is an eclipsing binary system consisting of two DA2 and K2 V dwarfs. This is a precataclysmic variable that has already passed the common-envelope stage, but active mass transfer has not yet started. Mullan *et al.* [15, 16] detected a fast cold wind from the red dwarf with $\dot{M} \geq 2 \times 10^{-11}\ M_\odot\ \mathrm{yr}^{-1}$. However, only a small fraction of the wind ($<10^{-4}\ \dot{M}$) is accreted by the white dwarf. Such a low accretion rate is attributable to counteraction of the white dwarf's rapidly rotating magnetosphere. The presence of a significant magnetic field is confirmed by the fact that nonthermal radio emission was detected from V471 Tau [17, 18]. Both a quiet emission component, which varied synchronously with the optical light curve, and sporadic flares were observed. The light from the latter is polarized by 50%, on the average.

The polarization of the star's optical light was measured only once by Kemp and Rudy [19]. The period-averaged linear polarization was $\bar{P} = (0.15 \pm 0.1)\%$, $\bar{\Theta} = 50° + 15°$. Variations of $\bar{P}$ during the period were within the limits of the measurement errors, whereas the position of the polarization plane varied. The authors believe the observed polarization to be interstellar, in agreement with the distance to the Hyades to which the star belongs.

OBSERVATIONS AND RESULTS

Our observations were carried out in 1994–1995 with the two-channel photoelectric polarimeter designed by Efremov and Naidenov [20] that was mounted at the Cassegrain focus of the Zeiss-1000 telescope. We used a circular 10″ aperture, within which the central star and the central part of the nebula fell. The signal integration time for a single measurement ranged from 1 to 10 s, depending on object brightness and observing conditions. The measurements were made simultaneously in *B* and *R*. The background was measured with the same aperture before and after each object. To reduce the observations from the instrumental system to the system corresponding to the true polarization parameters, on each night we observed standard stars with well-known true polarization parameters and stars with zero polarization from the lists by Serkowski [21], Hsu and Breger [22], Berdyugin and Shakhovskoĭ [23]. They were chosen as close to the program objects as possible. A weight that generally corresponded to the time of observation was assigned to each observation. Usually, the remaining conditions were kept constant during a single set of observations. Whenever possible, we combined and averaged individual observations to improve the accuracy. All equations were solved by the least-squares method. As a result, we obtained mean parameters $\bar{u}$ and $\bar{q}$, along with their mean errors estimated from dispersions of the parameters. Using standard formulas, we then calculated the mean degree of linear polarization $\bar{P}$, the mean position angle $\bar{\Theta}$, and their errors. The data reduction technique is detailed in [24].

When reducing the observations of **BD +50°2869,** we used the period published by Noskova [2]. An attempt to present the results with this period failed: neither brightness nor polarization parameters showed periodic variations. The period may be insufficiently accurate, but it is possible that here the problem with multiple periods is the same as that for BD +26°2405. Having averaged the results in interval $0.1P$ (34.3 min), we found that the degree of polarization in *B* changed within a night from 2.69 to 7.08%, and the position angle changed from 5° to 160°. The changes in *R* are smaller: the degree of polarization and the position angle changed from 2.55 to 4.57% and from 2° to 170°, respectively. The means of our measurements are

$$\bar{P} = (3.00 \pm 0.05)\%,\ \bar{\Theta} = 72.4° \pm 0.5°\ \text{in } B,$$

$$\bar{P} = (2.64 \pm 0.23)\%,\ \bar{\Theta} = 7° \pm 1°\ \text{in } R.$$

The results of our measurements are intermediate between those of Rudnikova [5] and Hamilton and Liller [6]. This may be explained by a different contribution of the nebula to the recorded radiation. However, if the changes are real, this implies variability of the central star, not only of its brightness but also of the rate of mass outflow, and maybe of the surface magnetic field.

No linear polarization was detected in **BD +26°2405** within the error limits, although the position angle varied. The means of all our estimates are

$$\bar{P} = (0.17 \pm 0.11)\%\ \text{in } B,$$

$$\bar{P} = (0.31 \pm 0.15)\%\ \text{in } R.$$

For **V471 Tau**, all measurements were made outside eclipse, but on both sides of it. No polarization was detected, within the limits of the measurement errors. We failed to record any significant variations neither inside the cycle nor between cycles. The means of our measurements are

$$\bar{P} = (0.13 \pm 0.05)\%\ \text{in } B,$$

$$\bar{P} = (0.10 \pm 0.17)\%\ \text{in } R.$$

This result is in good agreement with that of Kemp and Rudy [19].

The results of our polarization measurements are summarized in the table.

The calculations by Wood *et al.* [25, 26] show that multiple Thomson scattering in axisymmetric envelopes causes the polarization to increase to 4% or more.

Polarization measurements

P, %	Θ, deg	Band	Reference
BD +50°2869			
8.7 ± 1.9		*V*	[5]
0.15 ± 0.15		*U*	[6]
0.15 ± 0.06		*B*	[6]
0.4 ± 0.1		*V*	[6]
3.00 ± 0.05	72.4 ± 0.5	*B*	This paper
2.64 ± 0.23	7 ± 1	*R*	This paper
BD +26°2405			
0.17 ± 0.11		*B*	This paper
0.31 ± 0.15		*R*	This paper
V471 Tau			
0.15 ± 0.1	50 ± 15	*U* + *B*	[19]
0.13 ± 0.05		*B*	This paper
0.10 ± 0.17		*R*	This paper

At the same time, at significant absorption in the medium, the degree of polarization decreases and can reach zero.

BD +50°2869 is surrounded by a transparent nebula with a clearly distinguishable structure. It is already at the end of the common-envelope stage or has just emerged from it. This is the case where scattering produces significant polarization of light. In addition, the IRAS satellite detected a noticeable infrared radiation from it, which may suggest the presence of dust in its outer layers. Multiple Rayleigh scattering by dust grains also causes the degree of polarization to increase.

BD +26°2405 is surrounded by a fairly dense nebula. It is going through the common-envelope stage. No infrared emission was recorded from it. Absorption and reradiation must therefore depolarize the emergent emission.

Since the envelope of V471 Tau has long been dispersed, no polarization is observed. The components' intrinsic magnetic fields are not strong enough for the synchrotron radiation mechanism to start working.

ACKNOWLEDGMENTS

I am grateful to I.D. Naidenov for assistance in the observations.

REFERENCES

1. M. A. Kazaryan, Soobshch. Byurakan Obs., No. 39, 45 (1968).
2. R. I. Noskova, Astron. Tsirk., No. 1128, 1 (1980).
3. I. Becker, F. Gieseking, and J. Solf, Mitteil. Astron. Gesellschaft **62**, 253 (1984).
4. W. A. Feibelman and F. C. Bruhweiler, Astrophys. J. **357**, 548 (1990).
5. K. G. Rudnikova, Vestnik Kiev Univ. (Ser. Astron.), No. 6, 9 (1964).
6. N. Hamilton and W. Liller, Mem. Soc. R. Sci. de Liege, 6-e Ser. **5**, 213 (1973).
7. W. A. Feibelman and J. B. Kaler, Astrophys. J. **269**, 592 (1983).
8. A. Fruscione, J. J. Drake, K. McDonald, and R. F. Malina, Astrophys. J. **441**, 726 (1995).
9. A. Schnell and A. Purgathofer, Astron. Astrophys. **127**, L5 (1983).
10. R. I. Noskova, Pis'ma Astron. Zh. **15**, 346 (1989) [Sov. Astron. Lett. **15**, 149 (1989)].
11. H. L. Malasan, A. Yamasaki, and M. Kondo, Astron. J. **101**, 2131 (1991).
12. A. Acker, G. Jasniewicz, and F. Gleizes, Astron. Astrophys. **151**, L13 (1985).
13. G. Jasniewicz, A. Duquennoy, and A. Acker, Astron. Astrophys. **180**, 145 (1987).
14. G. Jasniewicz, A. Acker, N. Mauron, *et al.*, Astron. Astrophys. **286**, 211 (1994).
15. D. J. Mullan, E. M. Sion, F. C. Bruhweiler, and F. G. Carpenter, Astrophys. J. Lett. **339**, L33 (1989).
16. D. J. Mullan, H. L. Shipman, E. M. Sion, and J. MacDonald, Astrophys. J. **374**, 707 (1991).
17. J. Patterson, J. P. Caillault, and D. R. Skillman, Publ. Astron. Soc. Pac. **105**, 848 (1993).
18. J. Lim, S. M. White, and S. L. Cully, Astrophys. J. **461**, 1009 (1996).
19. J. C. Kemp and R. J. Rudy, Publ. Astron. Soc. Pac. **87**, 301 (1975).
20. V. G. Efremov, I. D. Naidenov, Otchety Spets. Astrofiz. Obs. (1991).
21. K. Serkowski, in *Planets, Stars and Nebulae Studied with Photopolarimetry*, Ed. by T. Gehrels (1974), p. 135.
22. J.- C. Hsu and M. Breger, Astrophys. J. **262**, 732 (1982).
23. A. V. Berdyugin and N. M. Shakhovskoĭ, Izv. Krym. Astrofiz. Obs. **87**, 122 (1993).
24. N. M. Shakhovskoĭ and Yu. S. Efimov, Izv. Krym. Astrofiz. Obs. **45**, 90 (1972).
25. K. Wood, J. E. Bjorkman, B. A. Whitney, and A. D. Code, Astrophys. J. **461**, 828 (1996).
26. K. Wood, J. E. Bjorkman, B. A. Whitney, and A. O. Code, Astrophys. J. **461**, 847 (1996).

Translated by N. Samus'

Astronomy Letters, Vol. 26, No. 5, 2000, pp. 322–327. Translated from Pis'ma v Astronomicheskiĭ Zhurnal, Vol. 26, No. 5, 2000, pp. 384–390.

Prominence Height and Vertical Gradient in Magnetic Field

B. P. Filippov* and O. G. Den

Institute of Terrestrial Magnetism, Ionosphere, and Radiowave Propagation, Russian Academy of Sciences, Troitsk, 142092 Russia

Received April 13, 1999; in final form, September 27, 1999

Abstract—The existence of a critical height for quiescent prominences and its relationship to parameters of the magnetic field of photospheric sources are discussed. In the inverse-polarity model, stable equilibrium of a filament with a current is possible only in the region where the external field decreases with height no faster than ~1/*h*. Calculations of the potential magnetic field above the polarity-inversion line are compared with the observed prominence height. The prominence height is shown to actually depend on the vertical field gradient and does not exceed the level at which the exponent of field decrease is equal to unity. *© 2000 MAIK "Nauka/Interperiodica".*

Key words: *plasma astrophysics, hydrodynamics and shock waves, Sun*

INTRODUCTION

Any bright structures visible in chromospheric lines (such as Hα or Ca II K) and rising above the solar limb are popularly known as solar prominences. They differ from the surrounding coronal matter by a higher density and a lower temperature. Some of them represent dynamic phenomena (surges, sprays, loops) with lifetimes of minutes or hours, while others are stationary structures persisting for many months. The latter are generally seen on the disk in absorption as dark filaments. Here, we deal with long-lived stable prominences and assume the terms *filament* and *prominence* to be synonyms. In their turn, the filaments are also subdivided into two classes: quiescent, larger but loose filaments observed outside active regions and more compact, dense filaments of active regions.

The prominences of active regions barely protrude above the average chromospheric level. Their heights usually do not exceed 10 Mm [1, 2]. The quiescent prominences reach considerably larger heights, up to 200 Mm [3, 4]. The sizes and heights of quiescent prominences increase during their lifetimes. The height at an early stage is 15–30 Mm, a well-developed filament in the middle phase is at a height of ~50 Mm, and the oldest prominences rise by 60–200 Mm above the limb [5]. Prominences appear at large heights only in the dynamic phase, during eruption.

The total number of prominences exponentially decreases with increasing height in the range 10–100 Mm [6]. Obashev [7] found the height distribution of all prominences to be similar in shape to Pearson's distribution peaking at a height of 30 Mm. This author found no dependence of the most commonly encountered (median) prominence height on solar-cycle phase from 1955 until 1957, at least in the heliographic-latitude range 20°–60°, and on latitude (if the polar regions are excluded). The lack of such dependence was also noted by Dermendzhiev [8] for 1945–1965. Variation in the yearly mean prominence height with solar cycle was revealed by Cantu *et al.* [9] and subsequently confirmed by Makarov [10] using the 1912–1974 data of the Kodaikanal Indian Observatory. The maximum prominence height is reached near maximum activity or two years earlier. In addition, a systematic increase in the mean prominence height from 25 to 33 Mm for the period under consideration was noted.

Kim *et al.* [11, 12] also found a dependence of the mean prominence height on cycle phase for the second half of solar cycle 21, which generally matches the dependence obtained by Makarov. They noted the presence of two peaks in the height distribution of prominences, at 18 and 33 Mm, and surmised that the lack of dependence of the median height on cycle phase could be due its bimodal structure. Having distinguished only high-latitude prominences, which constitute an almost continuous polar corona around the polar caps, Makarov *et al.* [13] found that, as the global neutral line drifts poleward, the prominence height above it decreases by more than a factor of 2.

The cool dense matter of prominences is generally recognized to be kept in the corona from falling into the chromosphere by a magnetic field (see, e.g., [14]). The field properties must determine the equilibrium conditions for filaments and, in particular, their heights. Attempts to consider the prominence height as a kind of a magnetic characteristic [15, 16] are therefore not

* E-mail address for contacts: bfilip@izmiran.troitsk.ru

1063-7737/00/2605-0322$20.00 © 2000 MAIK "Nauka/Interperiodica"

accidental, although there is currently no clear understanding of the physical relationship. For instance, it is suggested that the prominence height characterizes the background magnetic field strength [13] or that the height distribution of prominences is related to the distribution of the horizontal gradient in longitudinal magnetic field near the polarity-inversion line [17]. The latter authors found gradients of 2–10 G Mm^{-1} to correspond to most cases of the existence of filaments above the polarity-inversion line in December 1982. No quiescent filaments were observed for gradients exceeding 20 G Mm^{-1}. The existence of a critical transverse gradient in vertical field was also noted in several other studies [18–20], although the gradient values differ, being in the range 7–28 G Mm^{-1}. Maksimov and Prokop'ev [20] partly attribute the discrepancies to the different spatial resolutions of magnetograms.

The above studies contain no indications of the physical mechanism that relates the equilibrium conditions of filaments to the magnetic-field parameters. Here, we try to elucidate this relationship and to establish the physical reasons for the existence of critical values by testing the conclusions drawn from examples of specific calculations of the magnetic fields of photospheric sources above the polarity-inversion lines.

EQUILIBRIUM OF FILAMENTS IN A MAGNETIC FIELD

Two types of magnetic support of filaments above the chromospheric surface are distinguished. In the first one, represented by Kippenhahn–Schluter's model [21], the Lorentz force with which the field of photospheric sources interacts with the filament current is directed upward and balances the force of gravity. In the second one, represented by Kuperus–Raadu's model [22], the field of photospheric sources presses the filament current against the photosphere, and the supporting force is repulsion of the current from the surface currents induced by it in the photosphere. These two types of filament equilibrium differ not only by the directions of the currents but also by their relative magnitudes. In the former case, the current disturbs the background field only slightly, so the field inside the prominence is mainly determined by photospheric sources. For equilibrium of the second type, the field of the current dominates inside the filament and at a distance from it comparable to the prominence height above the chromosphere. Since the direction of the field inside the prominence can differ considerably from the background one and can even be opposite to it, such models were called inverse-polarity models, while modifications of Kippenhahn–Schluter's model were termed normal-polarity models.

The existence of a critical height for prominences or a critical gradient cannot be explained in terms of Kippenhahn–Schluter's classical model. As was shown by Anzer [23], the plasma equilibrium in this model is stable for vertical displacements, provided that the current density decreases with height in a vertical unbounded layer

$$\frac{dj^2}{dh} < 0, \tag{1}$$

and for horizontal displacements, provided that the field grows with height

$$\frac{dB}{dh} > 0. \tag{2}$$

In a current-free field, the condition (2) means that the field lines have a geometry with upward curvature. Since all sources of the field lie beneath the photosphere, the condition (2) can be satisfied only in a bounded region near the zero point. There is such a geometry, for example, in a quadrupole configuration, which is often invoked as the probable magnetic "skeleton" of the prominence [24–26].

The finiteness of the region where the inequality (2) is satisfied is inconsistent with the assumption that the layer is unbounded in height, which is used to derive the condition (1) of vertical stability. It can be easily shown that the horizontal and vertical stabilities require conflicting conditions. Indeed, for the filament as a whole, the vertical equilibrium implies that

$$F = \frac{I}{c}B(h_0) - mg = 0, \tag{3}$$

where I is the filament current, h_0 is the height of the filament equilibrium position above the photosphere, $B(h)$ is the magnetic field of photospheric sources, and m is the mass per unit length of the filament. The equilibrium is known to be stable if the second derivative of potential energy is positive,

$$\left.\frac{d^2W}{dh^2}\right|_{h_0} = -\left.\frac{dF}{dh}\right|_{h_0} > 0. \tag{4}$$

Substituting (3) in (4) and taking into account the fact that g = const on the scale of the vertical prominence extent, we obtain

$$\frac{dB}{dh} < 0, \tag{5}$$

which is in conflict with the condition (2) of horizontal stability.

In the simple two-dimensional inverse-polarity model, the force acting in the vertical direction per unit length of the filament is

$$F = \frac{I^2}{c^2h} - \frac{I}{c}B(h) - mg, \tag{6}$$

where the first term corresponds to the interaction of the filament current with the currents induced in the photosphere. If the filament weight is disregarded, the equilibrium is achieved at height h_0 determined from the equation

$$\frac{I}{ch_0} = B(h_0). \quad (7)$$

The horizontal stability in the inverse-polarity model requires that the relation opposite to (2) be satisfied, which is naturally satisfied for a dipole field. The condition of vertical stability follows from substitution of (6) and (7) in (4):

$$\left.\frac{dB}{dh}\right|_{h_0} > -\frac{B(h_0)}{h_0}. \quad (8)$$

Hence, the filament equilibrium is stable if the vertical gradient in external field lies in the range

$$-\frac{B(h_0)}{h_0} < \left.\frac{dB}{dh}\right|_{h_0} < 0. \quad (9)$$

If the change of the magnetic field in some range of heights is described by a power-law function

$$B(h) = Ch^{-\alpha}, \quad (10)$$

then we find from (8) that

$$\alpha < 1. \quad (11)$$

Thus, for the equilibrium to be stable, the external field in the vicinity of the filament must decrease with height no faster than ~1/*h*. This is a result of the height dependence of the magnetic field of the "mirror" current, as suggested by Van Tend and Kuperus [27]. If, beginning from some height h_c, the field falls off faster than ~1/*h*, then this height is the critical one for quiescent filaments. In models in which the external field is simulated by a linear dipole, the critical height corresponds to the depth at which the dipole lies beneath the photosphere [28, 29].

Thus, in the inverse-polarity models of filament equilibrium, the critical height of prominences depends on magnetic-field parameters, though not on the field strength and not on the horizontal derivative, as was assumed by some authors, but on the vertical derivative. To test the validity of this conclusion for actual solar prominences, it is necessary to calculate the magnetic field above the polarity-inversion line and to compare the critical height obtained from these calculations with the heights of observed prominences. The difficulties of such a comparison are clear even from the fact that the times of measurements of the prominence height at the limb and of the magnetic field near the central meridian are separated by a week. Nevertheless, we made such an attempt by assuming that the magnetic field near quiescent filaments did not change too much in this interval.

THE DATA

For our purposes, we need magnetic-field data with a sufficiently high spatial resolution (no worse than 5″, because it is necessary to reveal a functional height dependence of the field in the range of observed prominence heights) and with a high sensitivity, because the photospheric fields near quiescent filaments outside active regions are weak. We used MDI magnetograms of the SOHO Space Observatory, which are accessible via Internet at http://sohodb.nascom.nasa.gov/summary/. The calibration step wedge on each magnetogram allows the field strength to be measured at any point with an acceptable accuracy. As for the sensitivity of this magnetograph, it turns out to be insufficient for high-latitude regions; therefore, we had to restrict ourselves to low-latitude filaments in regions with a sufficiently strong field.

We determined the filament positions and the prominence heights from Hα filtergrams of the Big Bear Observatory and Ca II K_3 spectroheliograms of the Meudon Observatory, available at http://sohodb.nascom.nasa.gov/synoptic/gif/.

We chose several filaments observed in May, November, and December 1998, whose heights differed markedly.

THE METHOD OF CALCULATIONS

The current-free magnetic field in the corona can be calculated by solving the Neumann external boundary-value problem. Although the field of the filament current is not weak compared to the field of the subphotospheric currents, it can be readily separated from the latter. In the inverse-polarity model, the effect of the induction currents on the photospheric surface reduces to neutralizing the normal field component of the filament current on this surface, implying that the field of the filament does not penetrate beneath the photosphere. For this reason, the measured normal field component in the photosphere is entirely determined by the field of the subphotospheric sources and can be used to calculate its potential extension into the corona.

Since we are concerned with the magnetic field at the prominence height, which is small compared to the solar radius, we may neglect sphericity and use the well-known solution for half-space with a plane boundary (see, e.g., [30], p. 363)

$$\mathbf{B} = \frac{1}{2\pi}\int\!\!\int_S \frac{B_n(x', y', 0)\mathbf{r}}{r^3}dx'dy', \quad (12)$$

where $B_n(x', y', 0)$ is the normal magnetic-field component on plane *S* and **r** is the radius vector from some point on the surface to a given point in the corona. Actual measurements of the solar magnetic field yield the mean line-of-sight component on some area, whose size is determined by the magnetograph resolution. Within this small rectangular area, the integrals in (12) can be calculated analytically [31], and the field at a given point can be calculated by adding up the contributions of all areas on the plane. Cutting out a rectangular region around the filament under study from the

magnetogram of the full disk, we disregard the contribution of the areas outside it. This is justified if the region size is much larger than the filament height or if the main sources of the field (active regions) lie within the cut-out region. In practice, the region sizes were of the order of $10' \times 10'$. Since the side of such a square corresponds to 160 pixels on the MDI magnetogram, we performed averaging over 3–5 adjacent pixels to reduce the data set. As usual, the line-of-sight component was taken as the normal one, which gives an error mainly at the edges of the region.

For the equilibrium conditions, of importance is the field component perpendicular to the polarity-inversion line. Since the total vector in a current-free field is generally orthogonal to the polarity-inversion line, we took the magnitude of the horizontal field as the sought-for quantity in order not to determine the direction of the neutral line at each level. To calculate the local index α, we used the expressions obtained by differentiating (10) with respect to h

$$\alpha = -\frac{h}{B}\frac{dB}{dh} = -\frac{d(\ln B)}{d(\ln h)}. \quad (13)$$

To increase the significance, we took a mean of the three values determined for the center of the polarity-inversion line and with a shift of ±10% of the region size along it as α.

RESULTS

Figure 1 shows the magnetogram of the central part of the northern solar hemisphere for May 16, 1998, obtained by the MDI instrument on SOHO. The contour indicates the filament location from the Big Bear Observatory filtergram. This is a typical quiescent filament located between two active regions. There is the sunspot group NOAA 8222 in the eastern part (on the left) and the remnants of a decayed group, in which no sunspots are seen, in the western part (on the right). The polarity-inversion line is inclined to the meridian at an angle of 30° counterclockwise; its location in the central part changes with height only slightly (Fig. 2). Figure 3 shows changes of the magnetic field strength with height above the polarity-inversion line, with which the filament is associated, on a double logarithmic scale. The slope of the curve steepens with height, and, accordingly, the index of the locally fitting power-law function (dashed curve) increases. The height h_c at which the index is equal to unity is 58 Mm; the prominence height at the eastern solar limb on May 9, 1998, was 50 Mm. This value is lower than the critical one, although fairly close to it. Note that this well-developed filament suddenly disappeared on May 19, apparently exceeding the stability threshold.

In Fig. 4, critical height h_c of stable filament equilibrium is plotted versus observed prominence height h_p above the limb. The dashed line corresponding to equality of these quantities must be the upper boundary

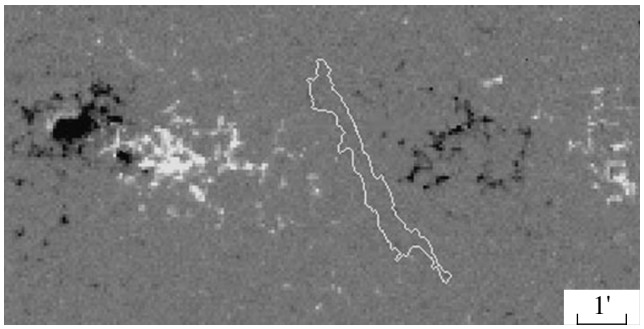

Fig. 1. The MDI/SOHO magnetogram of the central part of the northern solar hemisphere for May 16, 1998. The contour indicates the filament location from the Big Bear Observatory filtergram. (Courtesy of the SOHO MDI Consortium; SOHO is a joint ESA–NASA program.)

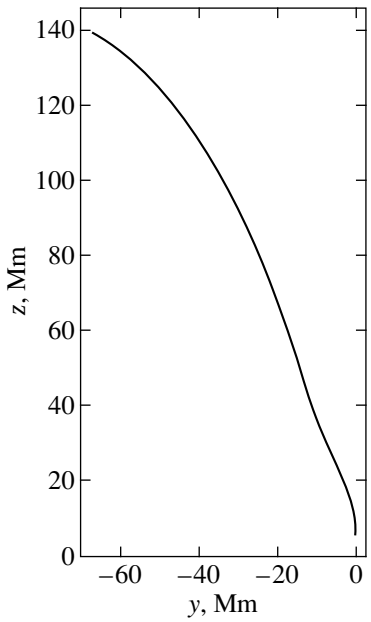

Fig. 2. The section of the $B_z = 0$ surface by the x = const plane passing through the center of the region under study, showing the displacement of the polarity-inversion line with height.

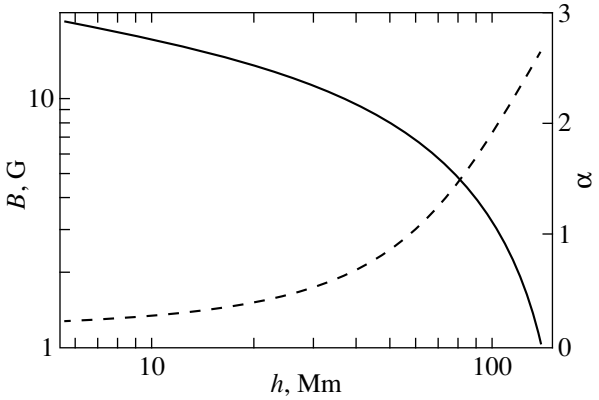

Fig. 3. Magnetic field strength on the polarity-inversion line versus height. The dashed line indicates variations in local index α.

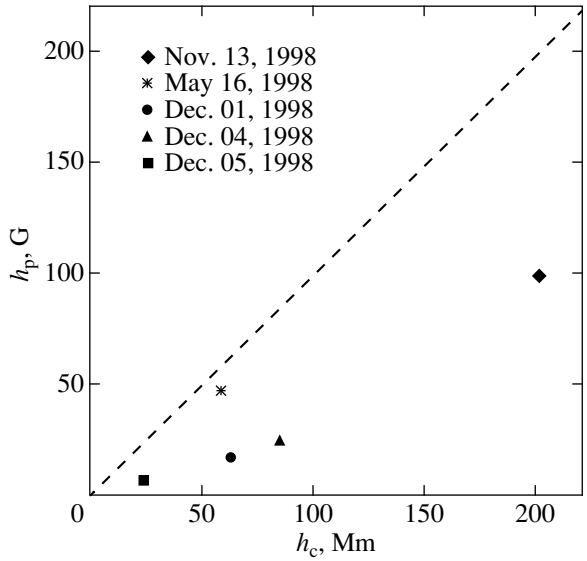

Fig. 4. Critical height of stable filament equilibrium h_c versus observed prominence height above the limb h_p. The dashed line corresponding to equality of these quantities is the stability boundary.

of the distribution. All points are seen to actually lie below this line. The distance from the point to the line characterizes the filament stability margin. It is the smallest for the May filament, which disappeared three days after it crossed the central meridian. The remaining filaments safely vanished behind the western limb, and three of them were reliably identified during the next rotation.

Thus, the above comparison lends support to the idea that the critical prominence height is determined by the height dependence of the external magnetic field. How can we interpret in this connection the data on the existence of a critical horizontal gradient mentioned in the Introduction? We first note that, in a plane current-free field with a translational symmetry along the x axis [$\mathbf{B} = \{0, B_y(y, z), B_z(y, z)\}$],

$$\frac{\partial B_y}{\partial z} = \frac{\partial B_z}{\partial y}. \quad (14)$$

In addition, the fact should be taken into account that the vertical gradient $\partial B_y/\partial z$, which determines the stability, at the prominence height must be known, whereas the horizontal gradient is measured at the photospheric level. As was already noted above, the critical prominence height for a linear dipole is equal to the depth at which the dipole lies beneath the photosphere. Hence, the z coordinate changes by a factor of 2, while the magnitude of the gradient changes by this factor cubed, i.e., eightfold. Using the inequality (8), for a height of 30 Mm and a field of 25 G typical of quiescent prominences [32], we obtain

$$\frac{\partial B_z}{\partial y} < 7 \text{ G Mm}^{-1}. \quad (15)$$

This value corresponds to the lower boundary of the measured critical values. Decreasing the height will increase it. For large gradients, the critical height becomes very small, and, probably, a detectable filament cannot form.

CONCLUSION

We have analyzed the prominence height above the limb. Some authors propose to consider its value as a characteristic of the coronal magnetic field. Remarkably, there are some preferred prominence height and a height above which no quiescent prominences are observed. In currently available models, the prominences can be in equilibrium in principle at any height. Kippenhahn–Schluter's classical model assumes that the prominence is unbounded in extent. Limiting the vertical size results in conflicting horizontal and vertical stability conditions. In the inverse-polarity model, the critical height of stable equilibrium is determined by the spatial characteristic of the magnetic field of photospheric sources. A comparison of the observed prominence height with the calculated coronal magnetic field shows that all of them are within the stability limits of the inverse-polarity model. In this model, the prominence height depends on the magnitude of the electric current flowing in the filament and increases with current. However, the critical height depends only on the properties of the external field; therefore, if the filament current steadily increases, the filament will inevitably reach the critical height, and eruption will follow. Thus, having data on the vertical magnetic-field component, we can estimate the eruption probability of a prominence by comparing its height above the limb with the critical height of stable equilibrium obtained from magnetic-field calculations.

ACKNOWLEDGMENTS

We are grateful to the staffs of the MDI SOHO mission and the Big Bear and Meudon Observatories, who made the observational data accessible via Internet. This study was supported by the State Science and Technology Program "Astronomy."

REFERENCES

1. B. Schmieder, in *Dynamics and Structure of Solar Prominences*, Ed. by J. L. Ballester and E. R. Priest (Universitat de les Illes Balears, 1987), p. 5.
2. B. Schmieder, in *Dynamics and Structure of Quiescent Solar Prominences*, Ed. by E. R. Priest (Kluwer, Dordrecht, 1989), p. 15.
3. E. Pettit, Astrophys. J. **76**, 9 (1932).
4. M. D'Azambuja *et al.*, Ann. Obs. Paris, Meudon **6**, Fasc. VII (1948).
5. B. Rompolt, Hvar Observ. Bull. **14**, 37 (1990).
6. R. Ananthakrishnan, Astrophys. J. **133**, 969 (1961).

7. S. O. Obashev, Izv. Krymsk. Astrofiz. Obs. **29**, 118 (1963).
8. V. S. Dermendzhiev, Astrofiz. Issled. (Sofia), No. 2, 8 (1977).
9. A. M. Cantu, G. Godoli, and G. Poletto, Mem. Soc. Astron. Ital. **38**, 367 (1968).
10. V. I. Makarov, Solnechnye Dannye, No. 4, 100 (1983).
11. I. S. Kim, V. Yu. Klepikov, S. Koutchmy, *et al.*, Solnechnye Dannye, No. 1, 75 (1988).
12. I. S. Kim, V. Yu. Klepikov, S. Koutchmy, *et al.*, Solnechnye Dannye, No. 5, 77 (1988).
13. V. I. Makarov, K. S. Tavastsherna, E. I. Davydova, and K. R. Sivaraman, Solnechnye Dannye, No. 3, 90 (1992).
14. P. Demoulin, Astron. Soc. Pacif. Conf. Ser. **150**, 78 (1998).
15. J. L. Leroy, V. Bommier, and S. Sahal-Brechot, Astron. Astrophys. **131**, 33 (1984).
16. I. S. Kim and V. F. Uvakina, in *The Solar Atmosphere, Interplanetary Medium, Planetary Atmospheres*, Ed. by R. A. Gulyaev (IZMIRAN, Moscow, 1989), p. 125.
17. V. P. Maksimov and L. V. Ermakova, Astron. Zh. **62**, 558 (1985).
18. S. A. Yazev and G. M. Khmyrov, Solnechnye Dannye, No. 12, 75 (1987).
19. B. A. Ioshpa and E. Kh. Kulikova, in *Solar Magnetic Fields and Corona*, Ed. by R. B. Teplitskaya (Nauka, Novosibirsk, 1989), Vol. 1, p. 167.
20. V. P. Maksimov and A. A. Prokop'ev, Astron. Zh. **70**, 1099 (1993).
21. R. Kippenhahn and A. Schluter, Z. Astrophys. **43**, 36 (1957).
22. M. Kuperus and M. A. Raadu, Astron. Astrophys. **31**, 189 (1974).
23. U. Anzer, Solar Phys. **8**, 37 (1969).
24. Y. Uchida, in *Proc. of the Japan–France Seminar on Solar Physics*, Ed. by F. Moriyama and J. C. Henoux (1981), p. 169.
25. J. M. Malherbe and E. R. Priest, Astron. Astrophys. **123**, 80 (1983).
26. P. Demoulin and E. R. Priest, Solar Phys. **144**, 283 (1993).
27. W. van Tend and M. Kuperus, Solar Phys. **59**, 115 (1978).
28. M. M. Molodenskiĭ and B. P. Filippov, Astron. Zh. **64**, 1079 (1987).
29. P. C. H. Martens and N. P. M. Kuin, Solar Phys. **122**, 263 (1989).
30. A. N. Tikhonov and A. A. Samarskiĭ, in *Equations of Mathematical Physics* (Nauka, Moscow, 1972), p. 363.
31. O. G. Den, O. E. Den, E. A. Kornitskaya, and M. M. Molodenskiĭ, Solnechnye Dannye, No. 1, 97 (1979).
32. V. Yu. Klepikov, in *The New Solar Cycle: Observational and Theoretical Aspects* (Pulkovo Astronomical Observatory, St. Petersburg, 1998), p. 269.

Translated by G. Rudnitskii

Astronomy Letters, Vol. 26, No. 5, 2000, pp. 328–330. Translated from Pis'ma v Astronomicheskiĭ Zhurnal, Vol. 26, No. 5, 2000, pp. 391–393.

Minicomets in the Solar System and in the Earth's Atmosphere and Related Phenomena

V. A. Bronshten

Committee on Meteorites, Russian Academy of Sciences, ul. Kosygina 19, Moscow, 117795 Russia

Received June 20, 1999

Abstract—We consider the history of discovery and justify the existence in the Solar system of a new class of bodies—minicomets, i.e., bodies of cometary nature and composition but of low mass. Two classes of minicomets are distinguished: icy ones similar to the Tunguska meteorite, and snow ones, which break up at high altitudes. © *2000 MAIK "Nauka/Interperiodica".*

Key words: *minicomets, bolides, upper atmosphere*

INTRODUCTION

In [1, 2], we stated the view that bodies of a cometary nature but of low mass exist in the Solar system. One of their representatives was the Tunguska meteorite ($M \sim 10^6$ t). More than 80% of the meteoroids observed as bolides by the Prairian and European fireball networks also belong to these bodies. We called them microcomets.

Ten years later, the American researchers L. Frank, J. Sygworth, and J. Craven [3] announced the discovery of minicomets, which manifested themselves as "ultraviolet holes" in the atmosphere, i.e., local declines in the intensity of the O (1304 Å), N_2 (1400–1700 Å), and Lα (1216 Å) line emission in regions of size $\sim 2 \times 10^3$ km^2. The authors attributed the formation of these holes to the screening of ultraviolet radiation by the water molecules brought into the upper atmosphere by comet-like objects. In their opinion, twenty 100-t minicomet nuclei enter the Earth's atmosphere in a minute, totaling 3×10^6 t day^{-1}. Previous astronomical estimates of the influx of meteoric matter on the Earth yielded 110 t day^{-1} [4], 150 t day^{-1} [5], and 50 t day^{-1} [6].

Cosmochemical methods (based mainly on estimates of the osmium and iridium contents in bottom deposits) yielded two to four orders of magnitude larger influxes (see [5] for a review). The cause of this discrepancy has not been established until very recently.

TWO CLASSES OF MINICOMETS?

The icy minicomets, which manifested themselves as bright fireballs [1, 2], and the snow minicomets announced by Frank *et al.* [3] differed markedly in physical properties. Whereas the former broke up in the atmosphere at "ordinary" meteoric altitudes (120–50 km), the latter were disrupted considerably higher, at altitudes 1000–200 km [7]. The question arises as to whether these bodies represent two distinct classes of minicomets or these are the disruption stages of the same bodies—icy nuclei surrounded by snow envelopes. Initially, we held the former viewpoint [8], but now there is reason to prefer the latter one. This issue will be considered in more detail in another paper.

V.N. LEBEDINETS'S STUDIES

A large series of studies by V.N. Lebedinets and his coworkers in the early 1990s showed that the concept of minicomets could easily account for a variety of hitherto unexplained natural phenomena, including the above discrepancy between astronomical and cosmochemical estimates for the influx of meteoric matter on the Earth.

Based on an analysis of the altitudes at which Draconides and radio meteors were disrupted, Lebedinets [9] showed that many of them ceased to exist at abnormally high altitudes. The Vega and Giotto experiments indicated that 30% of the submicron-sized dust grains in the coma of comet Halley consisted of C, H, O, and N (CNOH particles) and 35% were composed of their mixture with matter of chondritic composition. Thus, 50% of the mass of all meteoric bodies consists of organic material. However, "organic" micrometeoroids cannot be detected by astronomical methods, because they evaporate completely at high altitudes.

If the snow minicomets are covered with organic (rather than chondritic) film, its mass for 100-t minicomets may reach 10–100 kg, and it is capable of protecting a minicomet against solar heating and sublimation. This removes the main objection against the hypothesis of minicomets—the low dust content in them and the small thickness of the protective dust film.

Other phenomena hitherto unexplained, but readily explicable in terms of the minicomet hypothesis are

1063-7737/00/2605-0328$20.00 © 2000 MAIK "Nauka/Interperiodica"

listed and analyzed in [10]. These include the following: the motion of a luminous meteor trail; discrepancies between the results of acoustic and breakdown detectors when they record meteor impacts on spacecraft; an anomalous and growing (with altitude) dust content in the upper atmosphere (above 100 km); great enhancements of dust in the upper atmosphere during the action of large meteor streams; short-time (up to 40 min) increases (by two orders of magnitude) in the impact rates for (10^{-10}–10^{-16})-g dust grains; and an abrupt change in the distribution of zodiacal light at a distance of 0.5 AU from the Sun.

In the opinion of V.N. Lebedinets, minicomets, which bring to the Earth up to 10^5 t of organic material per day, can account for the high dust content in the stratosphere and mesosphere and for the presence of a dust cloud around the Earth. The short-time increases in the count rate of microparticles detected by satellite-borne instruments were explained by their passage through the dust jets from minicomet explosions.

Lebedinets [10] also considered the paradox between the high abundance of free oxygen in the atmosphere and the enormous amount of unoxidized substances in the Earth's crust, as was pointed out long ago by V.I. Vernadskii. In the opinion of Lebedinets, the main source of O_2 is in cosmos rather than in biota, ocean water and lithosphere; molecular oxygen is brought to the Earth by minicomets. They also determine the altitude profile of water vapor in the stratosphere and mesosphere and supply vapor to the mesopause, where its sublimation gives rise to noctilucent clouds.

Lebedinets and Kurbanmuradov [11] developed a mathematical global balance model of cometary water vapors in the atmosphere at altitudes of 60–140 km. If minicomets bring $(0.5–1) \times 10^6$ t of H_2O molecules into the Earth's atmosphere per day, then their relative density in the mesopause region must be $\sim 10^{-4}$, which is enough for vapor sublimation at $T \sim 160–170$ K. The smallest particles of interplanetary dust or the dust grains brought by minicomets can serve as condensation nuclei for noctilucent clouds. However, the number of interplanetary dust grains with $r > 1$ μm is not enough to serve as condensation nuclei. These can be particles with $r < 0.1$ μm from minicomets.

The previous results were reviewed by Lebedinets and Kurbanmuradov [12]. Begkhanov *et al.* [13] constructed a coagulation model for middle-atmosphere aerosols at minimum influx of meteoric matter, whose most likely estimate is 1000 t day^{-1} (for a mean particle density of 1 g cm^{-3}). As the particles sink into the atmosphere, they stick together and merge (coagulate) to produce the observed light-scattering layer at altitudes of ~50 km. The snow nuclei of minicomets are the main source of the influx of interplanetary dust.

Lebedinets [14] considered yet another phenomenon—the background sulfate layer in the atmosphere (Junge layer). Its origin is usually associated with sulfur ejections into the atmosphere during violent volcanic eruptions. However, the Junge layer experiences no sharp post-eruption density variations, while the influx of sulfur compounds (COS, H_2S, C_2S) from the troposphere is too small to maintain this layer. The author concludes that the Junge layer is formed from the sulfur brought by minicomets. The required sulfur influx of 10^6 t year^{-1} corresponds to a 30-fold depletion of the S/O ratio compared to their cosmic abundance, i.e., it is realistic.

Lebedinets [15] also analyzed a completely different phenomenon in cosmos rather than in the Earth's atmosphere—the observed breakup of cometary nuclei. This phenomenon (111 events in 160 years) can be explained by the bombardment of the nuclei of "large" comets by minicomets. The author estimated the breakup energy of cometary nuclei (~10^5 erg g^{-1}) and the frequency of disrupting collisions of comets of different masses with minicomets (from one collision every 3 or 4 years for comets with the nucleus radius $r = 3$ km to one collision every 25–30 years for comets with $r = 1$ km). Collisions with minicomets are much more effective than those with large meteorites.

A more thorough analysis of these collisions and their consequences was performed by Lebedinets [16]. The author showed that such collisions with comets produce minicomets, whereas collisions with asteroids produce swarms of stony meteorite-forming bodies. He also studied erosive processes on the surfaces of bodies without atmospheres (satellites, asteroids, Mercury and Pluto). The occasionally observed flashes on the Moon can also be attributed to the impacts of minicomets. The author separately considered the interaction of minicomets with the Martian atmosphere.

Each of the above studies by Lebedinets contains a serious mathematical analysis of the problems under consideration and relies on extensive literature. The previous difficulties, which are easily resolvable using the concept of minicomets, are so abundant that, even if we had known nothing about minicomets, their existence should have been suggested hypothetically. Fortunately, this is not needed.

The last study by Lebedinets appeared in the summer of 1993, and, on February 15, 1994, he passed away. The duty of currently living astronomers and geophysicists is to continue his investigations.

CONCLUSION

We have adduced a number of arguments for the hypothesis that there is a new class of bodies in the Solar system—minicomets, including the arguments outlined by Lebedinets. In the next paper, we are going to consider objections of those who criticize this hypothesis, as well as the relationship between icy microcomets [2] and snow minicomets [3].

REFERENCES

1. V. A. Bronshten, in *The Origin of Bodies in the Solar System* (VAGO GAO, Moscow, 1975), p. 265.
2. V. A. Bronshten, Astron. Vestn. **10**, 73 (1976).
3. L. A. Frank, J. B. Sigwarth, and J. D. Craven, Geophys. Res. Lett. **13**, 303 (1986).
4. A. N. Simonenko and B. Yu. Levin, Meteoritika, No. 31, 45 (1972).
5. V. A. Bronshten, Komety i Meteory, No. 32, 10 (1982).
6. V. N. Lebedinets, *Aerosols in the Upper Atmosphere and Cosmic Dust* (Gidrometeoizdat, Leningrad, 1981).
7. L. A. Frank and J. D. Craven, Rev. Geophys. **26**, 249 (1988).
8. V. A. Bronshten, Zemlya i Vselennaya, No. 5, 11 (1998).
9. V. N. Lebedinets, Astron. Vestn. **25**, 65 (1991).
10. V. N. Lebedinets, Astron. Vestn. **25**, 350 (1991).
11. V. N. Lebedinets and O. Kurbanmuradov, Astron. Vestn. **26**, 83 (1992).
12. V. N. Lebedinets and O. Kurbanmuradov, Astron. Vestn. **26**, 53 (1992).
13. M. Begkhanov, O. Kurbanmuradov, and V. N. Lebedinets, Astron. Vestn. **26**, 102 (1992).
14. V. N. Lebedinets, Astron. Vestn. **26**, 61 (1992).
15. V. N. Lebedinets, Astron. Vestn. **26**, 102 (1992).
16. V. N. Lebedinets, Astron. Vestn. **27**, 3 (1993).

Translated by A. Kozlenkov

Astronomy Letters, Vol. 26, No. 5, 2000, pp. 331–337. Translated from Pis'ma v Astronomicheskiĭ Zhurnal, Vol. 26, No. 5, 2000, pp. 394–400.

Asymmetric Periodic Solutions of the Averaged Hill Problem with Allowance for a Planet's Oblateness

M. A. Vashkov'yak* and N. M. Teslenko

Keldysh Institute of Applied Mathematics, Russian Academy of Sciences, Miusskaya pl. 4, Moscow, 125047 Russia

Received September 13, 1999

Abstract—We consider asymmetric periodic solutions of the double-averaged Hill problem by taking into account oblateness of the central planet. They are generated by steady-state solutions, which are stable in the linear approximation and correspond to satellite orbits orthogonal to the line of intersection of the planet's equatorial plane with the orbital plane of a disturbing point. For two model systems [(Sun + Moon)–Earth–satellite] and [Sun–Uranus–satellite], these periodic solutions are numerically continued from a small vicinity of the equilibrium position. The results are illustrated by projecting the solutions onto the (pericenter argument–eccentricity) and (longitude–inclination) planes. *© 2000 MAIK "Nauka/Interperiodica".*

Key words: *averaged Hill problem, periodic solutions, orbital evolution*

1. INTRODUCTION AND STATEMENT OF THE PROBLEM

This paper is devoted to constructing periodic solutions of the double-averaged Hill problem with allowance for oblateness of the central planet.

In this problem, the evolutionary set of differential equations has the following form:

$$\frac{d\mathbf{x}}{d\tau} = \mathbf{f}(\mathbf{x}), \tag{1}$$

where $\mathbf{x}^{\mathrm{T}} = (e, i, \omega, \Omega)$, τ is the normalized independent variable, which varies monotonically with physical time t; e, i, ω, and Ω are, respectively, the eccentricity, inclination, pericenter argument, and longitude of the ascending node of the satellite orbit. The angular variables are associated with the plane of the orbit of the perturbing point, which is tilted at an arbitrary angle ε to the equatorial plane of the planet, as well as to the line of intersection of these planes.

In a similar study [1], we investigated the periodic solutions generated by the steady-state solutions

$$\omega^* = \pm 90^\circ, \quad i^* = i^*(\varepsilon), \quad \Omega^* = 0, 180^\circ,$$

where ω^*, i^*, and Ω^* are the equilibrium values of the orbital elements ω, i, and Ω. These solutions possess a symmetry about the axes $\omega = \pm 90^\circ$ in projection onto the (ω, e) plane and about the axes $\Omega = 0, 180^\circ$ in projection onto the (Ω, i) plane.

In contrast to the above work, we consider here the periodic solutions generated by the steady-state solutions

$$\sin 2\omega^* = 0, \quad \cos i^* = 0, \quad \cos\Omega^* = 0. \tag{2}$$

Previously [2], these solutions were shown to have no axial symmetry and their asymmetry will be illustrated below.

In the case of an oblate planet, when the coefficient of the second zonal harmonic of its gravitational field is negative ($c_{20} < 0$), the generating solutions (2) exist only for $\omega^* = 0, \pi$ and are stable in the linear approximation [3]. For these solutions, the equilibrium values of the eccentricity e^* and the semimajor axis a^* are related by the equation

$$e^{*2} = 1 - (\gamma/2)^{2/5}, \tag{3}$$

in which

$$\gamma = -\frac{\mu a_0^2 c_{20} a_1^3}{\mu_1 a^{*5}} \tag{4}$$

is the parameter of the problem that depends (in addition to the above constants) on the products of the gravitational constant and the masses of a planet and a perturbing point (μ and μ_1, respectively), on the mean equatorial radius of the planet a_0, and on the semimajor axis a_1 of the orbit of the perturbing point. In the case of N coplanar circular orbits of perturbing points, the combination μ_1/a_1^3 in formula (4) should be replaced by

$$\sum_{j=1}^{N} \mu_j/a_j^3.$$

* E-mail address for contacts: vashkov@spp.keldysh.ru

1063-7737/00/2605-0331$20.00 © 2000 MAIK "Nauka/Interperiodica"

In what follows, we shall consider, as examples, the model systems [Sun + Moon)–Earth–satellite], $N = 2$, $\varepsilon = 23^\circ.44$ and (Sun–Uranus–satellite), $N = 1$, $\varepsilon = 97^\circ.8$. For each of these systems, the parameter γ is chosen from the condition of equality of two frequencies of small oscillations of orbital elements in the vicinity of the generating solution (2). Such a resonant value of the parameter γ is determined by the formula [2]

$$\gamma_{res} = 2\left(1 + \frac{2}{25}\sin^2\varepsilon\right)^{-5/2} \quad (5)$$

and stipulates the existence of the simplest periodic solutions with small amplitudes relative to the orbital elements e^*, i^*, ω^*, Ω^* and with the period

$$T = \frac{\pi}{20}(2 + 25\,\mathrm{cosec}^2\varepsilon)^{1/2} \quad (6)$$

in τ depending solely on ε.

Our aim is to extend numerically these solutions to the region of large deviations from the equilibrium position (e^*, $i^* = 90^\circ$, $\omega^* = 0$, $\Omega^* = 90^\circ$).

2. DESCRIPTION OF THE ALGORITHM FOR CONSTRUCTING ASYMMETRIC PERIODIC SOLUTIONS

We proceed from the conditions of periodicity of solutions of the evolutionary system of four differential equations for the problem under study,

$$\begin{aligned} e(T, e_0, i_0, \omega_0, \Omega_0) &= e_0, \\ i(T, e_0, i_0, \omega_0, \Omega_0) &= i_0, \\ \omega(T, e_0, i_0, \omega_0, \Omega_0) &= \omega_0, \\ \Omega(T, e_0, i_0, \omega_0, \Omega_0) &= \Omega_0. \end{aligned} \quad (7)$$

The initial values of the elements of the satellite orbit at the time $\tau = 0$, with which we perform the numerical integration of the evolutionary system, are marked by subscript 0. In what follows, for convenience and without loss of generality, we set $\omega_0 = 0$. Assuming that the variations of all the elements retain the libration pattern (as in the position close to the equilibrium one), we can obtain the values of the elements $e(\tau)$, $i(\tau)$, and $\Omega(\tau)$ at the instant of time $\tau > 0$ when the condition

$$\omega(\tau > 0, e_0, i_0, 0, \Omega_0) = 0. \quad (8)$$

is satisfied. Our goal is to find, by a proper choice of the e_0, i_0, and Ω_0 values, the instant $\tau = T$ at which all the equalities (7) are satisfied. This, in general, three-dimensional problem can be reduced to the two-dimensional one, if we take into account that system (1) has the first integral—averaged perturbing function $W(e, i, \omega, \Omega) = \text{const}$. Its explicit form enables one to obtain the dependence of the inclination i on the remaining orbital elements and parameter W, $i = i(e, \omega, \Omega, W)$, and to reduce by unity the dimension of the boundary-value problem. However, practice of computations showed that, by virtue of the ambiguity of this dependence, the algorithm of the two-dimensional boundary-value problem proves to be incorrect in certain cases. As a consequence, the three-parameter procedure was used as a regular algorithm in searching for periodic solutions. When constructing symmetric T-periodic solutions [1], it was sufficient to perform numerical integration of the system on the segment $0 < \tau < T/2$.

In order to construct a family of periodic solutions, we chose the method of "motion" in parameter. As applied to our problem, the most convenient parameter is one of the extremum values of eccentricity.

Let the initial data (e_0, i_0, $\omega_0 = 0$, Ω_0) determine a periodic solution with the period T, i.e., conditions (7) are satisfied. If, as a result of solution of the three-dimensional boundary-value problem with varied values e_0, i_0, and Ω_0, we find such corrections δe_0, δi_0, $\delta\Omega_0$, that the conditions

$$\begin{aligned} e(T^{(1)}, e_0^{(1)}, i_0^{(1)}, 0, \Omega_0^{(1)}) &= e_0^{(1)}, \\ i(T^{(1)}, e_0^{(1)}, i_0^{(1)}, 0, \Omega_0^{(1)}) &= i_0^{(1)}, \\ \omega(T^{(1)}, e_0^{(1)}, i_0^{(1)}, 0, \Omega_0^{(1)}) &= 0, \\ \Omega(T^{(1)}, e_0^{(1)}, i_0^{(1)}, 0, \Omega_0^{(1)}) &= \Omega_0^{(1)} \end{aligned}$$

are satisfied in the integration of system (1) with the initial data $e_0^{(1)} = e_0 + \delta e_0$, $i_0^{(1)} = i_0 + \delta i_0$, $\omega_0^{(1)} = 0$, and $\Omega_0^{(1)} = \Omega_0 + \delta\Omega_0$ on the interval from $\tau = 0$ to $\tau = T^{(1)}$, then a new periodic solution with the period $T^{(1)}$ and initial data $e_0^{(1)}$, $i_0^{(1)}$, $\omega_0^{(1)} = 0$, $\Omega_0^{(1)}$ will be determined. At the next step the procedure is repeated for the found solution: it serves to determine a solution with the initial data $e_0^{(2)}$, $i_0^{(2)}$, $\omega_0^{(2)} = 0$, $\Omega_0^{(2)}$ and the period $T^{(2)}$, etc. Recall that the elements of the equilibrium orbit,

$$e^*, i^* = 90^\circ, \quad \omega^* = 0, \quad \Omega^* = 90^\circ. \quad (9)$$

are chosen as an initial approximation in this procedure.

3. EXAMPLES OF THE FAMILIES OF PERIODIC SOLUTIONS

The algorithm described here was realized in the numerical construction of the family of periodic solutions in the vicinity of the generating equilibrium solution (9). Calculations were performed for two model systems (see Sect. 1): in the first and second cases, the central planet is the Earth and Uranus, respectively.

To represent numerical results for each of these variants in a graphical form, we took several orbits in order of increasing the period of oscillations of the orbital elements. Numerical values of the elements of the selected orbits at two instants of time, $t = 0$ and $t = T/2$, as well

Table 1. Parameters of periodically evolving satellite orbits in the system [(Sun + Moon)–Earth–satellite]: $\gamma \approx 1.93$, $e^* = 0.11895$, $i^* = 90°$, $\omega^* = 0$, $\Omega^* = 90°$, $W^* = -4.5723$, $T^* = 219.5$ yr, $a^* = 37298$ km, $P^* = 19^h.9$

No.	e_0	$e(T/2)$	i_0, deg	$i(T/2)$, deg	$\omega(T/2)$, deg	Ω_0, deg	$\Omega(T/2)$, deg	T, yr	W
1	0.13996	0.09329	89.61	90.41	0	88.83	91.15	226.2	−4.5723
2	0.16226	0.06646	85.75	94.13	0	77.62	102.18	237.4	−4.5601
3	0.18291	0.04498	81.82	97.89	0	65.49	113.98	247.3	−4.5264
4	0.19494	0.02575	77.81	101.73	−0.01	51.33	127.77	268.2	−4.4697
5	0.18888	0.01250	74.39	105.12	−0.02	35.82	143.07	307.5	−4.4019
6	0.15249	0.00409	71.85	107.84	−0.02	17.12	161.88	404.2	−4.3377
7	0.11603	0.00171	71.23	108.60	−0.01	7.36	171.86	524.8	−4.3197

as the values of T and of the first integral W, are listed in Table 1 (variant 1) and Table 2 (variant 2). In addition, we indicate the values of parameters common for the specified family: the perturbation parameter γ; the elements of the equilibrium orbit (9) e^*, i^*, ω^*, and Ω^*; the first integral W^*; the semimajor axis a^* of the satellite orbit; the satellite revolution period P^*; and the period T^* of small oscillations in the vicinity of the equilibrium solution.

For each of the periodically evolving orbits, we calculated the time dependence of all the elements on the interval equal to the evolution period T. The results of calculations are presented as projections of phase curves in Figs. 1–4 (variant 1) and Figs. 5–9 (variant 2). Since the behavior of phase curves for two variants has its peculiarities, it is expedient to perform further description of the graphic material for each variant separately.

3.1. Periodic Solutions for the System [(Sun + Moon)–Earth–satellite]

The periodic phase trajectories in the space (e, i, ω, Ω) for variant 1 are presented as their two-dimensional projections onto the planes of two variables: (ω, e) in Fig. 1 and (Ω, i) in Fig. 2. The same four-dimensional phase trajectories are displayed as projections onto the subspace (ω, e, Ω) in Fig. 3 and onto the subspace (i, e, Ω) in Fig. 4. Here were also depicted two-dimensional projections: onto the plane (ω, e) in Fig. 3 and onto the plane (Ω, i) in Fig. 4 (see for comparison Figs. 1 and 2).

The whole system of spatial curves is mapped on the planes of the drawings with the help of axonometric projecting from different directions, which were specially selected so as to demonstrate most clearly the mutual disposition of all the curves. These curves were artificially shifted in the direction of the Ω axis (Fig. 3) or the e axis (Fig. 4) lest the three-dimensional curves

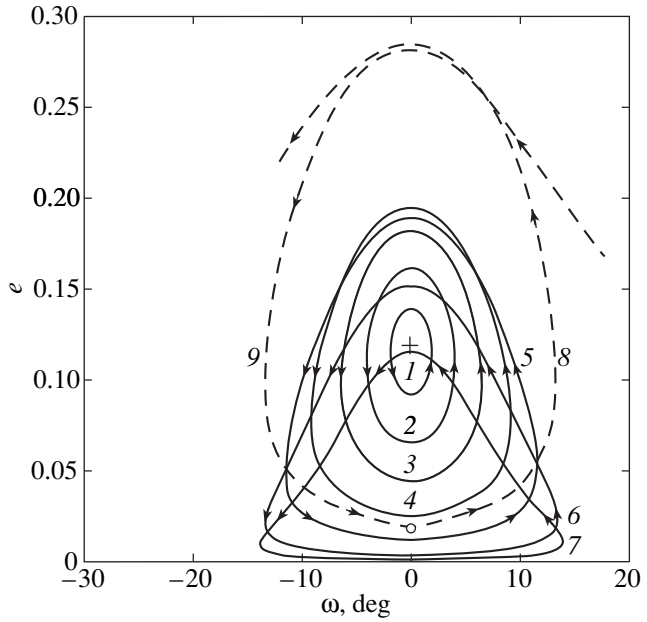

Fig. 1. Phase trajectories in projection onto the (ω, e) plane (variant 1).

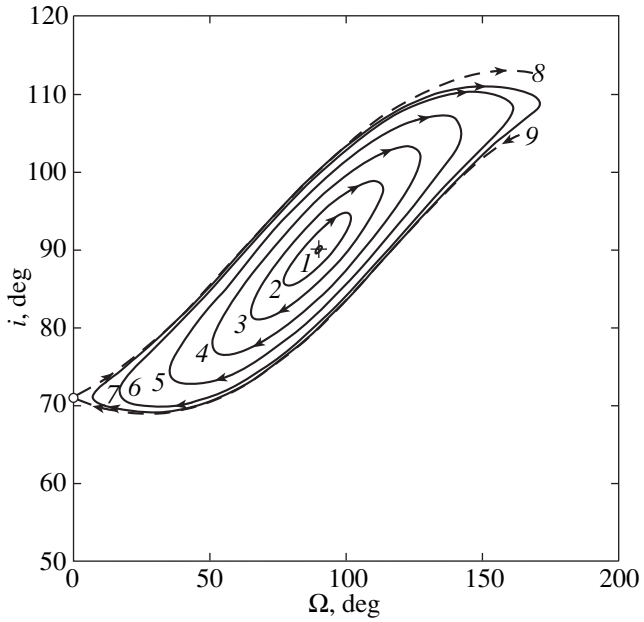

Fig. 2. Phase trajectories in projection onto the (Ω, i) plane (variant 1).

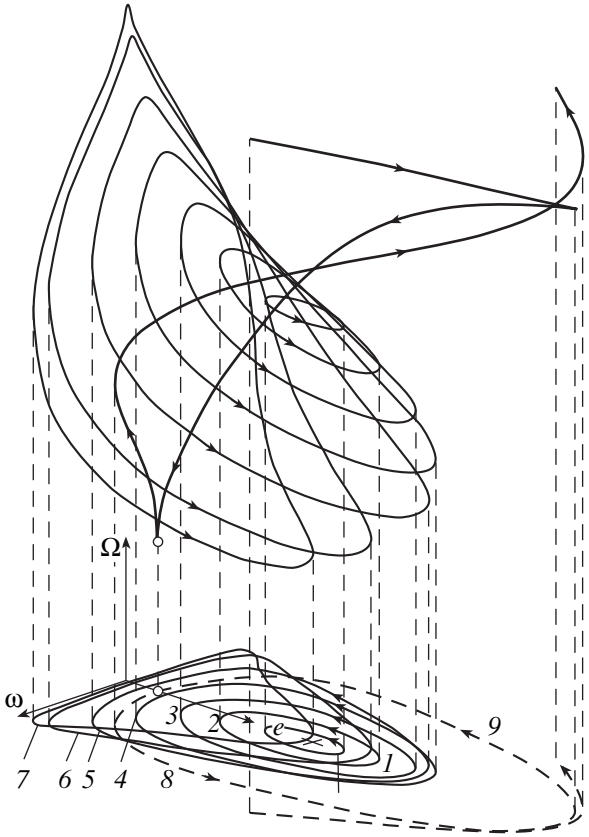

Fig. 3. Phase trajectories in projection onto the (ω, *e*, Ω) subspace (variant 1).

be superposed visually on their two-dimensional projections. Arrows in the curves indicate the direction of evolution with increasing time. The crosses in the figures mark the equilibrium solution e^*, $i^* = \Omega^* = 90°$, $\omega^* = 0$, which generates a family of periodic solutions.

In the small vicinity of the equilibrium solution, the periodic trajectories *1–3* in plane (ω, *e*) are nearly symmetric with respect to the ω = 0 axis and relative to the inclined axis in the (Ω, *i*) plane. As the amplitude of oscillations increases, this symmetry breaks down, though insignificantly in this variant 1 (see the values of ω(*T*/2) in Table 1 for curves *4–7*).

The amplitude of oscillation of the eccentricity reaches ~0.2 and then begins to decrease. The amplitude of oscillation of the pericenter argument for trajectories of the given family does not exceed 14°.

The ranges of oscillations are most significant for the inclination *i* (from 70° to 110°) and the nodal longitude (from 7° to 172°).

We see from Fig. 2 that curve *7* is located in a sufficiently small vicinity of the asymptotic curves *8* and *9*, while the period of oscillations is almost twice the period *T** (see Table 1). The resulting computational problems give no way of tracing the subsequent transformation of trajectories in the phase space, in particular in the (ω, *e*) plane, where for the last of constructed curves we have $e_{min} \approx 0.0017$ and $e_{max} \approx 0.116$.

Asymptotic trajectories pass through the unstable stationary points $\Omega = \omega = 0$, $i \approx 71^\circ.12$, $e \approx 0.0199$, and $W \approx -4.3151$ marked by circles in the figures. A small vicinity of these points was investigated analytically by the author [2]. Also described was the effect of asymmetry of these periodic solutions in the small vicinity of the generating solution $i = \Omega = 90°$ and $\omega = 0$.

3.2. Periodic Solutions in the System (Sun–Uranus–Satellite)

A graphical representation of periodic solutions is similar to that in variant 1, but the phase trajectories in

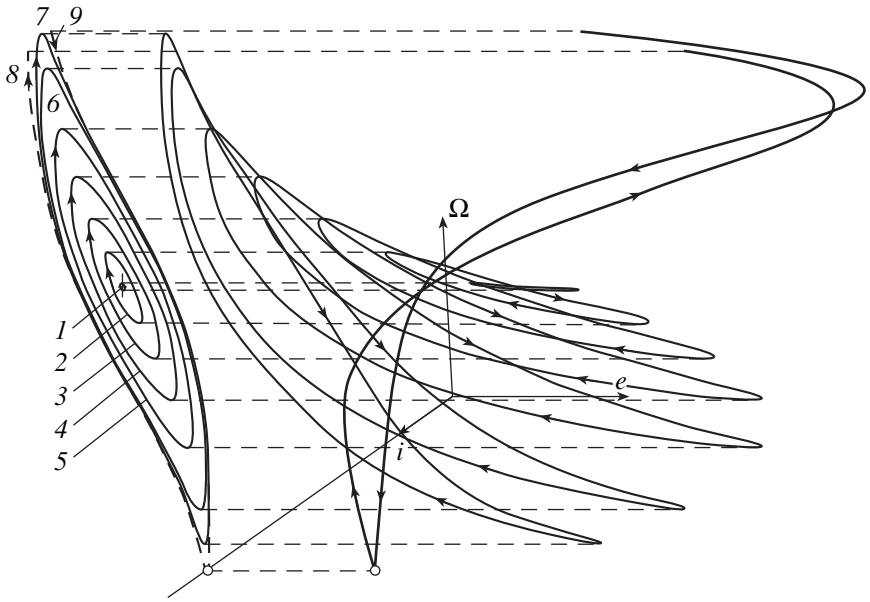

Fig. 4. Phase trajectories in projection onto the (*i*, *e*, Ω) subspace (variant 1).

Table 2. Parameters of periodically evolving satellite orbits in the system (Sun–Uranus–satellite): $\gamma \approx 1.66$, $e^* = 0.26977$, $i^* = 90°$, $\omega^* = 0$, $\Omega^* = 90°$, $W^* = -4.1815$, $T^* = 53603.5$ yr, $a^* = 1\,074\,819$ km, $P^* = 33^d16^h$

No.	e_0	$e(T/2)$; e_{min}	i_0, deg	$i(T/2)$, deg	$\omega(T/2)$, deg	Ω_0, deg	$\Omega(T/2)$, deg	T, yr	W
1	0.30053	0.24369	89.28	90.73	0.02	85.59	94.49	53919.5	−4.1365
		0.24369							
2	0.34145	0.23023	96.48	84.37	3.50	77.97	102.44	56042.9	−3.8833
		0.22390							
3	0.35501	0.33376	120.26	60.51	5.54	78.69	101.74	58467.1	−3.6752
		0.25342							
4	0.37966	0.37966	131.09	48.91	0	79.45	100.55	62010.4	−3.4543
		0.27362							
5	0.38995	0.38995	150.52	29.48	0	61.66	118.34	81896.4	−2.8280
		0.19878							
6	0.29919	0.29919	157.60	22.40	0	43.30	136.70	115836.3	−2.4604
		0.11727							
7	0.16102	0.16102	160.16	19.84	0	33.27	146.73	151489.0	−2.3102
		0.05410							
8	0.03998	0.03998	160.86	19.14	0	29.96	150.04	167506.3	−2.2720
		0.01272							

the (ω, e) plane evolve in this case in a more complicated manner. In a small vicinity of the generating solution, periodic trajectories are nearly symmetric with respect to the axis $\omega = 0$ (Fig. 5). For curve *1* $\omega(T/2) \approx 0\overset{\circ}{.}02$ (Table 2). An increase in the evolution period leads not only to the rise of the amplitude of oscillation of the elements (curve *2*), but also to the occurrence of a loop (curve *3*). The asymmetry of these curves also increases: we see from Table 2 that $\omega(T/2)$ reaches several degrees. While increasing in size, the formed loop merges over the entire length with the main curve *4* so that the phase point in plane (ω, e) circumscribes twice the same trajectory over the evolution period, with $\omega(T/2) = \omega_0 = 0$. All other curves in Fig. 6 (*5*–*8*) also possess this property.

As the evolution period increases, a nearly oval form of curves *4* and *5* becomes strongly distorted, while trajectories themselves become highly asymmetric when they approach the horizontal axis (curve *8*). As a result, $e_{min} \approx e_{max} \longrightarrow 0$. At the same time, the phase point in plane (Ω, i) makes only one revolution moving along closed trajectories (Fig. 7). As T increases, these trajectories tend to the asymptotic trajectories *9* and *10*, whose existence follows from analysis of a specific case of the problem with $e = 0$ (see, e.g., [4]). The asymptotic trajectories pass through the unstable equilibrium positions corresponding to the Laplace plane and marked by circles in Fig. 7 ($\Omega = 0$, $i \approx 168\overset{\circ}{.}8$; $\Omega = 180°$, $i \approx 11\overset{\circ}{.}2$).

To better understand the structure of four-dimensional phase trajectories, we used the already described representation of such trajectories in the form of projections onto subspaces of two or three variables in different combinations. For example, the three-dimensional projections onto the (ω, e, Ω) subspace and two-dimensional projections onto the (ω, e) plane are shown in Fig. 8. The corresponding projections onto the (i, ω, Ω) plane and the (Ω, i) plane are displayed in Fig. 9.

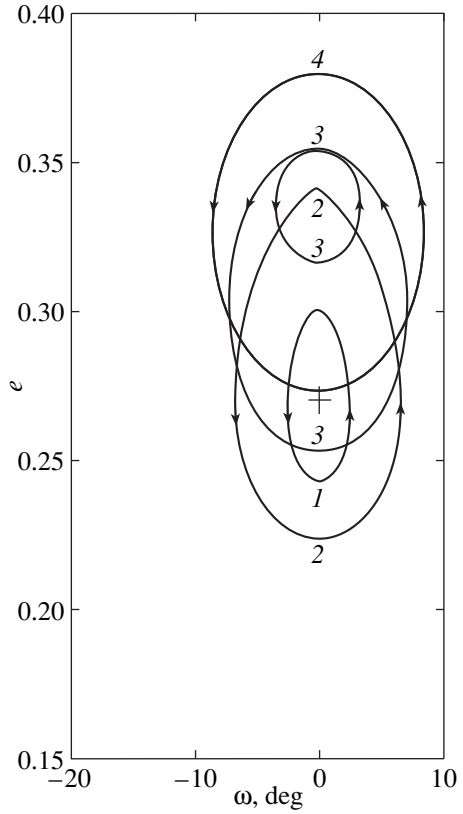

Fig. 5. Phase trajectories in projection onto the (ω, e) plane (variant 2).

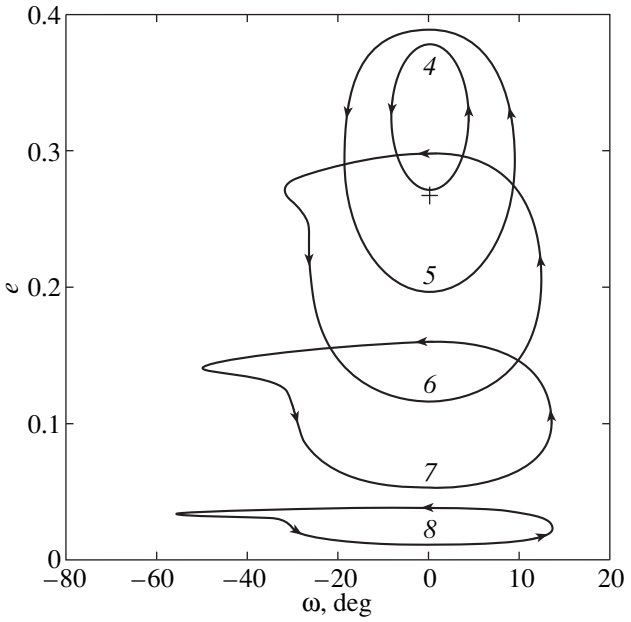

Fig. 6. Phase trajectories in projection onto the (ω, *e*) plane (variant 2).

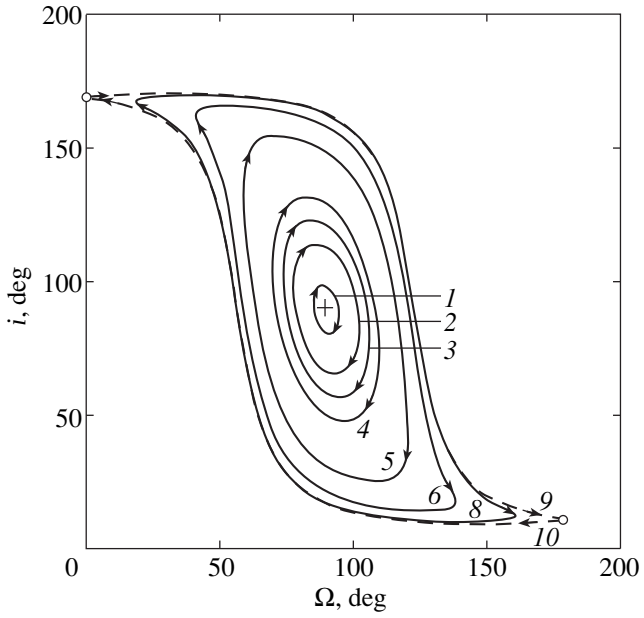

Fig. 7. Phase trajectories in projection onto the (Ω, *i*) plane (variant 2).

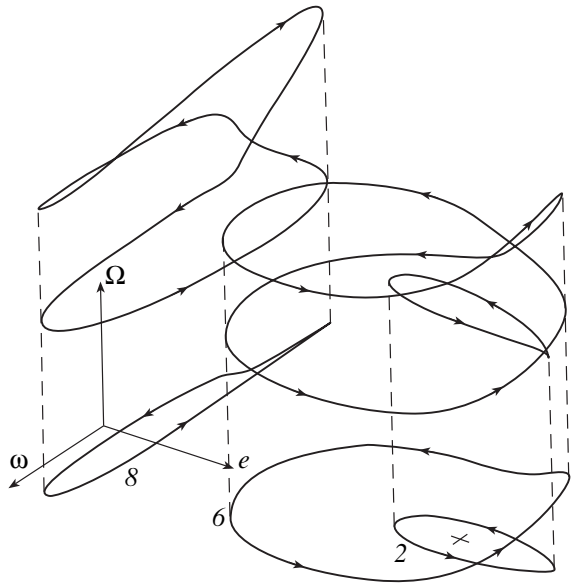

Fig. 8. Phase trajectories in projection onto the (ω, *e*, Ω) subspace (variant 2).

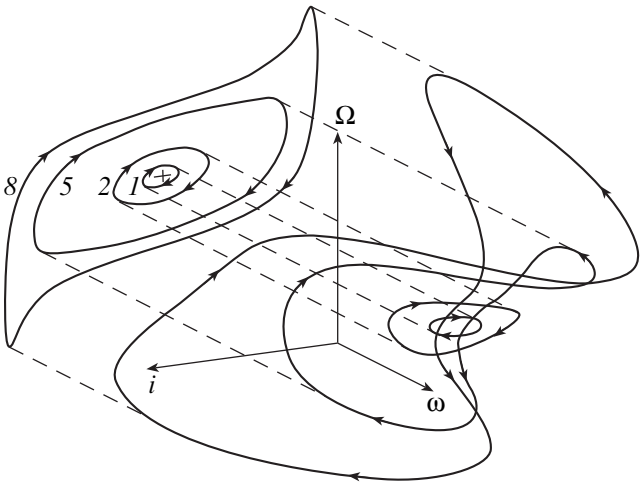

Fig. 9. Phase trajectories in projection onto the (*i*, ω, Ω) subspace (variant 2).

CONCLUDING REMARKS

This study completes a certain stage associated with the search for and construction of periodic solutions of the double-averaged Hill problem with allowance for oblateness of the central planet. The families of asymmetric periodic solutions are presented for two model systems, [(Sun + Moon)–earth–satellite] and (Sun–Uranus–satellite). These families start in a small vicinity of steady-state solutions ($\omega^* = \cos i^* = \cos\Omega^* = 0$), which are stable in a linear approximation and end in the asymptotic solutions passing through unstable equilibrium positions. In addition, two other families of periodic solutions with the inverse direction of evolution exist by virtue of the invariance of the evolutionary system relative to the substitution

$$\bar{\tau} = -\tau, \quad \bar{e} = e, \quad \dot{i} = i, \quad \bar{\omega} = -\omega, \quad \bar{\Omega} = -\Omega.$$

The projections of these solutions onto the (ω, *e*) and (Ω, *i*) planes are symmetric with respect to the con-

structed solutions; they are obtained by a mirror reflection of Figs. 1, 5, and 6 relative to the straight line $\omega = 0$ and by reflection of Figs. 2 and 7 relative to the straight line $\Omega = 0$.

The study of stability of periodic (symmetric and asymmetric) solutions established in our works reduces to obtaining the fundamental matrix of solutions to a linearized set of equations with T-periodic coefficients for time $\tau = T$. This problem will be considered in one of the next papers.

REFERENCES

1. M. A. Vashkov'yak, Pis'ma Astron. Zh. **25**, 792 (1999) [Astron. Lett. **25**, 688 (1999)].
2. M. A. Vashkov'yak, Pis'ma Astron. Zh. **25**, 631 (1999) [Astron. Lett. **25**, 544 (1999)].
3. M. A. Vashkov'yak, Pis'ma Astron. Zh. **24**, 791 (1998) [Astron. Lett. **24**, 682 (1998)].
4. M. A. Vashkov'yak, Cosmich. Issled. **12**, 834 (1974).

Translated by A. Kozlenkov